UNIVERSITY OF CALIFORNIA,
IRVINE

Relic Galaxy Analogies in N-body Simulations: Exploring Viable Definitions for Relicness

DISSERTATION

submitted in partial satisfaction of the requirements
for the degree of

DOCTOR OF PHILOSOPHY

in Physics

by

Hasitha Eranda Pituwala Kankanamge

Dissertation Committee:
Professor David Buote, Chair
Professor Herbert Hamber
Professor Aaron Barth

2023

DEDICATION

To international grad students who could not see their families for years while having visa deadlines.

TABLE OF CONTENTS

LIST OF FIGURES

LIST OF TABLES

ACKNOWLEDGMENTS

I acknowledge and thank the UC Irvine Department of Physics & Astronomy for providing me with a departmental fellowship for the last quarter in my graduate school. I also thank my supervisor Prof. David A. Buote for supporting one quarter as a graduate student researcher.

This thesis uses data from the cosmological hydrodynamical simulation that is publicly available. I would like to thank Dr. Dylan Nelson at Institute for Theoretical Astrophysics, the Center for Astrophysics of Heidelberg University, Germany, who answered all my questions about the TNG300 simulation. Part of our data analysis were performed on the High Performance Community Computing Cluster (HPC3) at the University of California, Irvine. All particle level data for TNG300 simulation were stored in Campus Research Storage Pool (CRSP) at UC Irvine which was possible thanks to my advisor Prof. David A. Buote who prvided funding.

I would like to thank my advisor Prof. David A. Buote for accepting me in the middle of my graduate student career when my future at UC Irvine was uncertain. Thank you for suggesting interesting projects and guiding me through my graduate career.

I would like to thank my committee members, Prof. Herbert Hamber and Prof. Aaron Barth, for their time and help. I enjoyed my work with Herbert and I would like to thank him for giving me the opportunity to work on theoretical cosmology. I would like to thank Prof. Aaron for allocating time to go through my thesis and giving me invaluable suggestions.

I want to thank my friends who have supported me through my rough times and not feel alone in a town where I did not know any Sri Lankans. I want to thank Nayana, Hooshang, Milad and Sunny who prevented me from leaving grad school and because of their motivational speeches, I managed to continue. I am forever grateful to Jan and two rescuers for saving my life in Alaska. I would also like to thank Maeve from the office of campus social work, for helping me with financial and legal aid which helped me immensely with my visa and other deadlines.

I would like to thank my wife Becky, without her mental support I would not have survived my later half of my grad school career. Finally, I thank my family for all the support. My dad has always inspired me to go in to science and my mom has always been behind me. It was hard not seeing my parents and my siblings for more than 4 years and counting, but with their continuous support, I managed to continue my work. I also thank my loku appachchi and loku amma for gifting me astronomy books and a telescope that ignited my passion for astrophysics.

VITA

Hasitha Eranda Pituwala Kankanamge

EDUCATION

Doctor of Philosophy in Physics **2023**
University of California, Irvine *Irvine, California*

Bachelor of Science in Physics **2016**
University of Colombo *Colombo, Sri Lanka*

RESEARCH EXPERIENCE

Graduate Research Assistant **Winter 2023**
University of California, Irvine *Irvine, California*

TEACHING EXPERIENCE

Teaching Instructor **Spring 2022**
University of California, Irvine *Irvine, California*

Graduate Teaching Assistant **2017-2022**
University of California, Irvine *Irvine, California*

REFEREED JOURNAL PUBLICATIONS

Gravitational Fluctuations as an Alternative to Inflation III.Numerical Results **2020**
Universe

ABSTRACT OF THE DISSERTATION

Relic Galaxy Analogies in N-body Simulations: Exploring Viable Definitions for Relicness

By

Hasitha Eranda Pituwala Kankanamge

Doctor of Philosophy in Physics

University of California, Irvine, 2023

Professor David Buote, Chair

This thesis demonstrates the potential of the cosmological hydrodynamical simulation IllustrisTNG 300-1 to investigate and to provide fresh insights into the search for massive relic galaxies that are believed to skip the second phase of the two-phase formation process for massive ETGs. We present an analysis of the stellar mass and size of massive early-type galaxies (ETGs) in the TNG300-1 at redshifts $z = 0$ and $z = 2$, using simulation particle level data. We implemented a dust attenuation process via a semi-analytical approach for star light, and we derive the stellar mass-size relation. We find that the derived median mass-size relation is in good agreement with the observations (within 10% of the predictions from Sloan Digital Sky Server).

We developed methods to define the relicness of massive compact galaxies physically by constraining dark matter and stellar mass after redshift 2, and examine the stellar and dark matter properties of the selected relics. We find that constraining dark matter mass within a proper length of 100 kpc is better suited than virial radii to quantify the passiveness of dark matter mass growth. We have also demonstrated that the relicness defined physically corroborates the definition based on compactness that has been used in observations. Additionally, we have demonstrated that the dark matter halo concentration of the selected relics shows a positive correlation with relicness (i.e., passiveness). We also explored various methods that

have been used in observations, to define relicness using compactness of galaxies. We find that massive relics with low virial mass ($M_{200} < 10^{13} M_{\odot}$) have a higher dark matter halo concentration (c_{200}), i.e., above the ΛCDM $c_{200} - M_{200}$ relationship.

Motivated by the massive relic galaxy Mrk 1216 which has an extremely high dark matter halo concentration, we have presented our analysis of dark matter halo concentrations (c_{200} and c_{2500}) in TNG300. We have verified the expected $c_{200} - M_{200}$ relation for halos with mass $10^{12} M_{\odot} \leq M_{200} \leq 3 \times 10^{13} M_{\odot}$ and for the first time we have presented the power law fit for $c_{2500} - M_{2500}$ for simulated halos in this mass range. We verify that both concentrations follow a log-normal distribution with similar scatter for a given mass bin. Furthermore, we have been able to find a few halos with extremely high concentrations (i.e., positive outliers with above $5\,\sigma$ from the ΛCDM $c_{200} - M_{200}$ relationship). We investigate the gas and interactions with the local environment of these halos and find that all these halos do not have any gas and have shown many interactions (i.e., flybys) with other subhalos since redshift 2.

Chapter 1

Introduction

1.1 Massive Galaxy Formation

Galaxies are collections of matter on vast scales that have captivated the human imagination for centuries. They have also served as powerful testing grounds for astrophysical theories. Indeed, understanding how galaxies form and evolve has been a persistent and fundamental challenge in the field of astrophysics for many decades. Galaxy formation remains a key astrophysical problem since it is a complex process with many variables determining numerous processes that galaxies experience in their lifetime (for a review see Benson et al. [10], also see the two books by Mo et al. [122] and Cimatti et al. [29]).

In the ΛCDM model, the matter power spectrum, which describes the correlation of density fluctuations with the spatial scale, is larger on small scales [149, 150]. This means that the density perturbation amplitude in the early universe is larger on smaller scales. Therefore, smaller structures are the first structures to undergo gravitational collapse to form halos (in general, the collapse is described by the top-hat spherical collapse model [67, 68]). Subsequently, larger structures form by merging smaller halos. This process is called "hierarchical

clustering" or "bottom-up growth" [223]. The baryons relax and cool to form cold gas and stars.

1.1.1 Two-Phase Galaxy Formation

It is established that the evolution of massive early-type galaxies (ETGs) may be broadly described by two distinct phases [147, 61]. In the first phase, which ends by a redshift $z \sim 2-3$, the stellar mass of the galaxy increased mainly by gas collapsing within the dark matter halo to form "in situ" stars [47]. This early rapid star formation, also called "cold-flow-driven" star formation [45], forms in situ stars near the galaxy center. The central region of these galaxies (i.e. within an effective radius) is highly dense compared to local ETGs [38, 211]. These compact ($R_e \lesssim 2$ kpc) and massive ($M_* \gtrsim 10^{11}\ M_\odot$) galaxies observed at $z \gtrsim 2$, which are the finished product of Phase-1 evolution, are called "red nuggets" [40].

The history of cosmic star formation rates suggests that the mechanism of Phase-1 mass accretion peaked somewhere between $z = 2$ and $z = 1.5$ [110]. Although Phase-1 is expected to be terminated by the redshift $z \sim 2$, it was observed that the median size for a given stellar mass and stellar masses has increased from the redshift $z \sim 2$ to $z = 0$ [213]. Initially, it was unclear whether it is due to size growth in individual galaxies or due to progenitor bias, which is the addition of newly quenched galaxies to the already quenched galaxy population [57]. Currently, there is a great deal of evidence to suggest that the massive galaxies typically continue to grow in stellar mass and size [1, 144]. Although it has been observed that the sizes of ETGs at $z = 0$ are roughly 2.6-6 times larger than their counterpart galaxies at $z \sim 2$ [199, 28, 18], the same trend has not been observed for the stellar masses of ETGs, which show only a factor ~ 2 growth since $z \sim 2$. It is widely accepted that the stellar mass growth after $z \sim 2$ is mainly due to a build-up in the outer shells of the galaxies [216].

This slower outer growth signifies the beginning of the second phase, which is driven by

"dry" minor mergers (see Section 1.1.2 for the definition) [141, 8, 78], while in situ star formation can only contribute $\sim 20\%$ of the stellar mass growth since $z \sim 2$ [209, 102, 216]. Although on average one major merger can occur since $z \sim 3$ [112, 114], minor dry mergers are more frequent than dry major [86] and major mergers generally [34]. In Section 1.1.2 we discuss the influence of minor dry mergers and other interactions with the environment.

1.1.2 Galaxy Interaction with the Environment

The environment around a galaxy has a profound effect on its evolution. On the basis of the type of interaction with its environment, this evolution may be divided into a few categories.

1. Mergers and harassment
2. Tidal stripping
3. Ram pressure stripping

Interactions between distinct galaxies (i.e. for which neither galaxy is a subhalo of the other) could mainly occur via harassment [123] or mergers. Galaxy harassment is a process that heats up a particular galaxy through a high-speed, close encounter with another galaxy. This "heating up" of the perturbed galaxy increases the kinetic energy of its constituent particles (stars, gas, and dark matter), causing them to be less gravitationally bound, and therefore making the galaxy vulnerable to disruption by more disturbances resulting from further encounters. The effects of harassment are more pronounced in low-mass galaxies [24].

Galaxy mergers are mainly categorized into two groups on the basis of the relative stellar masses of the interacting pair. Major mergers occur when the two galaxies have similar stellar masses, and as such are conventionally defined when the ratio of the stellar masses is greater than 1/3. Minor mergers are said to occur for lower mass ratios with a lower limit of

1/10 typically considered. In addition to the classification based on stellar masses, the mass fraction of cold gas is used to designate the mergers as wet or dry mergers. As its names suggest, a "dry merger" does not contain much cold gas in the progenitor compared to a "wet merger". Typically the line of demarcation drawn between the two types of mergers is for a cold gas fraction of 0.15 in the progenitor; i.e., a cold gas fraction greater than 0.15 represents a wet merger. Mergers have a greater impact on the growth of stellar mass and size at lower redshift ($z < 1$) compared to earlier times ($z > 2$) [116]. Major wet mergers add stellar mass to the ETG without significantly affecting the size [46], while minor dry mergers increase the size of the ETG without adding much stellar mass [132, 175, 73] for $z < 1$. These properties of wet and dry mergers are well established from observations [144, 231, 72], and theoretical simulations have also shown that major mergers do not cause significant size growth compared to dry minor mergers [146, 8].

In addition to stellar mass and size, mergers induce changes in a variety of galaxy properties for $z < 2$. Hilz et al. [73] showed that the dark matter fraction within the radius containing half of the stellar mass increases more by minor mergers than by major mergers. Another property that get affected is metalicity profiles. Although recent dry mergers do not significantly affect the metallicity gradient, they are likely to flatten the metallicity profiles and enrich the metallicity [88, 48, 228]. Other properties, in general, that are significantly affected are stellar kinematics, including angular momentum [37, 152, 229] and kinematic misalignment [229], and the surface density profile [6, 73].

Another way in which two galaxies may interact occurs when one of the galaxies is embedded within the other galaxy; i.e., the halo of one of the galaxies is a subhalo, or satellite, of the other "host" galaxy. Dynamical friction causes the orbit of the satellite galaxy to decay and fall toward the center of the host halo where tidal stripping is more efficient. Such tidal stripping removes matter at larger radii from the satellite's halo owing to the large-scale tidal gravitational field of the host halo [16]. Studies of tidal stripping using hydrodynamical

cosmological simulations [181] have shown that the dark matter halo of the satellite always gets stripped more than its stellar matter; e.g., when a subhalo gets closer than $1.5 \times R_{\rm vir}$ ($R_{\rm vir}$ is the virial radius of the host halo), it could lose up to 80% of its dark matter halo [143].

Another way of interaction with the environment is when a galaxy infalls into a cluster causing a pressure, which is called ram pressure stripping [68], which might remove gas from the galaxy. This can drop the star formation rate to almost zero, but galaxies experiencing a mild ram pressure show an increase in star formation [193]. K. Yun et al. [230] showed that at $z \leq 0.6$, 30% of the satellite galaxies ($M_* > 10^{9.5}\ M_\odot$) with a massive host ($M_{200} > 10^{13}\ M_\odot$) shows ram stripped gas in the Illustris-TNG100 simulation.

1.2 Relic Galaxies

Although the great majority of ETGs at low redshift are expected to have experienced at least one major merger during their evolution, a small portion of the population has managed to avoid them. For massive ETGs (i.e., with stellar mass $M_* \sim 10^{11}\ M_\odot$) it is expected that $\sim 1\% - 10\%$ of the population have not experienced a major merger since $z \sim 2$ [75]. Since minor mergers are more common than major mergers, as shown, e.g., by the fact that the minor-merger pair fraction over the redshift range $0 < z < 3$ is at least twice the major-merger fraction between $z \sim 2$ and $z = 0$ for massive galaxies $> 10^{11}\ M_\odot$ [104, 34], and as just noted it is already rare for a massive galaxy not to experience a major merger, it is therefore even rarer that a galaxy does not undergo any kind of merger. However, owing to the stochastic nature of mergers, some red nuggets avoid their second phase of evolution so that, at low redshift, they are referred to as "relic galaxies" or "naked red nuggets". The extreme rarity of relic galaxies is testified by their low number densities found by observations [206, 185, 58, 173] and simulations [162].

The first confirmed relic galaxy observed was NGC 1277 [208] followed by Mrk 1216 and PGC 032873 [58]. Currently, there are many more candidates for relics [183, 226, 58, 185, 103]. These confirmed relics are ultra compact, which is believed to be extremely limiting the second phase of evolution. Due to scatter or differences in initial conditions (such as environment at $z = 2$) and the path taken by the evolution of a red nugget, a spectrum of relicness is introduced.

Relicness overall depicts where a relic resides in its evolutionary track. Initially, more extreme conditions were used to define relics that are later called extreme relics, but later many studies started using more relaxed conditions. The core of the definition to identify a relic is based on the limits used to define compactness. Since we expect these relics to not undergo the second phase, it is generally expected that the relic has an effective radius similar to the effective radius predicted from the size-stellar mass median relation at $z = 2$. For example, many picked an effective radius ($R_{\rm eff} < 2$ kpc) to define compact galaxies assuming the size-mass relation at $z = 2$ for massive ETGs. But some work has shown that during $1 < z < 2$, ETGs become larger when moving to a denser environment [23, 35], questioning the adaptation of $R_{\rm eff} = 2$ kpc while some other groups [79, 83] have shown that there is no correlation between $R_{\rm eff}$ and environmental density. The compactness criteria for the classification vary [213, 39, 153, 63]. On top of compactness criteria, some works have used additional criteria to classify relics. For example, de Arriba et al. [153] use stellar age. Since simulations provide the merger history and direct access to mass distributions at each snapshot, stellar and dark matter mass evolution from $z = 2$ to $z = 0$ and other properties are being used as metrics to define relicness [153, 59]. Due to the ambiguity in the definition of relicness, properties derived from relics could vary. Almost all of the observed relics show a larger velocity dispersion [184], low SFR [117]. Mrk 1216 and PGC 032873 show high dark matter concentrations [21] which begs the question: do relics have high concentrations?

Many decades ago, using N-body simulations, it was shown that under the Cold Dark Matter

(CDM) model, spherically averaged density profiles of relaxed halos who have come to an equilibrium are universal [134, 135]. This radial profile of the spherically averaged density (ρ) is modeled by Navarro-Frenk-White (NFW) profile (see Section 5) In this model, at scale radius (r_s) the logarithmic slope of the density becomes -2. Using this radius, the concentration is quantified as $c_\Delta = r_\Delta / r_s$ for $r \leq r_\Delta$. c_Δ depends on several factors such as halo mass, assembly time, environment, redshift. Wechsler et al. [220] showed that halos formed earlier have higher concentrations. Also, they showed, on average, halos which did not undergo a major merger since $z = 2$ have higher concentration than the total population. Furthermore, Ragagnin et al. [163] observed that fossil groups have high concentrations. Do these relics like Mrk 1216 have high concentrations due to their isolated environment or are they due to not undergoing mergers?

Furthermore, 15 local compact galaxies were identified that are suspected to resemble relics in the Yıldırım al. [226] study, host extremely large supermassive galaxies [226]. Cohn et al. [31] discuss the potential reason for the different properties of the galaxy UGC 2698 black hole mass ($M_{\rm BH}$). They show that $M_{\rm BH}$ of UGC 2698 are consistent with the three relationships, bulge luminosity ($M_{\rm BH} - L_{\rm bulge}$), stellar velocity dispersion ($M_{\rm BH} - \sigma_*$), and bulge mass ($M_{\rm BH} - M_{\rm bulge}$) while Mrk 1216, NGC 1277, and NGC 1271 which are also part of that catalog, shows a larger $M_{\rm BH}$ compared to the predictions by both bulge luminosity ($M_{\rm BH} - L_{\rm bulge}$) and bulge mass $M_{\rm BH} - M_{\rm bulge}$. They argue that UGC 2698 may have had a recent merger, which makes its $M_{\rm BH}$ agree with those scaling relations. Does that mean that relic galaxies have over-massive $M_{\rm BH}$ compared to predictions from $M_{\rm BH} - L_{\rm bulge}$ and $M_{\rm BH} - L_{\rm mass}$? It is not yet well explored whether the relics follow this property or not.

What kind of role does the galaxy environment play for the survival of those red nuggets is not clear yet. The first confirmed relic NGC 1277 resides in the highly dense Perseus cluster, which questions do relics prefer a dense environment? Later some observations [5, 17] and in simulations [194, 153] claimed that compact quiescent galaxies and relics are significantly

more likely to be found in dense environments, arguing that massive relic galaxies prefer dense environments, arguing that having a cluster in the neighborhood could protect cluster core members from mergers. But using a small sample of massive compact galaxies in Illustris and tracking their evolution from $z = 2$ to $z = 0$, S. Wellons et al. [221] argued that isolated galaxies at $z = 2$ experience little merger activity compared to the dense environment. In addition, Tortora et al. [202] claimed that the effect of the environment is mild. Later, it has been observed that some other relics such as Mrk 1216 and PGC 32872 reside in isolated environments [58]. This leads to the claim that the evolution of red nuggets in a dense environment might be different from that in a low dense environment [180].

1.3 Summary

The purpose of this thesis is to explore and study relic galaxies formed in the TNG300-1 hydrodynamical cosmological simulation and to compare them with candidate relic galaxies identified from observations. We develop metrics to define relic galaxies physically and examine whether they have the key stellar properties such as stellar mass-size and age as seen in the observations. We also explore what physical properties correlate with relicness (represents where a relic galaxy reside in the evolutionary track of a relic). Conversely, we use the stellar properties to define relic galaxies as used in observations and examine to what extent they match the physically motivated definitions of relic galaxies. We next examine the connection between high halo concentrations and relicness and explore the formation channels responsible for producing high-concentration relics and high-concentration halos generally. Finally, we also consider the connection between relicness, high concentration, gas fraction, and black hole mass.

In Chapter 2, we state the importance of exploring the mass-size relation in order to study relic galaxies mass-size relation.We derive the halo median stellar mass-size relation for ETGs

in TNG300 simulation. To have an accurate and robust comparison with observations, we implemented a dust model. We explore the changes needed to adapt (e.g., aperture, galactic center) in order to have a realistic comparison with the observations. We show that the size-mass relation for the simulation halos agrees well with the observed size-mass relation at both $z = 2$ and $z = 0$. Finally we explore dependence of galaxy stellar mass-size on other factors such as the used filter and aperture, which both showed the trend we see in the data from the observations.

In Chapter 3, we search for candidate relics in the TNG300 simulation. We start with the most basic definition using stellar mass and dark matter evolution from $z = 2$ to $z = 0$ and explore how relaxing the definition for relic changes the filtered sample. We explore what the best estimators are to define relicness. We show that out of overdensity based and fixed apertures, a 100 kpc aperture around the halo center is the best suited metric to define relic galaxies. Finally, we investigate the correlation between dark matter concentration and relicness and show that overall,relic galaxy candidates show concentrations above the median concentration-halo mass relation with some large outliers.

In Chapter 4, we examine various criteria in the literature to define relic galaxies and compare the results. We show that the definition used by Trujillo [206] is marginally better than other methods since its predictions match the physical criteria of stellar/DM fractions and stellar age better. Hence we use the Trujillo definition to select relics and categorize them into two categories, ultra-compact and compact. Then we analyze their stellar and dark matter mass evolution from $z = 2$ to $z = 0$. The analysis shows that 85% of the ultra compact relics agree with the relic definition used in Chapter 3. Our analysis of their dark matter profile reveals some key characteristics, such as a slightly higher dark matter concentration (c_{200}, c_{2500}), less dense environment at $z = 0$.

In Chapter 5, we compute dark matter concentrations for roughly 40,000 halos at $z = 0$. We assume an NFW profile and follow the method in Yangyao et al. [27]. Our $c_{200} - M_{200}$

median relation is in good agreement with Dutton et al. [53].

Chapter 2

Stellar Mass-Size Relation of Early-type Galaxies in TNG300 simulation

2.1 Introduction

As we discussed in Section 1.1.1, massive ETGs are believed to evolve through two broad phases. In particular, the second phase associated with the buildup of an extended stellar envelope proceeding slowly after the formation of the red nugget may be effectively probed by studying the redshift evolution of the stellar masses and sizes of ETGs. The stellar mass-size relation is perhaps the most fundamental and accessible way to define a relic galaxy, closely followed by an estimate of the stellar age and star formation history. Owing to its importance for our study of relic galaxies, we briefly review how well simulations of galaxy formation reproduce the observed mass-size relation for ETGs, describe our approach for computing it from a cosmological N-body hydro-dynamical simulation of galaxy formation,

and, finally, compare our results to previous work, with an emphasis on the most massive ETGs.

2.1.1 Definition

We offer a more exact definition of the elements comprising the mass-size relationship and examine the common methods employed to measure these components. Initially, we examine the stellar mass (M_*), which is commonly associated with the overall mass of a galaxy or a close approximation thereof. It has been derived from observations employing various methods that employ one or a combination of techniques such as photometry, stellar dynamics, X-ray emission, and gravitational lensing measurements. In all cases, it is the stellar light (i.e., luminosity) that is measured and the stellar mass that is derived from it, in the vast majority of cases, by assuming the mass-to-light ratio (M_*/L)[1] to be constant over the entire galaxy (some evidence for radial M_*/L variations is discussed later in the section). Total stellar luminosity is determined by measuring the amount of light within a certain spatial aperture and making corrections to estimate the amount of light outside of that aperture. These corrections typically assume a simple model of the spatial light profile, most commonly a Sersic model [174, see below]

The primary method to determine the stellar mass of a galaxy is through modeling of the spectral energy distribution (SED). An SED is the distribution of the flux radiated by all stars as a function of the wavelength of the emitted light (the process of creating an SED is built upon the work done by Tinsley [198], Spinrad et al. [186], and Faber [56]). The fundamental assumption of this method is that the emitted star light can be expressed as a summation of "simple" stellar populations – SSP (defined as "an ideal case of an ensemble of coeval stars all born in an instantaneous burst of star formation and with the same metallicity" [29]). The stellar mass of a galaxy is typically obtained by multiplying the luminosity by the

[1]The ratio between the stellar luminosity (in some band) and mass.

value of M_*/L obtained by fitting the SSP model to the observed SED. This technique has the great advantage of typically requiring only short telescope exposures in a small number of bands (or even just a single band) with the result that such telescope data are widely available in public archives and also very often with magnitudes published in the literature. In general, SED fitting yields stellar masses with constraints of roughly 0.2-0.3 dex[1], but, with the addition of near-infrared bands, this method can produce even better constraints [33, 131].

Although this method is frequently used in the community, it suffers from having a number of poorly constrained assumptions and models, the most important of which are the initial mass function (IMF), star formation histories (SFH), and abundances of heavier elements (metallicity). For example, there are many empirical functions that are used to describe the SFH (e.g., delta-function, exponential, constant) that are not always easily distinguished and with parameters that are only weakly constrained. Using cosmological simulations of galaxy formation considering all galaxy types with masses between $4.4 \times 10^7 M_\odot - 1.4 \times 10^{12} M_\odot$, Lower et al. [105] showed that differences in SFH models may result in variations in the stellar mass as large as 0.4 dex inferred from SED fitting.

Perhaps an even larger source of systematic error for SED models is the assumed model for the IMF [93, 26], which describes the number of stars as a function of the initial mass a star possesses when it first appears on the main sequence. The IMFs are empirical functions that do not derive from a well-understood fundamental theory of star formation. Consequently, it is unclear whether any of these simple functions can be universally applied to all stellar populations [203]. With these uncertainties in IMFs, the stellar mass estimates could vary largely even by as much as an order of magnitude for extremely dim dwarf galaxies [155, 171, 13], but only by about a factor of two (0.3 dex) for massive relic galaxies [226].

An alternative way to interpret M_*/L is by fitting the gravitational mass profile, which

[1]Order-of-magnitude; i.e., in base-10 logarithm

is done through multiple methods, most commonly by using stellar dynamics, but also by strong gravitational lensing and even through hydrostatic equilibrium analysis of the hot, X-ray emitting gas. The advantages and disadvantages of each of the probes used to measure the gravitational mass profile vary in terms of their spatial coverage and systematic uncertainties.

One effective approach to mitigate such drawbacks has been to integrate stellar dynamics with gravitational lensing to exploit the detailed spatial information in the gravitating mass profile provided by stellar dynamics with the precise and robust value of the total enclosed gravitating mass measured at the location of the Einstein radius provided by strong gravitational lensing. The stellar mass profile obtained from this method is fitted along with the other mass components to the total mass profile, typically by assuming that M_*/L is constant with radius. Building upon the foundation laid by Treu et al. [204, 205], where they demonstrate a successful disentanglement of the stellar and dark matter mass distributions, the stellar masses of several ETGs have been measured [90] and are in good agreement with photometric stellar mass estimates [66]. Although this method is promising, its application is limited only to those relatively rare systems that show measurable strong gravitational lensing features.

Constraints of similar quality, both in statistical precision and agreement with SSP models, have been obtained for the stellar masses for a small number of massive elliptical galaxies and galaxy groups via hydrostatic equilibrium analysis of extended, luminous X-ray emitting gas (e.g., Humphrey et al. [80], Gastaldello et al. [64], Buote [20]). A key advantage of this method is that it provides a useful probe of the mass profile much farther out into the halo, in many cases yielding precise constraints out to a radius of $\sim R_{2500}$[1].

Despite producing accurate measurements, this method is limited to nearby ETGs (i.e., within distances of about 100 Mpc). The main reason for the limitation is that for distant luminous X-ray halos (even extending out to R_{2500}) they do not produce good enough X-ray

[1] R_{2500} is defined based on the spherically averaged density. See Chapter 5 for more details.

data with current telescopes, due to their inadequate spatial resolution (even for Chandra[1], the sensitivity is far too low to allow galaxies to be studied at large distances). In addition to that, an additional source of systematic error arises from an uncertain contribution to the support of the X-ray plasma from non-thermal pressure, which is expected to be better constrained with data from microcalorimeter observations on future telescopes (XRISM[2], ATHENA[3]). (Courteau et al. [36] provide a more detailed review of different methods for estimating the stellar mass of a galaxy)

The next ingredient in the mass-size relationship we are going to examine is the "size" of the galaxy. While the size of an object may seem definitive, in the case of galaxies, where there is no definite boundary, the definition of the size becomes arbitrary. Since the very beginning of extragalactic observations, it has been observed that the surface brightness profiles of galaxies do not die out sharply with radius [166], consequently making it very difficult to define the edges of the galaxy precisely. The absence of a clear boundary can lead to the adaptation of a variety of definitions for the size. The definition of size commonly used in the community is based on the total luminosity and its surface brightness profile. Since there is ambiguity in defining the boundary, it is typically assumed that the light profile follows a specific function that allows extrapolation to infer the total luminosity.

The most popular choice for luminosity-based size is the radial distance containing half of the total light (luminosity in a chosen wavelength) of the galaxy (i.e., effective radius $R_{\rm eff}$). The selection of the fraction of one-half is completely arbitrary as any other fraction could be chosen, but, the mass evolution of the galaxy may not affect all radii equally. For example, as suggested by Miller et al. [121] and Mosleh et al. [125], choosing a radius that contains 20% of the total luminosity (R_{20}) is more closely related to in situ star formation, while similarly defined radius R_{80} is more sensitive to the accretion process that occurs in the outer regions

[1] `https://chandra.harvard.edu/`
[2] `https://heasarc.gsfc.nasa.gov/docs/xrism/`
[3] `https://www.the-athena-x-ray-observatory.eu/en`

of a galaxy. Therefore, due to its sensitivity to both phases in 2-phase galaxy evolution, $R_{\rm eff}$ is generally more appropriate for the study of the galaxy mass-size relation and its evolution.

The typical approach to estimate $R_{\rm eff}$ is to fit the surface brightness profile with a "Sersic" model [174]. The surface brightness at a radius R from the center of the galaxy (I(R)) is given by,

$$I(R) = I(R_{\rm eff}) \exp\left\{-b_n \left[\left(\frac{R}{R_{\rm eff}}\right)^{\frac{1}{n}} - 1\right]\right\} \tag{2.1}$$

where $R_{\rm eff}$ is the effective radius, n is called the "Sersic index" and, the coefficient b_n is chosen so that the $R_{\rm eff}$ encloses the half of the total luminosity. This results b_n to not have an analytical expression therefore an approximation has to be used. One of the approximations is given by the formula 2.2 (adapted from Ciotti et al. [30] and MacArthur et al. [107]).

$$b_n = \begin{cases} 2n - 0.324 & \text{if } n \geq 0.36 \\ 0.01945 - 0.8902n + 10.95n^2 - 19.67n^3 + 13.43n^4 & \text{if } n < 0.36 \end{cases} \tag{2.2}$$

One of the many reasons for the popularity of the Sersic fit is that it produces sizes that are generally less prone to varying image quality [69]. In addition to that, inferred sizes are barely affected by the depth of the images [210]. Although it is the most commonly used technique to estimate the size, some ETGs have displayed surface brightness profiles that deviate from the Sersic fit, possibly due to having internal structures [91, 77]. Dayari et al. [41] demonstrated that fitting multi-component (i.e., have internal structures) compact ellipticals with a single Sersic model (given by Equation 2.1) biases the inferred $R_{\rm eff}$ larger by $10\% - 20\%$.

An alternative approach to define the galaxy size is directly utilizing the stellar mass profile. The most widely adapted metric in this method is the half-stellar mass radius ($R_{\rm hm}$); the radius that encloses half of the total stellar mass of the galaxy. It has been observed that $R_{\rm hm}$ is smaller than $R_{\rm eff}$ for a given stellar mass, and the difference could be even greater than 25% [196, 195, 12]. Their work has suggested that M_*/L of local ETGs is radial dependent due to the variation in stellar population spatial distribution in the galaxies (i.e., the center is redder and outskirts are bluer). Although stellar mass-based radius does capture the physical processes in galaxies really well, it is computationally expensive and especially difficult to infer for high redshift galaxies.

Once the mass and size are estimated, there are two main ways to interpret the galaxy mass-size relation. Typically it is modeled as a power-law (in the form as in Equation 2.3) which provides a good broad description to the observations.

$$R_{\rm eff} = A \left(\frac{M_*}{M_p} \right)^B \tag{2.3}$$

where M_p is the arbitrarily chosen pivot mass, and A and B are the normalization constant and the slope, respectively. As we discussed in Chapter 1, the mass-size relation depends on the redshift; therefore, it is important to fit for a chosen redshift bin. The assumption that a power law fits well may not be valid for the whole mass range. We discuss the issues or concerns with the fitting procedure for obtaining a mass-size relation in Subsection 2.1.3). The other frequently used interpretation is the median size for stellar mass bins. In the following section, we will explore the historical development of the mass-size relationship of ETGs and how it gain insight into the process of galaxy formation.

2.1.2 Historical Background

The galaxy stellar mass-size relation has been in the spotlight in extragalactic astrophysics for decades, hoping it would clear up some unresolved questions at that time regarding galaxy formation (i.e., Are local ETGs remnants of major mergers of local disk galaxies? or they grow as described in 2-phase galaxy formation?). One of the first works to characterize the mass-size relation using a large local galaxy sample was done by Shen et al. [176] where they used a sample of 140,000 local galaxies ($z < 0.3$) from the Sloan Digital Sky Survey (SDSS). In addition to noting that the mass-size relationship for ETGs is steeper than that of LTGs, their results showed a log-normal distribution for $R_{\rm eff}$ for a given M_*. One of their major revelations was that the observed scatter in the $R_{\rm eff} - M_*$ relation for ETGs does not corroborate ETGs being remnants of present-day major mergers of disk galaxies.

Earlier, mainly due to the limitations of ground-based telescopes, it was hard to obtain a large enough sample of galaxies or/and accurate size estimations at larger redshifts to have a reliable mass-size relation. Following the introduction of space telescopes and the improvement of ground-based telescopes, ETGs have been reported to have significantly smaller sizes at $z \sim 1.5$ [38, 207]. Buitrago et al. [18] analyzed 82 massive galaxies ($M_* \geq 10^{11} M_\odot$) and confirmed that ETGs at $z \sim 2.3$ are roughly 4 times smaller than their local counterparts. Furthermore, they even argued that it is likely that the size growth halts beyond $z \sim 3$. This has led to a great deal of debate in the field as to what causes the size growth of ETGs with time. A variety of explanations have been suggested to explain the observed mass-size evolution. Here, we categorize the proposed explanations based on whether its physical or systematic.

1. Modeling bias

    - Overestimation of stellar masses and/or underestimation of sizes.

2. Accurate estimation of masses and sizes

    - progenitor bias
    - major merging
    - minor merging
    - Intrinsic expansion (due to internal processes such as quasar feedback)

First, it caught the attention of the community that masses are overestimated and/or the sizes are underestimated. Van Dokkum [215] proposed that the stellar masses could be overestimated at higher redshifts due to an incorrectly assumed IMF. As mentioned in Section 2.1.1, when the stellar masses are derived from a SED fitting, IMF is an ingredient of the stellar population synthesis models. Generally, the same IMF (e.g., Kroupa [93], Chabrier [26]) is used in mass modeling for both local and higher redshifts. Van Dokkum [215] proposed a different "bottom-light"[1] IMF for higher redshifts and conveyed that it lowers the previously inferred stellar masses. To test this hypothesis, Van Der Wel et al. [214] adapted a different definition to estimate the stellar mass that does not depend on an IMF. They used stellar velocity dispersion to derive a dynamical mass ($M_{\rm dyn}$) that ended up producing a mass-size relation ($M_{\rm dyn} - R_{\rm eff}$) similar to what has previously been observed, contradicting the hypothesis of overestimation in stellar masses caused by a different IMF.

The other side of the modeling bias is the underestimation of sizes. One of the potential candidates to explain was that ETGs may have strong radial gradients in M_*/L (i.e., M_*/L strongly depends on the radial distance) which introduce a bias towards smaller $R_{\rm eff}$. The analysis by Hopkins et al. [76] revealed that this type of M_*/L alone cannot produce the observed mass-size evolution. As near-infrared spectroscopy and telescopes have advanced, evidence has been mounting that ETG growth is not solely due to modeling bias [142, 211].

[1] having a deficit of low mass stars

After accepting that the observed growth of ETGs is not just modeling bias, the first candidate considered for the explanation was a statistical effect called "progenitor bias" (see Chapter 1). Bezanson et al. [14] showed that progenitor bias is not sufficient to explain this difference in mass-size relations in earlier redshifts. Furthermore, they explored the feasibility of the last three explanations in the list above. They used simple models to quantify the change in mass size for major mergers and minor mergers. The model they used for intrinsic expansion is motivated by the ability of a quasi-stellar object (QSO) to blow out a large amount of mass, resulting in a reduction in galaxy mass-size. Their general predictions for each model are shown in Figure 2.1. Their analysis concludes that the major mergers are in worst agreement with the observed local galaxy mass-size while the minor merger and intrinsic expansion by QSO are remarkably well in agreement. Additionally, they show that the intrinsic expansion model slightly underpredicts the central densities of elliptical galaxies.

The most promising explanation, which is minor merger-driven evolution, analytically predicts a larger growth in the effective radius ($\Delta R_{\rm eff}$) compared to the growth in the stellar mass (M_*). It is roughly followed by $\Delta R_{\rm eff} \propto M_*^2$ [14, 75]. This prediction based on the conservation of binding energy was tested using N-body simulations [132] and provided more support for minor mergers that are responsible for evolving high redshift ETGs into local counterparts.

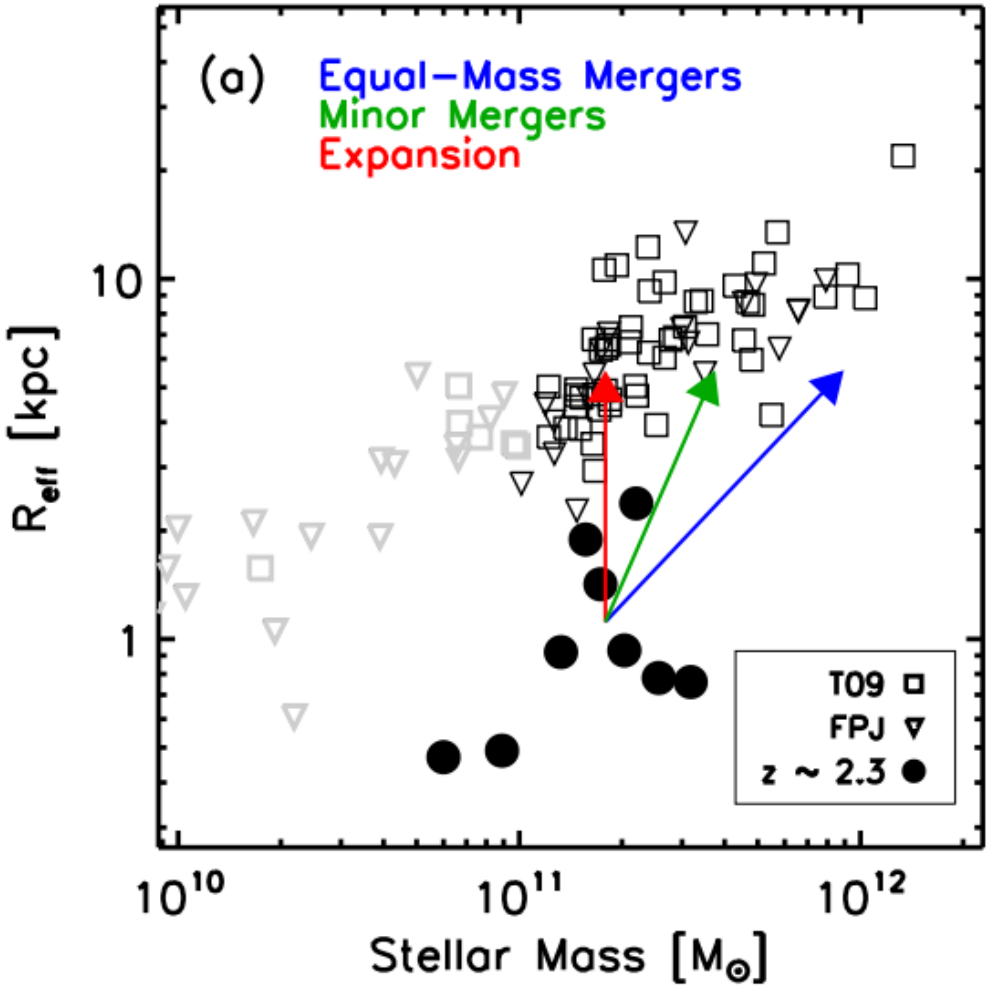

Figure 2.1: Open symbols are local galaxies, solid circles are high redshift compact galaxies from Kriek [92]. Light grey points are nearby galaxies with masses $< 10^{11} M_\odot$, i.e., lower than the high z compact galaxies. Arrows begin at mean values of high redshift sample and show predictions from simple models for the evolution of the compact galaxies: blue arrows shows the direction of evolution due to equal-mass mergers, green arrows for minor mergers and red arrows for the expansion model. (Figure from Bezanson et al. [14]. ©AAS. Reproduced with permission.)

2.1.3 Recent Developments

Over the last decade, the landscape of observational astronomy has experienced notable progress, characterized by the deployment of numerous large-scale surveys. One of them is the "Cosmic Assembly Near-Infrared Deep Extragalactic Legacy Survey" (CANDELS) which was carried out with near-infrared WFC3 and optical ACS camera on board the Hubble Space Telescope [89]. One of the biggest analysis of the galaxy stellar mass-size relation up to $z = 3$ is done by Van Der Wel et al. [213] (hereafter Van14). Figure 2.2 shows $M_* - R_{\rm eff}$, the median mass size for a sample of more than 30,000 galaxies in redshifts $0 < z < 3$. Their work further corroborates previous findings about the ETG evolution; i.e., grows physically in size with time (see Figure 2.2), the mass size follows a power law at all redshifts considered $0 < z < 3$.

Apart from those observations, their analysis reveals many more interesting properties of the mass-size relation. First, the median mass-size relation seems to flatten below $2 \times 10^{10}\ M_\odot$ (some other work has also shown this property for masses below $3 \times 10^{10}\ M_\odot$ [81, 172, 136]). Hyde et al. [81] investigated the cause of this curvature and argued that it was not caused by contamination at $M_* = 3 \times 10^{10} M_\odot$ or the effect of the aperture. This means that for the whole mass range, a double power-law in order is required to fit $R_{\rm eff}$ to M_*. Second, $R_{\rm eff}$ dependence on wavelength, which was previously observed by Barbara et al. [94] and later corroborated by [84, 85]. Their results indicate that the mean effective radius for ETGs decreases with wavelength. Kelvin et al. [84] argued that for local ETGs it could be mainly due to low levels of unresolved dust or the effects of AGN feedback in the core of the galaxy.

With the development of computational power, more advanced tools and robust methods have been introduced to extract galaxy sizes. For example, two-dimensional (2D) algorithms to implement a Sersic fit have been used in the last couple of decades with the employment of software such as GALFIT [151] and GIM2D [177]. Although $R_{\rm eff}$ extracted using these

different software are in reasonably good agreement, the GIM2D results are systematically biased toward higher Sersic indices, which can lead to systematic misclassification of the galaxy sample [70]. This happens if the Sersic index is used to distinguish ETGs from LTGs.

Despite the abundance of galaxy surveys that investigate the mass-size relationship and the deployment of more robust techniques to infer masses and sizes, there are still unresolved questions and issues. For example, there is little agreement on how the environment around galaxies affects the mass-size relation. Maria et al. [25] claimed that ETGs in less dense environments are 3.5% larger than their counterparts in highly dense environments. They argued that at earlier redshifts ($z > 1$) galaxies in highly dense regions could have gone through a faster growth than the galaxies in under-dense regions. However, in lower redshifts ($z < 1$), growth may have slowed in overdense regions, while in low-density regions, growth may have maintained or even increased. On the other hand, Moein et al. [126] demonstrated that $R_{\rm eff}$ of medium mass quiescent galaxies [1] in voids are $10 - 25\%$ smaller than their counterparts in groups and clusters. Yoon et al. [227] observed that local massive ETGs[2] are $20 - 40\%$ larger in $R_{\rm eff}$ in dense environments compared to their counterparts in underdense environments. Their argument is that massive galaxies residing in a dense environment undergo more major and minor mergers than their counterparts in underdense environments, resulting in larger galaxies in highly dense environments. They also observed that there is negligible environmental dependence on the environment density for galaxies with $10^{10.7} M_{\odot} \leq M_{*} < 10^{11.2} M_{\odot}$.

However, there are some studies [111, 133] that oppose this claim, in which they found no dependence on the environment for $z < 0.3$. In general, these studies suggest that the dependence on the environment depends on the range M_{*}. This disagreement with some other work could be due to a small sample size [227] or/and definition of environment [7] or/and due to the biases introduced in sample selection methods [172].

[1] $10^{9.8} M_{\odot} < M_{*} < 10^{11.2} M_{\odot}$
[2] $0.1 < z < 0.2$ and $M_{*} > 10^{11.2} M_{\odot}$

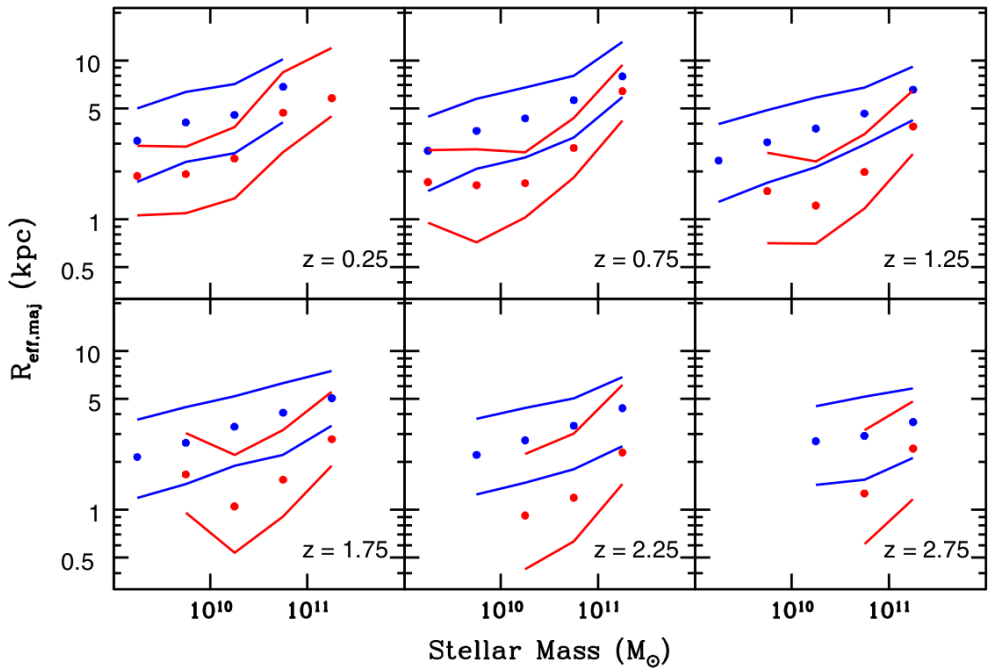

Figure 2.2: Median (points) and 16th and 84th percentiles (lines) of the size–stellar mass distributions at different redshift bins. Red (blue) represents ETGs (LTGs). (Figure from Van Der Wel et al. [213]. © AAS. Reproduced with permission.)

Another issue is that mass-size analysis often has a variety of statistical effects that vary from study to study. For example, sample bias can be caused by having fewer massive ETGs[1]. One way to avoid such bias is to weight the sample according to the number density of each mass bin (weight $\propto 1/$(number density)) [213]. Another example is the uncertainty in galaxy classification (i.e., categorization into ETGs and LTGs). In general, the $u-r$ vs. $r-z$ color-color diagram is used to classify galaxies (see Chapter 2.2.3). Although most galaxies separated well into two types by a boundary, some galaxies are in the region between two types [74]. Van der Wel et al. [213] employed a probability of misclassification in their Bayesian fitting to reduce the impact of misclassification.

2.1.4 Implementation in Cosmological Simulations

Upon the development of more accurate hydrodynamical simulations which include baryonic physics, a new platform emerged to explore the galaxy mass-size relationship. In simulations, you have access to data in phase space for all the stellar particles up to the boundary of the halo identified by the halo finder algorithm. Therefore, it opens up an opportunity to adapt different definitions for galaxy mass and size. There are two main approaches to extract $R_{\rm eff}$. The first approach is to generate images that resemble optical images obtained from observations and then follow the procedure to extract a half-light radius by fitting a Sersic fit as done in observations. Only a few studies have employed this method [169, 148, 43]. The other approach is to use the stellar particle distribution straightforwardly. Some studies use light distribution to fit a 1 dimensional Sersic fit to extract the effective radius [224] while others have used nonparametrical (without using any fit for the surface brightness profile) half-light radius [65, 167] or half stellar mass radius [62, 219, 118, 165]. There are slight variations in the definitions adapted in these works, which are explained in Table 2.1.

[1]This is also theoretically predicted by the halo mass function [161], which predicts that low-mass galaxies are more abundant than high-mass galaxies for a given redshift

Do cosmological simulations produce a comparable mass-size relationship? Overall, they agree with the observations regarding the trend, but values for the fitted parameters or median size values could be different from the observations. Figure 2.3 shows the median sizes ($R_{\rm eff}$) for different stellar mass bins and the difference between them could be due to the difference in the methods used to extract $R_{\rm eff}$. For example, Genel et al. [65] used a circularized projected half-light radius for the simulation TNG100-1 [115] and their median sizes of ETGs for mass bins $> 10^{10.5} M_{\odot}$ are roughly 2 kpc larger than the Van14 at $z = 0$. For the EAGLE simulation, Graaf et al. [43] showed that their $R_{\rm eff}$ derived from the 2-D Sersic fit is typically 0.1-0.5 dex larger than $R_{\rm hm}$. More interestingly, their results showed that $R_{\rm hm}$ of quiescent galaxies agree more with observations from GAMA [98] than with $R_{\rm eff}$. They argue that it is merely a coincidence. Regarding the 1-D Sersic fit, it has shown that $R_{\rm eff}$ has roughly a maximum deviation of 2 kpc from the observations at higher stellar masses [224] (the power law fit has been done for galaxies with $M_* \geq 9 \times 10^{10} M_{\odot}$ and compared to the observational results by Hyde et al. [82]).

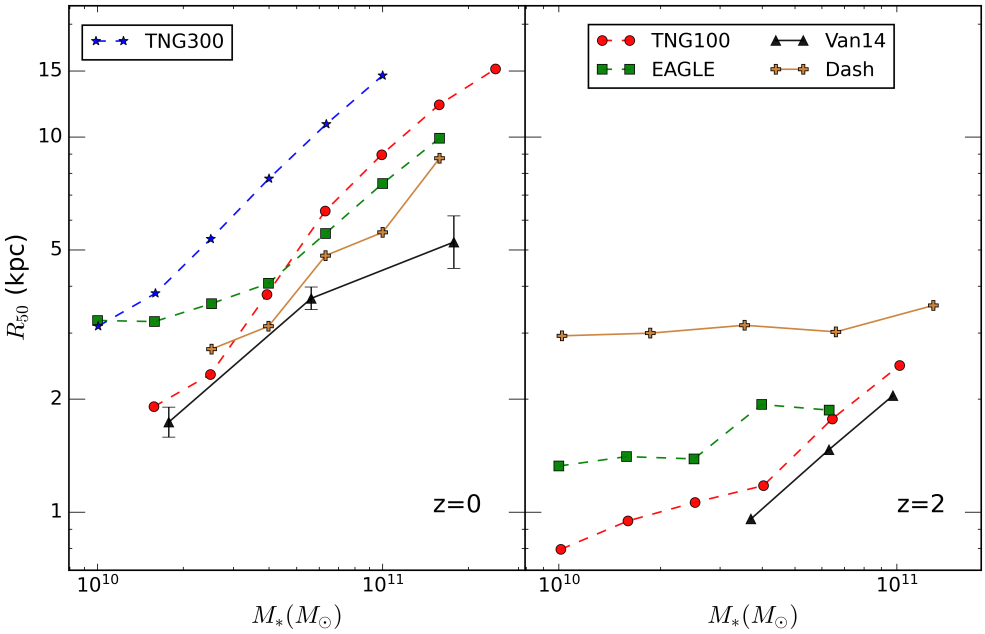

Figure 2.3: Median stellar mass-size for latest cosmological simulations in the literature compared with Van1 and Dash (data from Mowla et al. [128]). Left (right) panel is for redshift (2). TNG300 [167] and TNG100 [65] r-band half-light radius projected on z-axis. Eagle [62] and shows half stellar mass radius. Dashed (solid) lines represents data from simulations (observations). In the right hand panel both observational data are for the redshift bin $1.75 < z < 2$.

Bridging observations and simulation results for comparison is not straightforward. One of the major differences in simulations is that massive ETGs have stellar particle data up to several hundreds of kpc as opposed to observations where you are limited by the light profile, which dies out at a short distance (in the highest resolution light curve available for Mrk 1216, the light curve extends to a radial distance of roughly 35 kpc [225]). This leads to an addition of a structure (named "intracluster light" (ICL)) to the light profile that exists at a large radial distance in simulations. ICL around a central galaxy of a galaxy cluster was first noticed by Zwicky [232]. It has shown that at low redshifts, ICL have a characteristic radius almost independent of the mass and because of its low brightness it does not capture observationally in most galaxies [197]. Therefore, including the ICL in simulations leads to an overestimation of the mass and size of the halos.

A further difficulty is to incorporate the impact of dust on the stellar radiation in these simulations. Xu et al. [224] showed that dust-corrected luminosities produce a galaxy luminosity function closer to the observations compared to raw luminosities without dust correction in the simulation Illustris-1. Only a handful of studies have implemented dust modeling for simulations data (e.g., for the simulations Illustris-1, TNG100-1, TNG50-1 [169] and for EAGLE [43]). In addition to that, simulations having different physics models could contribute to producing the mass-size relationship different from the observations. For example, using the FIRE-2 zoom simulation, Parsotan et al. [148] showed that the lack of active galactic nuclei (AGN) feedback results in an underestimate of galaxy sizes at redshift $z < 2$.

Table 2.1: Different definitions used in simulations to define galaxy size and stellar mass. The columns contain the name of the simulation, then method which describes whether it used a parametric (P) or non-parametric (NP) method and effective radii derived using light or mass profile, dimension whether stellar mass or light is projected on a plane (2-D) or not (3-D), and final column describes if a radial cut is implemented or not.

Simulation	Method	Dimension	Description
TNG300-1	NP-L	2-D	all particles considered
Illustris-1	P-L	2-D	all particles considered
TNG100-1	NP-L	2-D	particles within 2× stellar half-mass radius
EAGLE:Ref-L100N1504	NP-M	3-D	particles within 100 kpc
Magneticum Pathfinder	NP-M	3-D	all particles considered

This chapter is organized as follows. Section 2.2 gives an overview and structure of the TNG300 simulation and the method we implemented to derive the mass-size relationship for ETGs in TNG300. In section 2.3 we analyze our mass-size relationship results and compare them with other studies in the literature. Finally, Section 2.4 provides our conclusions.

2.2 Simulating ETGs with TNG300

In present-day there are a lot of hydrodynamical simulations, yet each has a trade-off balance between resolution and the size of the simulation box, i.e., while high-resolution simulations have fewer halos (e.g., TNG50), larger simulations have low resolution (e.g., Magneticum). On the contrary, high-resolution simulations have fewer halos. The comparison between different hydrodynamical simulations is shown in Table 2.2. To obtain a larger sample size of halos (i.e., having a larger number of ETGs will result in a higher chance of identifying a larger number of massive relics) while avoiding low-resolution effects, we choose Illustris TNG 300 [137]. As we have demonstrated in Table 2.1, to our knowledge, no one has studied so far the mass-size relation robustly for TNG300 but only half-stellar mass radii. Therefore, we chose TNG300 as our laboratory to examine the mass-size relationship and search for relic galaxies.

Table 2.2: Properties of different hydrodynamical simulations. The columns contain the name of the simulation, minimum value of softening length of gas particles, the box size at $z = 0$, and the total number of halos at $z = 0$.

Simulation	$\epsilon_{\rm gas}$ (kpc)	$L_{\rm box}$ (Mpc)	$N_{z=0}$
Illustris TNG300-1	0.37	205	14485709
Illustris-1	0.7	1.94	4366546
Illustris TNG100-1	0.18	75	4371211
Illustris TNG50-1	0.07	35	5688113
Magneticum Box0/mr	14.76	3968	329648[a]

[a] The number of halos with $M_{200} \geq 12 \times 10^{13} M_{\odot}$.

2.2.1 TNG300

TNG300 simulation has 3 versions with distinct resolutions. We consider the highest resolution (TNG300-1). We use publicly available[1] raw data from the hydrodynamical cosmological simulation TNG300-1 [139] (hereafter referred to as TNG300). It uses the quasi-Lagrangian code AREPO [187] to solve coupled dynamical equations of dark matter and gas. They start from the initial conditions for the universe from Planck 2015 observations [158].

The galaxy formation model of this simulation includes magnetohydrodynamics, isotropic galactic winds (an improved version of older simulations), and modified black hole-driven kinetic feedback [157]. It assumes a Chabrier initial mass function [26, 218] for the stellar evolution model. The star formation column density ($n_{\rm H}$) threshold for gas to form stars is ~ 0.1 cm^{-3} and the pressurization of the multiphase ISM is treated as in the Springel & Hernquist model [188].

The simulation physics runs in a periodic cube of 304 cMpc (in comoving units), and a total of 100 snapshots spanning redshifts $z = 20$ to $z = 0$ are publicly available. For each snapshot there are 4 types of resolution elements (particles): gas, dark matter, stellar and stellar wind, and black holes. Dark matter is simulated using N-body methods to follow the pure gravitational dynamics of dark matter particles. The behavior of dark matter particles is determined by a combination of the collisionless Boltzmann equation and the Poisson equation, which keeps the mass of the particles constant throughout the simulation. A softening length is imposed for the gravitational interactions in order to prevent close encounters. For dark matter, stellar and wind particles are fixed at a comoving value of 1.48 kpc until $z = 1$ and after that the value of 1.48 kpc up to $z = 0$. The gas particles have adaptive gravitational softening ($\epsilon_{\rm gas} = 2.5\, r_{\rm cell}$), where $r_{\rm cell}$ is the radius calculated assuming the Voronoi gas cell[2] is a sphere. The mass resolution is set to $1.1 \times 10^7\ M_\odot$ for baryons and

[1] `https://www.tng-project.org/data/`

[2] Constructed through a Voronoi tessellation of space

$1.1 \times 10^7\ M_\odot$ for dark matter.

In the simulations, the standard Friends of Friends (FoF) [42] and SUBFIND [190] algorithms are used to identify group structures. FoF algorithm runs only on DM particles and uses a linking length[1] $b = 0.2$. FoF-grouped structures are referred to as "halos". The boundary of a halo has some fuzziness that depends on the number of particles it has [124]. More et al. [124] showed that the boundary does not correspond to a specific density threshold, but to a range of densities around a critical value. For the adapted link length (b = 0.2), the critical density is 81.62 times the mean matter density.

The structures inside these halos are classified using a modified version of the original SUBFIND algorithm [49] which is named the "subhalo". A subhalo has at least 20 particles of any type gravitationally bound together. The most massive subhalo of a halo at a given snapshot is called the "primary" subhalo. The primary subhalo may change to secondary if there is a more massive subhalo identified by the SUBFIND algorithm inside the host halo.

The particle with the least gravitational potential in a halo (subhalo)is considered to be the center of the halo (subhalo). The primary subhalo and its parent halo share the same center. For a given snapshot half-stellar mass ($R_{\rm hm}$) is the 3-D radius that encloses half of the stellar mass[2] (M_*).

[1] Any particle that finds another particle within a distance b is linked to it to form a structural group.
[2] Stellar mass includes all the stellar particles that belong to the subhalo.

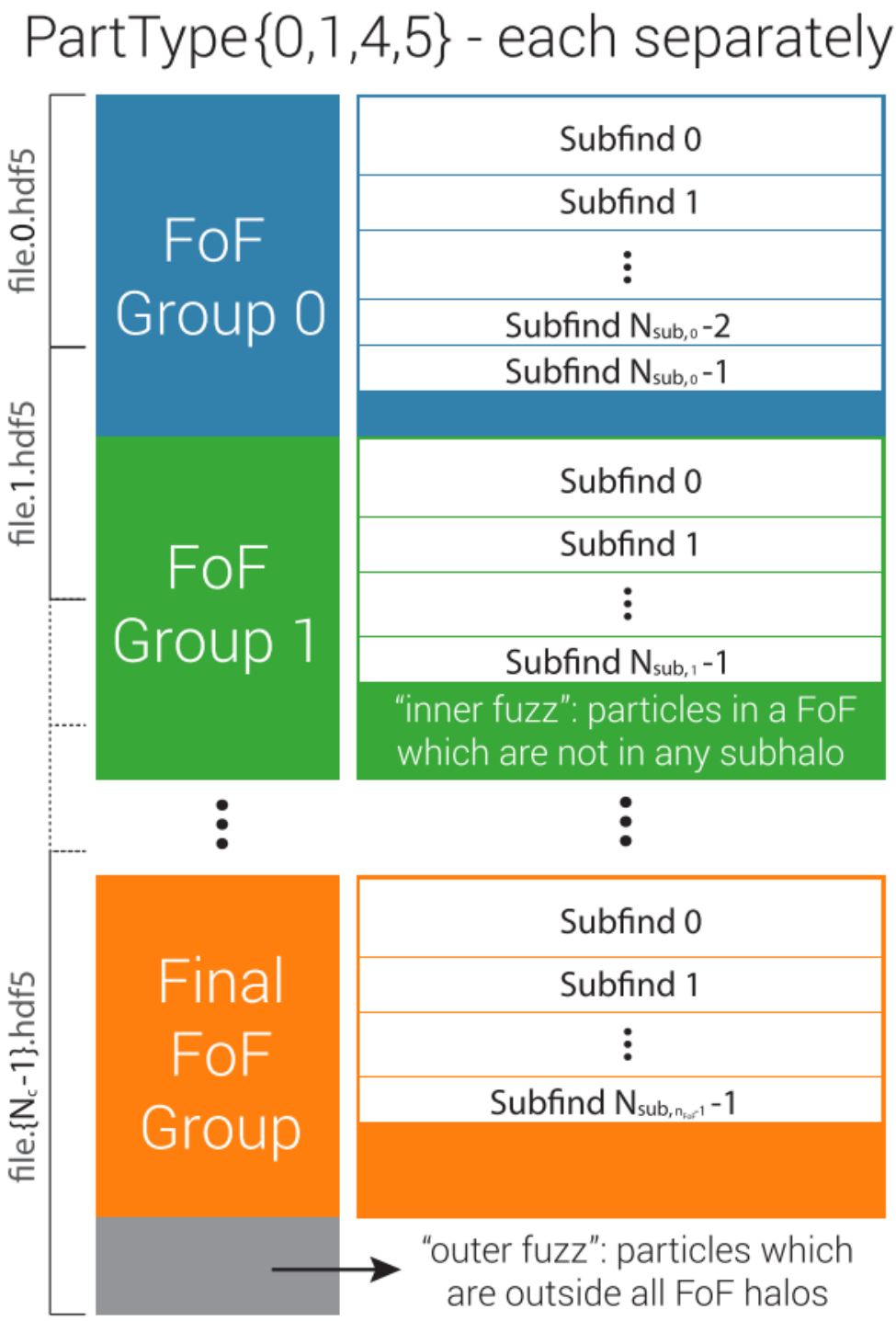

Figure 2.4: The organization of particles data for a snapshot for each particle type. Particle order is set by a global sort of the following fields in this order: FoF group number, Subfind subhalo number, binding energy. Each particle for a given particle type is assigned to halo/subhalo and labeled according this structure in TNG300 simulation (Figure from Nelson et al. [139]).

2.2.2 Halo Selection

All selected subhalos are identified by the Subfind algorithm and the data is available publicly. The first step in selecting ETGs is based on M_{200}[1] (which is publicly available). We are mainly motivated by the isolated relic galaxy Mrk 1216; therefore, we chose only primary subhalos to avoid environmental interactions such as tidal effects, flybys, and ram pressure to some extent (this criterion alone will not remove ETGs suffered with flybys and other tidal effects, but it will remove a significant amount of those interactions). The conditions for the selections are as follows.

- $10^{12} M_{\odot} \leq M_{200} \leq 5 \times 10^{13} M_{\odot}$.
- Primary subhalo at $z = 0$ and $z = 2$.
- Subhalo flag = 1.

M_{200} is the total mass within R_{200} where R_{200} encloses $200 \times \rho_c$ (For more details see Section5). Publicly available M_{200} has been calculated considering all types of particles.

The subhalo flag indicates whether the subhalo has a cosmological origin or not. Not all objects recognized by the Subfind considered to be "galaxies". Some subhalos may not have collapsed as a result of the structure formation process. The subhalo flag = 1 indicates that the subhalo structure has collapsed from the galaxy formation model and has enough baryonic mass.

2.2.3 ETGs

In this section, we discuss how we categorized the sample into the two types of galaxy based on star formation. We then compare two methods and choose the best method to classify

[1] All particle types (i.e., gas,stellar,dark matter,black holes) is being considered to calculate M_{200}

galaxies based on their star formation.

There are two main types: Early-type galaxy (ETG) and late-type galaxy (LTG) based on stellar activity. There are many classifiers with different parameters used for identification [213]. Mainly based on specific star formation rates (sSFR) or UVJ magnitudes.

First, we use UVJ magnitudes to classify galaxies using $U-V$ vs $V-J$ plane. We use publicly available dust-corrected UVJ magnitudes [138, 51] to classify galaxies into ETGs and LTGs. Each magnitude is calculated only considering luminosities of stellar particles within 30 kpc from the subhalo center. We use the following conditions used by Muzzin et al. [130] to classify ETGs,

$$\begin{aligned} U - V - 0.88(V - J) - c &> 0 \\ U - V - 1.3 &> 0 \\ 1.6 + J - V &> 0 \end{aligned} \tag{2.4}$$

where c = 0.69 for $z \leq 0.5$ and c = 0.49 for $1 \leq z \leq 2.5$.

In Figure 2.5, we show that the two categories ETG and LTG. The top (bottom) panel shows galaxies at redshift 0 (2). At $z = 2$ all galaxies are classified as ETGs. For the same classification, Figure 2.6 shows the number of subhalos in each stellar mass bin. Red (Blue) represents the ETGs (LTGs).

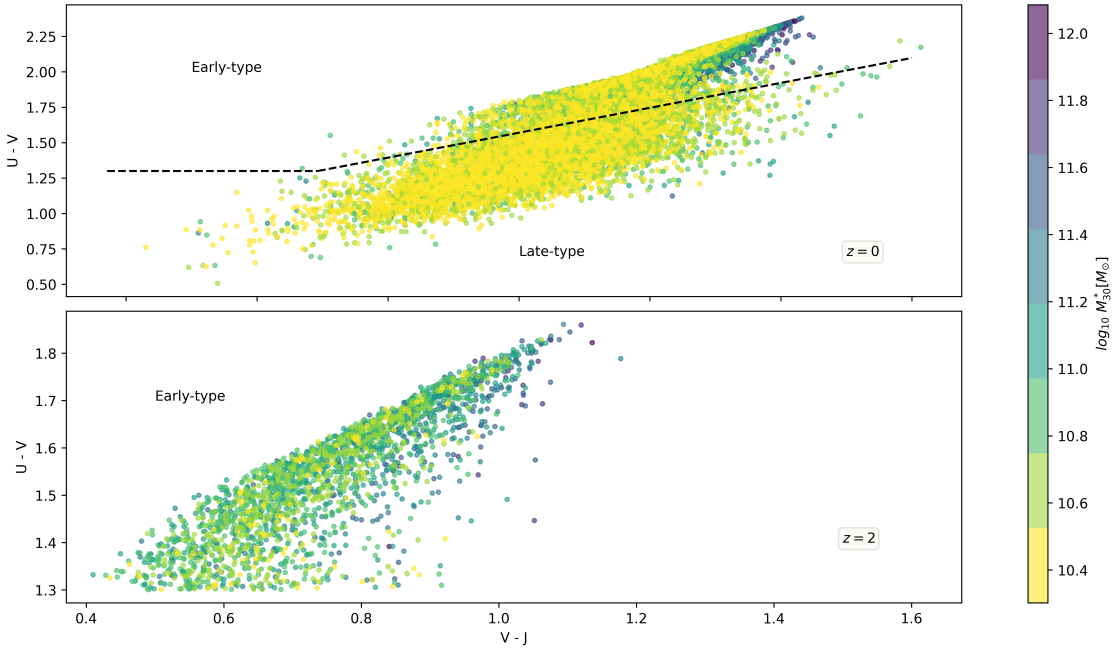

Figure 2.5: ETG and LTG classification based on $U - V$ vs $V - J$ plane. The color bar represents the log of stellar mass within 30 kpc from the galactic center. The top (bottom) panel shows galaxies at redshift 0 (2). Dust corrected U, V, J stellar magnitudes are taken from publicly available UVJ magnitudes [138, 51]. Each dot represents primary subhalos we selected from the simulation TNG300. Dashed lines represent the boundary dividing the sample into LTGs and ETGs according to the conditions 2.4.

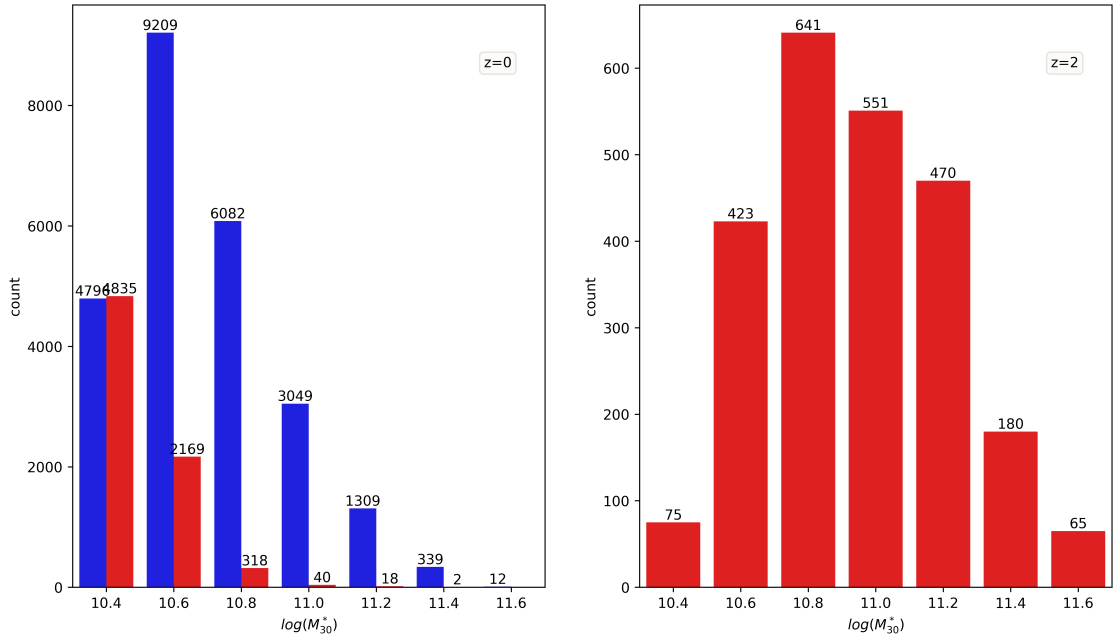

Figure 2.6: Stellar mass number distribution of the sample subhalos. Red (Blue) represents the ETGs (LTGs). Left (right) plot is for redshift 0 (2). Stellar mass is the total stellar mass within 30 kpc from the galactic center.

Next, we adapt the classification criteria used by Genel et al. [65] which they used in the simulation TNG100-1. We identify ETGs as subhalos for stellar masses $10^9 M_\odot \leq M_{*30} \leq 10^{11} M_\odot$ with a specific star formation rate[1] (sSFR), $\log_{10}(\text{sSFR})[\text{Gyr}^{-1}] \leq -1.94$ for $z = 0$ and $\log_{10}(\text{sSFR})[\text{Gyr}^{-1}] \leq -1.94$ for $z = 2$. We used publicly available sSFR data [51] calculated only considering stellar particles within 30 kpc of the subhalo center.

To compare with the UVJ method, we plot subhalos classified in Figure 2.7. Red (blue) dots represent ETGs (LTGs). At redshift 2, both methods agree well with each other, but for $z = 0$, there is some disagreement. Steinhardt et al. [192] demonstrated that in UVJ classification, some galaxies with large sSFR can be incorrectly classified as ETG and Sanchez et al. [50] showed that actual ETGs can be labeled as LTG. The figure 2.7 shows this trend, which implies that the sSFR-based method is more accurate. Furthermore, the method used in Xu et al. [224], where they pick the best fit from the Sersic and de Vaucouleurs [44]

[1]Only considering stellar particles within 30 kpc from the subhalo center.

profiles, is a bit arbitrarily and sensitive to the radial bins used for the fit. Additionally, not all ETGs have a light profile that follows a perfect 1-D Sersic fit (see Section 2.1.1). Therefore, since the simulation provides star formation rates with good time resolution, we adapt the latter definition to classify the subhalos based on the star formation activity.

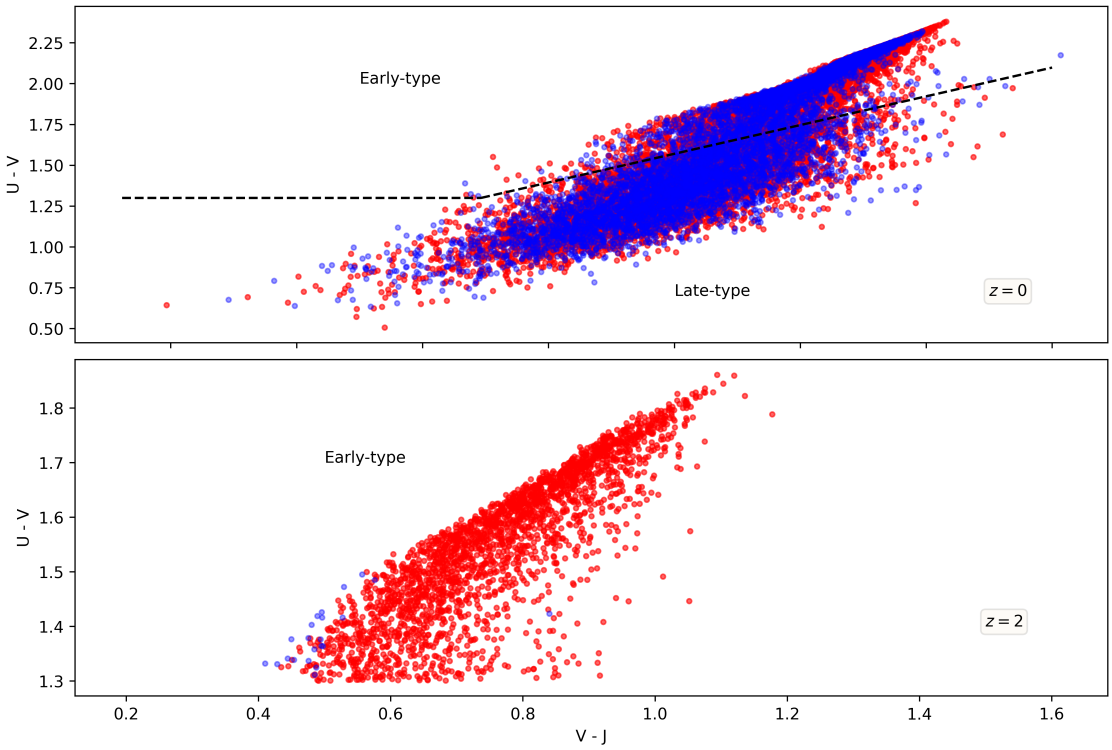

Figure 2.7: ETG and LTG classification based on specific star formation rates (sSFR). Red (Blue) dots represents ETGs (LTGs). The top (bottom) panel shows galaxies at redshift 0 (2). We used publicly available sSFR data [51]. Each dot represents primary subhalos we selected from the simulation TNG300. Dashed lines represent the boundary dividing the sample into LTGs and ETGs according to the conditions 2.4.

2.2.4 Dust Modeling

To model the dust attenuation, we followed the procedure in Xu et al. [224]. We only consider the gas and stellar particles within $3R_{\rm hm}$ from the subhalo center(from the Subfind algorithm) to calculate the average neutral hydrogen column-density ($\langle N_{\rm HI}\rangle$). First, we consider a mesh grid 100×100 in the x-y plane that spans from $-3R_{\rm hm} - +3R_{\rm hm}$ centered around the subhalo center. We use publicly available data for gas particles inside the grid. For each cell (i, j) we calculate a mean neutral hydrogen density $\langle N_{\rm H}^{(i,j)}\rangle$ using the pysph library [164] in python to scatter the fractional hydrogen cold masses of each gas cell onto the mesh cell (i, j). We assume that gas particles can be approximated by a density profile related to the SPH kernel $W(r, r_{\rm SPH})$ that is given by

$$W(r, r_{\rm SPH}) = \frac{8}{\pi r_{\rm SPH}^3} \begin{cases} 1 - 6q + 6q^3 & 0 \leq q \leq \frac{1}{2} \\ 2(1-q)^3 & \frac{1}{2} \leq q \leq 1 \\ 0 & 1 \leq q \end{cases} \tag{2.5}$$

where $q = \frac{r}{r_{\rm SPH}}$

Then the mean neutral hydrogen density($\langle N_H^{(i,j)}\rangle$) is given by,

$$\langle N_H^{(i,j)}\rangle = 2 \times 0.76 \left(\frac{\rm HI}{\rm H}\right)^k \left(\frac{m^k}{m_{\rm H}}\right) \int_0^{l_{\rm max}} W(r, r_{\rm SPH})\, dz \tag{2.6}$$

where m^k is the total mass of the k-th gas particle inside the mesh grid cell (i, j).

We consider both dust attenuation from absorption and scattering. The optical depth from

absorption (τ^a),

$$\tau_a^{(i,j)} = \left(\frac{A_\lambda}{A_V}\right)_{Z_\odot} \left(\frac{Z_g}{Z_\odot}\right)^s (1+z)^\beta \frac{\langle N_{\rm H}^{(i,j)} \rangle}{2.1 \times 10^{21} {\rm cm}^{-2}} \tag{2.7}$$

where Z_g is the gas metallicity of the galaxy, $\left(\frac{A_\lambda}{A_V}\right)_{Z_\odot}$ is the solar-neighborhood extinction curve. $\beta = -0.5$, s = 1.35 for $\lambda < 2000\,$Å and s = 1.6 for $\lambda > 2000\,$Å. $Z_\odot = 0.2$

Taking into account isotropic and forward only scattering, the total optical depth ($\tau^{(i,j)}$) for the cell (i,j) is given by

$$\tau^{(i,j)} = h_\lambda \sqrt{1-\omega_\lambda} \tau_a^{(i,j)} + (1-h_\lambda)(1-\omega_\lambda)\tau_a^{(i,j)} \tag{2.8}$$

where ω_λ is the albedo and h_λ is the weighing factors for the isotropic scattering.

$$h_\lambda = 1 - 0.516 e^{-(|y-3.3112|^{2.2}/0.17)} \tag{2.9}$$

and,

$$\omega_\lambda = -0.48y + 2.41 \tag{2.10}$$

where $y = \log(\lambda)$. For a star particle in cell (i,j) we interpolate optical depth (τ) by using

the $\tau^{(i,j)}$ of the 4 neighboring cells. Dust corrected luminosity($L_{\rm crtd}$) is given by,

$$\frac{L_{\rm crtd}}{L_{\rm raw}} = \frac{1 - \exp(-\tau)}{\tau} \tag{2.11}$$

$L_{\rm raw}$ is the luminosity derived from the publicly available stellar magnitudes which are calculated according to the model in Vogelsberger et al. [218]. Dust effects are not considered for these magnitudes.

2.2.5 Method to Compute Stellar Masses and Sizes

Since TNG300 provides the luminosities of all the stellar particles that belong to a halo, there is the luxury to infer the half-light radius accurately without modeling the light profile (unlike in observation where the boundary of the galaxy cannot be observed clearly. See more the discussion in Section 2.1.1). Since nonparametric methods produce robust enough $R_{\rm eff}$ and to avoid complications occurring when the Sersic model is employed for multi-structural ETGs [127], we chose the half-light radius as the size estimator of a halo. Therefore, we followed the first half of the procedure in Xu et al. [224] to define the galaxy size, but we did not follow their method of using the Sersic fit. Here, we explain the procedure for computing the half-light radius.

SUBFIND center was chosen as the initial point. Then calculate new light centeroids ($Xc = x_c, y_c$) for an aperture $3R_{\rm hm}$ from the initial center,

$$Xc = \frac{\sum_i L_i X_i}{\sum_i L_i} \tag{2.12}$$

where, L_i is the dust-corrected luminosity of the i th gas particle, and X_i is the appropriate coordinate of the i th gas particle in the periodic box.

In order to calculate half-light radius, we assume that the 2-D surface brightness profile follows a series of elliptical isophotes with a constant axis ratio (b/a) and orientation angle (ϕ). We evaluate b/a and ϕ using equations 2.13 at a distance of $3R_{\rm hm}$ from the centeroid (Xc).

$$\begin{aligned} M_{XiXi} &= \frac{\sum_i L_i (X_i - X_{ci})^2}{\sum_i L_i} \\ M_{XiXj} &= \frac{\sum_i L_i (X_i - X_{ci})(X_j - X_{cj})}{\sum_i L_i} \end{aligned} \tag{2.13}$$

The axis ratio (b/a) is given by,

$$(b/a)^2 = \frac{M_{xx} + M_{yy} - \sqrt{(M_{xx} + M_{yy})^2 + 4M_{xy}^2}}{M_{xx} + M_{yy} + \sqrt{(M_{xx} + M_{yy})^2 + 4M_{xy}^2}}. \tag{2.14}$$

The orientation angle is given by the following.

$$\phi = 0.5 \, \tan^{-1}\left(\frac{2M_{xy}}{M_{xx} - M_{yy}}\right) \tag{2.15}$$

In order to avoid ICL, a 30 kpc radial cut-off is introduced as done in other work [224, 43]. Here, we chose 30 kpc from the galactic center, as used in the paper [224]. Hence the total luminosity ($L_{\rm tot}$) is the sum of luminosities of the stars within a radius of 30 kpc. Finally, using $L_{\rm tot}$, we calculate the circularized half-light radius ($R_{\rm eff}$) which corresponds to the isophote enclosing a luminosity of $0.5\,L_{\rm tot}$.

2.2.6 Mass−Size Relation

Figure 2.8 shows the median size-stellar mass relationship for ETGs at redshift=0. We explore the best estimator for galaxy size by comparing it with the observations. The dashed (solid) lines represent data from observation(derived results from the simulation data). The teal color represents half-light radius for raw luminosities and without the 30 kpc radial cut-off. That means that it captures all the stellar particles that belong to the halo. The red color line is half-stellar mass radius with a 30 kpc radial cutoff. The yellow line shows the circularized half-light radius for dust-corrected luminosities and the 30 kpc radial cut-off. All the light-based radii are for filter r luminosities. Green, black, and blue dashed lines show data from Van14 [213], Sloan Digital SkyServer Data Release 7 [120], and DASH [128] respectively.

By fitting a power law for subhalo $M_* - R_{\rm eff}$, we compare the subhalo size-mass relationship with observations [213, 128](Figure 2.9). We used the best estimator the effective radii ($R_{\rm eff}$) for galaxy size which includes dust correction. Red line is the minimum chi-squared best fit created by using the Scipy regression package [217] in Python. For this fit we did not include complex statistical methods to remove outliers or sample bias from having less halos in massive mass bins.

We also compute the median size-mass relation for redshift 2 (Figure 2.10) using a process similar to that we used for $z = 0$. We explore the best estimator for galaxy size which is closest to the observations. The dashed (solid) lines represent data from observation(derived results from the simulation data). Since the observations Van14 [213] have a wider redshift bin for $z = 2$, unlike the simulations, we include both redshift bins $1.75 \leq z < 2$ and $2 \leq z < 2.5$.

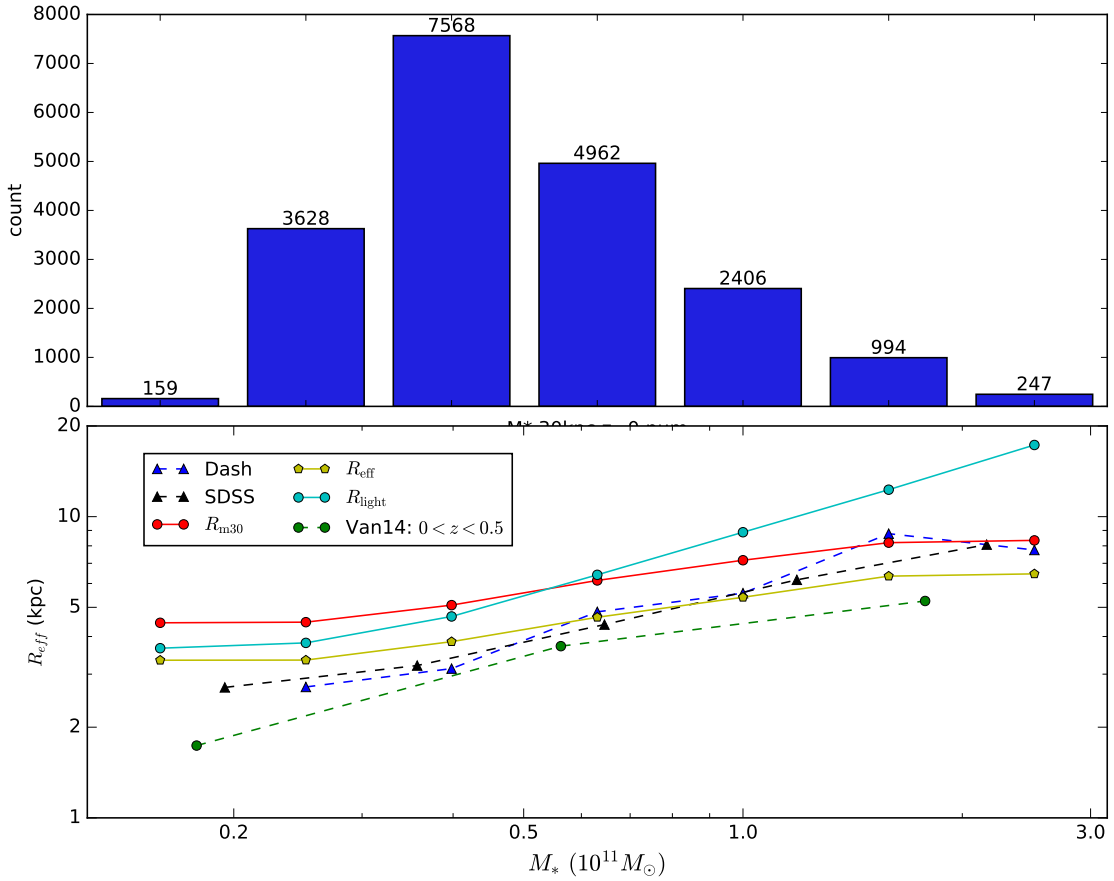

Figure 2.8: Median mass-size relation at $z = 0$ for Early-type galaxies. Dashed (solid) lines represents data from observation (derived results from the simulation data). Green represents circularized half light radius for filter r with a 30 kpc cut-off. Green, black and blue dashed lines shows data from Van14 et al. [213], Sloan Digital SkyServer Data Release 7 [120], and DASH [128] respectively.

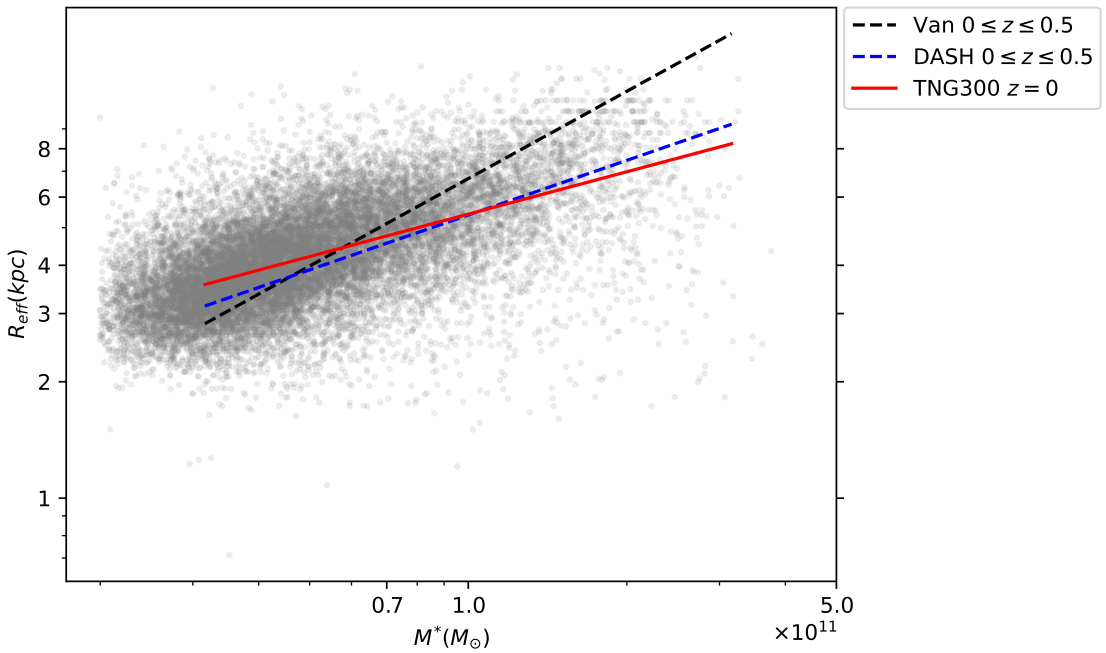

Figure 2.9: Effective radius ($R_{\rm eff}$)- stellar mass (M_*) relation at $z = 0$ for Early-type galaxies. Dashed (solid) lines represents best power law fit for data from observations (TNG300 simulation). Blue and black dashed lines shows results from van der Wel et al. [213] and DASH [128] respectively. Red line is a minimum chi squared fit created using Scipy regression package [217] in Python. The fit is done for halos with $M_* \geq 3 \times 10^{10} M_\odot$. M_* is the stellar mass within 30 kpc radius from the galactic center.

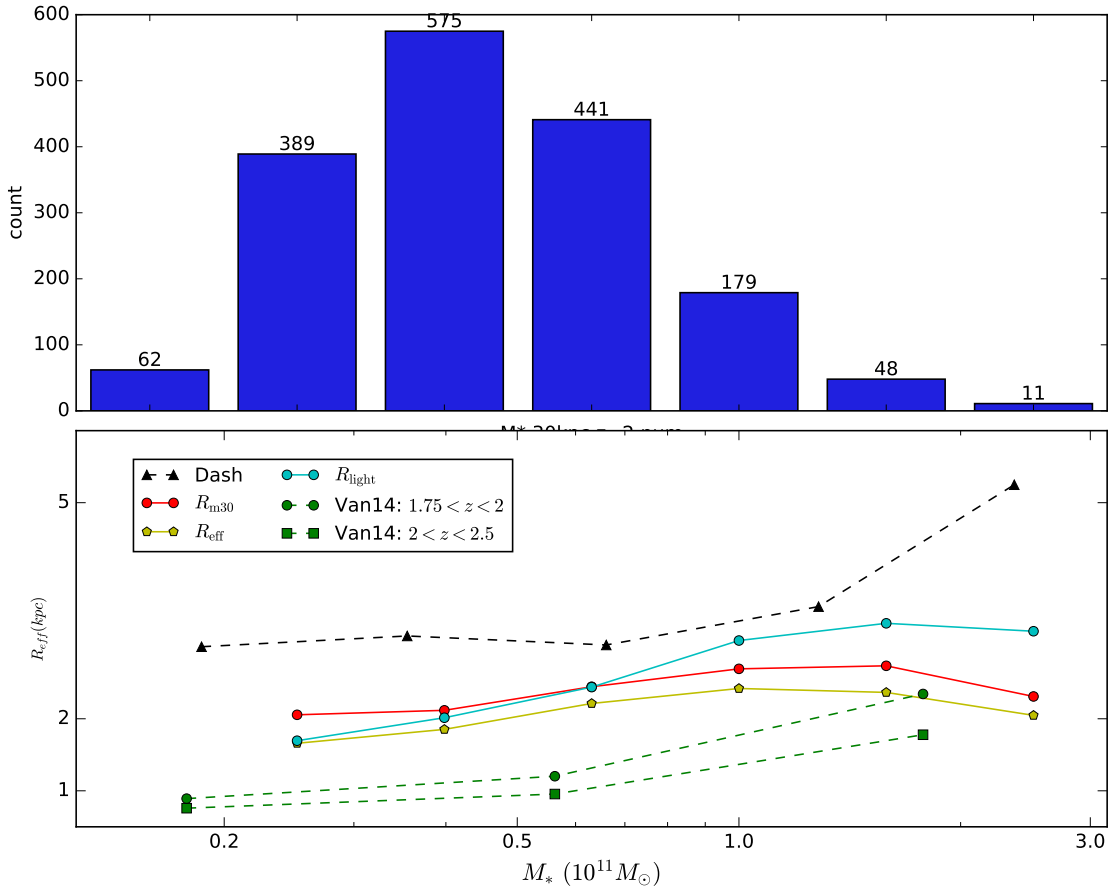

Figure 2.10: Median size-mass relation at $z = 2$ for Early-type galaxies. Green represents circularized half light radius for filter r with a 30 kpc cut-off. Black line shows half-light semi-major axis derived from the galaxy profiles [120] analyzed for Sloan Digital SkyServer Data Release 7.

Effect of Dust Correction

We use the dust model discussed in Section 2.2.4 to implement the attenuation of stellar light by dust. We explore how important the dust effect is and quantify its effect on galaxy sizes. In Figure 2.11 we plot the median half-light radius for stellar luminosities with and without dust correction. Both radii were inferred using elliptical isophotes centered at the light center in x-y plane. Both calculations only include stellar particles within 30 kpc from the light center. In Figure 2.12 we show the distribution of the ratio ($\frac{R_{\rm dust}}{R_{\rm raw}}$); dust-corrected half-light radius to without dust-correction half-light radius.

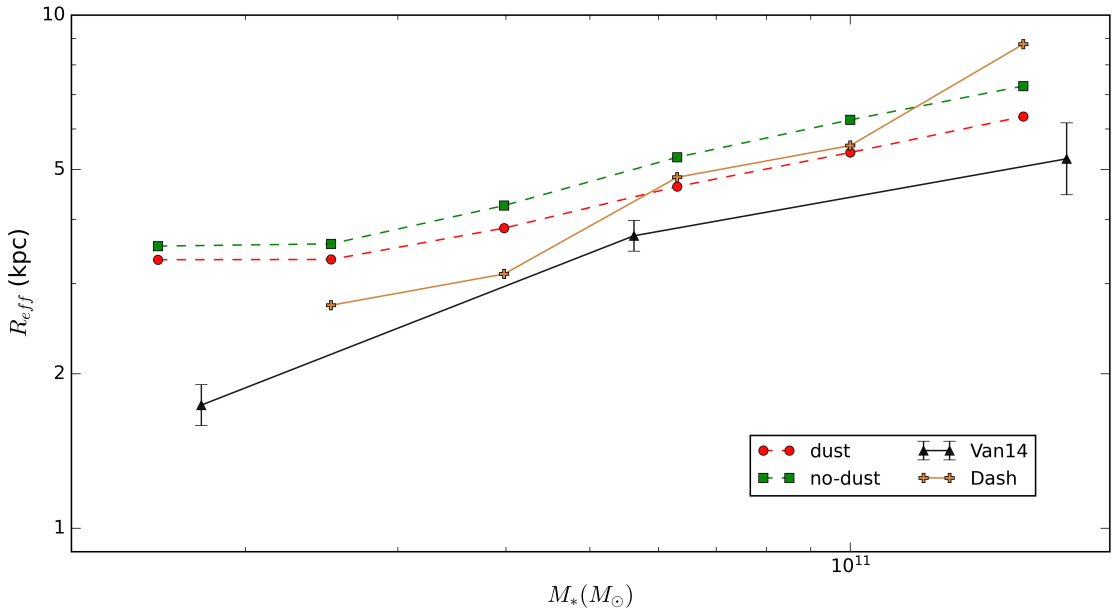

Figure 2.11: Comparison of dust corrected vs raw median mass-size relations at $z = 0$ for Early-type galaxies. red (green) points show half-light radii with (without) dust correction. Black line and brown line show median half-light semi-major axis from Van14 [120] and DASH [128] respectively.

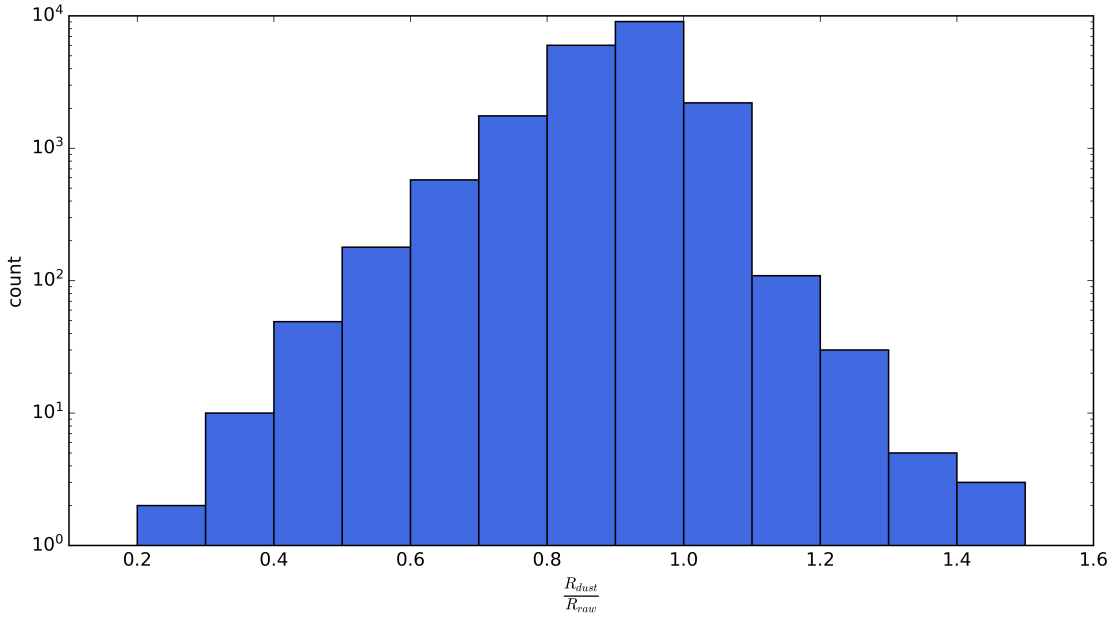

Figure 2.12: Distribution of dust corrected ($R_{\rm dust}$) to raw ($R_{\rm raw}$) half-light radius ratio at $z = 0$ for Early-type galaxies. The blue solid histogram indicates the number distribution of the ratio for 0.1 size bin.

Wave Length Dependence

Figure 2.13 shows the median size for 3 different filters compared to observations at redshift 2. The yellow, blue, and red lines represent median half-light radii for the filters; Buser's V, Buser's K, and SDSS camera g filter, respectively. Half-light radii were calculated using raw stellar luminosites of stellar particles within 30 kpc from the galactic center. The green and black dashed lines show results from van der Wel et al. [213] for wavelength 5000Å and DASH [128] for H_{160} filter, respectively.

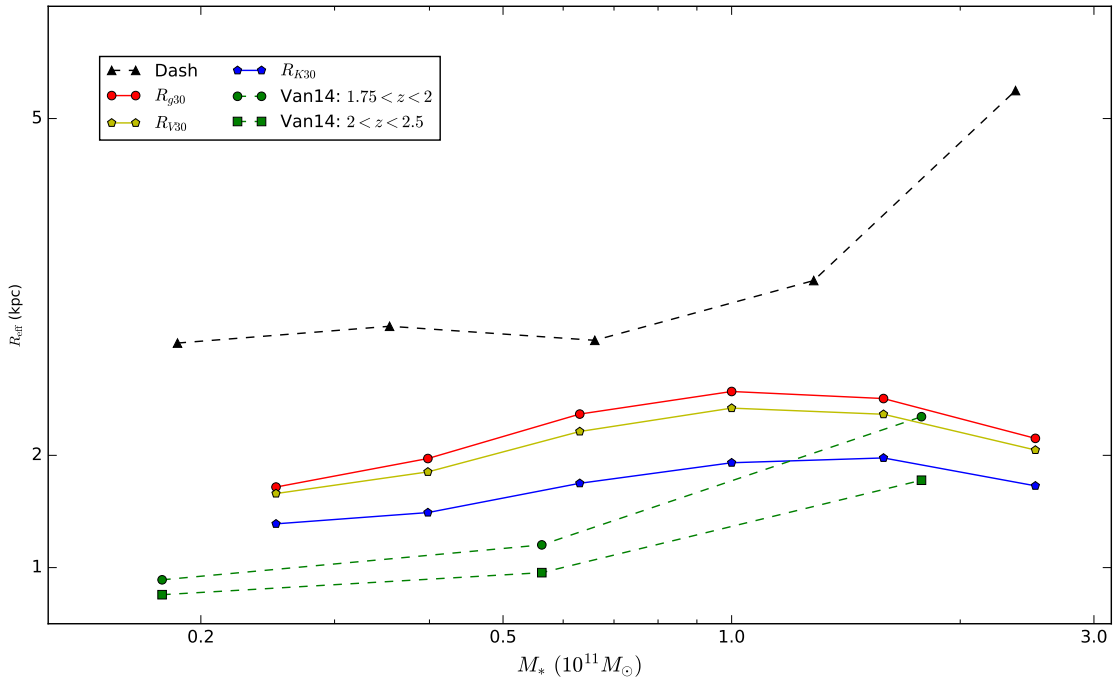

Figure 2.13: Median half-light radii for filters Buser's V, Buser's K, and SDSS camera g filter at redshift $z = 2$. Half-light radii were calculated using raw stellar luminosites of stellar particles within 30 kpc from the galactic center. Green and black dashed lines shows results from van der Wel et al. [213] for wavelength 5000 Å and DASH [128] for H_{160} filter respectively.

Aperture Dependence

Figure 2.14 shows how a cutoff from the galactic center affects galaxy sizes. Dashed (solid) lines represent data from observations (derived results from the simulation data). The teal, yellow, and red lines represent the median half-mass radii for apertures 100 kpc, 50 kpc, and 30 kpc from the galactic center, respectively. The stellar mass (M^*) is also defined as the stellar mass within a radius according to the corresponding aperture from the galactic center. Green represents the circularized half-light radius for filter r with a 30 kpc cutoff. Green, black and blue dashed lines show data from van der Wel et al. [213], Sloan Digital SkyServer Data Release 7 [120], and DASH [128] respectively.

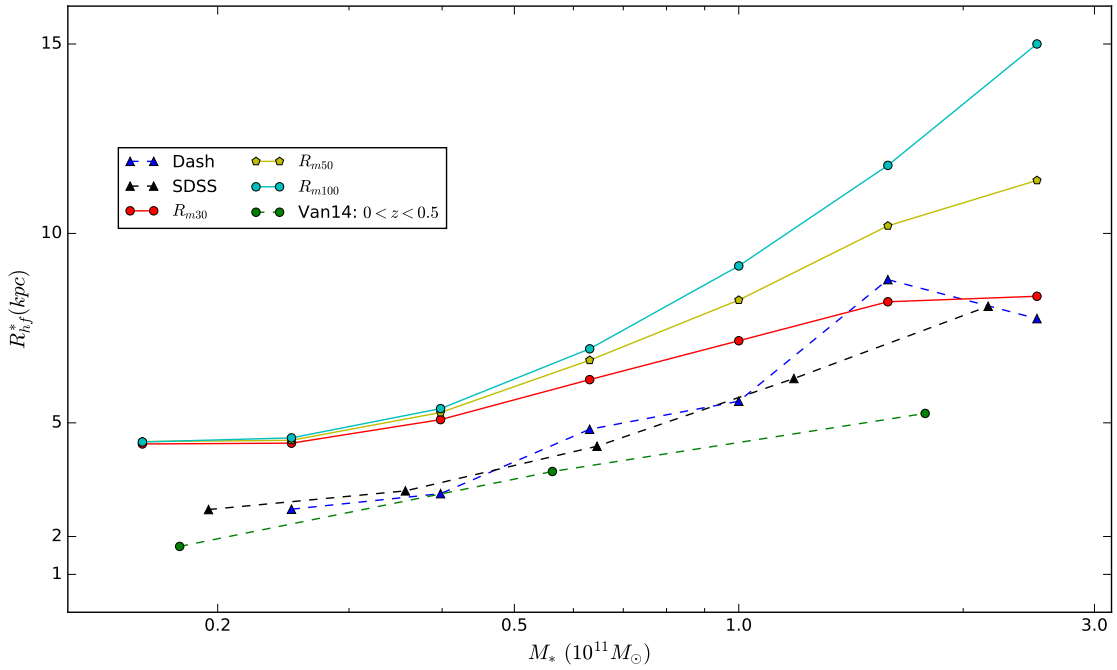

Figure 2.14: Median stellar half-mass radius at $z = 0$ for different apertures from the galactic center. Dashed (solid) lines represents data from observations (derived results from the simulation data). The teal, yellow, and red lines represent the median half-mass radii for apertures 100 kpc, 50 kpc and 30 kpc from the galactic center, respectively. The stellar mass (M_*) is also defined as the stellar mass within a radius according to the corresponding aperture from the galactic center. Green represents the circularized half-light radius for filter r with a 30 kpc cutoff. Green, black and blue dashed lines show data from van der Wel et al. [213], Sloan Digital SkyServer Data Release 7 [120], and DASH [128] respectively.

2.3 Discussion

This section demonstrates that ETGs grow in size from $z = 2$ to $z = 0$ for TNG300. This has not been done robustly for TNG300 before, only using half-stellar mass radii [167]. In Figure 2.8, we show that half-stellar mass ($R_{\rm m30}$), half-light radius for raw stellar luminosities and including all the stellar particles ($R_{\rm light}$) overestimate the sizes compared to the effective radius ($R_{\rm eff}$) which includes dust-corrected luminosities and 30 kpc cut-off from the galactic center. Compared to observations, $R_{\rm eff}$ performs better than the other estimators, which have the closest deviation from both Van14 [213] and DASH [128]. Although the two observations agree well for lower stellar mass, they show a larger deviation at massive mass bins. This discrepancy in the observation is even seen at redshift 2 (Figure 2.10). This could be mainly due to the difference in samples, since Van14 [213] has fewer galaxies (a factor of 3-4 less) for $M_* \geq 10^{11} M_\odot$ compared to DASH [128].

As expected from the median size results, Figure 2.9 shows that our calculated $R_{\rm eff}$ for ETGs in TNG300 agree well with DASH [128] but deviates more from van der Wel et al. [213] especially at higher stellar masses. This could be due to bias in the sample and the different statistical procedures implemented in those studies. Also, the impact on the mass evolution and soft length needed to be studied, as there could be an impact on the results.

Figure 2.11 shows that dust-corrected half-light radii are more consistent with the observations. The difference between with dust correction and without dust correction median radii is smaller at lower stellar mass end and higher for larger stellar mass bins. This is possibly due to the fact that massive ETGs have more gas, whereas a significant number of less massive ETGs do not posses gas; i.e., larger portion of massive ETGs show a higher dust attenuation compared to ETGs in lower stellar mass bins. Figure 2.12 illustrates the importance of dust correction. Although the median of the ratio ($R_{\rm dust}/R_{raw}$) is closer to one (0.9), approximately 10% of the ETGs at $z = 0$ show at least 25% effect by dust correction.

The median effective radii of ETGs decrease with wavelength according to the figure2.13. Filter g has the smallest wavelength while K has the highest wavelength out of those 3 filters. Hence, when filter g shows the largest half-radius and filter K the smallest, our results follow the trend expected by Barbera et al. [95, 213]. van der Wel et al. [213] measured a redshift and stellar mass-dependent negative slope for $\log(R_{\rm eff}) - \log(\lambda)$ which implies that the longer the wavelength, the smaller the measured galaxy size.

Our simulation results show (Figure 2.14) the importance of having a radial cut. Since simulations grasp all the particles which are identified by the Subfind algorithm, which can be extended to several hundreds of kpc, light curves in observations are not sensitive to that kind of radius. Hence, subhalos in simulations capture ICL which overestimate the galaxy size and stellar mass. We show that 30 kpc cut-off is the best estimator out of 100 kpc, 50 kpc cut-offs, which agrees with the observations. This discrepancy between $R_{\rm m30}$ and other half-stellar mass radii is not clearly visible for lower mass bins but is clearly visible for mass bins above $10^{11} M_{\odot}$.

2.4 Conclusion

We explored how to bridge simulation halo properties with observations. We found that the best estimator (closest to Van14) for stellar mass is M^{*}_{30} which imposes a 30 kpc radial cut-off from the halo light center. The best size estimator is the dust corrected half-light radius ($R_{\rm eff}$) where we used 30 kpc cut-off and elliptical isophotes to derive. The half-stellar mass radius overestimates the galaxy size at both redshifts $z = 0$ and $z = 2$.

By deriving half-light radii and stellar mass for TNG300-1 hydrodynamic simulation, we derive the median galaxy size-stellar mass relationship for redshift $z = 0$ (Figure 2.8) and $z = 2$ (Figure 2.10). At both $z = 2$ and $z = 0$, the median size for a stellar mass bin

increases with the stellar mass, as expected. The median sizes for a given mass bin increase from $z = 2$ to $z = 0$. This shows that the increase in galaxy size-mass relationship is not due to the prognitor bias but to the physical growth in galaxies. Dust correction plays a vital role in estimating reliable half-light radii. Although for less massive ETGs, the median of the dust corrected R_{50} is only around 5% lower than the raw R_{50}, massive ETGs show a difference over 15% between two types of radii.

Using raw stellar magnitudes for three different filter bands (g, V, K), we show that the halo stellar structure depends on the wavelength. We find that half-light radius has a negative correlation with the wavelength. We show that massive ETGs stellar mass profile extend beyond 100 kpc from the center, hence capturing possibly ICL. The discrepancy between half-stellar mass radii $R_{\rm hm100}$ and $R_{\rm hm30}$ increases with stellar mass.

In summary, we derive the stellar mass-size relationship for ETGs in the simulation TNG300. We explore the factors that are sensitive to the mass-size relationship and compare them with what is observed in the literature. Our best estimated median mass-size relationship agrees well with the trend expected from the observed data. This gives us the opportunity to look for relics candidates using the mass-size relationship in the next chapters.

2.4.1 Future Prospects

One potential effect that we did not consider that might affect the results is "halo-subhalo switching". Halo-Subhalo switching occurs when a massive halo/subhalo comes closer to the halo/subhalo of interest. As we discussed previously, the primary subhalo is the most massive subhalo in a halo, but when a more massive subhalo comes closer to the first subhalo, the Subfind algorithm may identify the new subhalo as the primary subhalo. In this process, the change of identification may cause the coordinates to change even by 1000 kpc. Overall, this should not greatly change the statistics. For more details, see the Appendix A.

Another path that needed to be explored was including satellite subhalos to the sample. As we mentioned before, to avoid chaotic effects (to some extent), such as tidal stripping, we chose only primary subhalos. Including the secondary subhalos will significantly increase the sample size, but it may introduce bias effects from having more tidally affected subhalos (Rodriguez et al. [167] showed that satellites in TNG300 are roughly 30% smaller than the primary subhalos due to mainly tidal stripping).

Apart from exploring different samples, there is more to investigate on inferred sizes of ETGs. We have only employed a nonparamtric method to infer sizes, but Sersic fitting is feasible for TNG300 data. To our knowledge, no one has so far studied how the multi-component Sersic fits would affect the mass-size relation in hydrodynamical simulations. For example, although ETGs are less structured compared to spiral galaxies, Huang et al. [77] proposed that local ellipticals generally contain three structural components; therefore, the majority of ellipticals are not well described by a single-component Sersic fit but by a three-component Sersic fit. Other work including Meert et al. [119] and Msoleh et al. [127] supports for multi-component Sersic fit over single-component. In fact, Msoleh et al. [127] showed for ETGs nonparametric and two-component Sersic fits yield the most robust estimations of effective radius, while single Sersic fits often overestimate the effective radius. We can try to find and answer "is there a better suited radius to investigate the formation of ETGs?".

I hope that I would have the opportunity to investigate these issues/find answers, not just in TNG300, but also in upcoming simulations (e.g., MilleniumTNG[1]) in the future.

[1]The successor of IllustrisTNG which is almost 15 times larger than TNG300.

Chapter 3

Physically Defined Massive Relic Galaxies in TNG300 Simulation

3.1 Introduction

As we mentioned in Chapter 1, massive galaxies go through a two-phase evolution where the latter phase is dominated by minor dry mergers. Because of its stochastic nature, some of these galaxies do not go through a merger between $z \sim 2$ and $z = 0$; called relics. With the development of simulations and availability of their merger trees, it is possible to define relic galaxies physically. Using this opportunity, we briefly review the previous work done on defining relics physically, and then describe how we develop criteria to define relic galaxies physically in the hydrodynamical simulation TNG300. Then we examine whether they produce the key stellar properties expected of massive relic galaxies, and finally analyze how relicness is correlated with dark matter properties.

3.1.1 Approach from Observations

In the observational approach, a relic galaxy is usually defined on the basis of compactness (see Chapter 4). Using extreme compactness as a classifier, studies are able to select the galaxies at the extreme end of the relicness. Imposing extreme compactness criteria (i.e., $R_{\rm eff} \lesssim 2\,{\rm kpc}$) may lose some of the relic candidates not just due to capturing the extreme end of the relicness spectrum, but also some massive relics in general might have larger radii depending on some other factor (e.g., environment). There exists substantial evidence indicating that there could be two possible evolutionary paths from red nuggets to relics [12]; i.e., relics residing in dense or isolated environments, displaying different average effective radii from each other. However, since the massive relics galaxies are expected to avoid the second phase of the galaxy formation, it is expected to have a size (i.e., effective radius) similar to the size predicted from $M_* - R_{\rm eff}$ at $z = 2$.

3.1.2 Utilizing Simulations

The halos in N-body simulations grow hierarchically bottom-up, starting from smaller halos and later making clusters. In this picture, halos/subhalos grow mainly either internally (i.e., formation of in-situ stars) or via mergers. With the development of larger N-body simulations and later improving their mass and time resolutions, the need for tracking of halo's growth and assembly history was created. A set of semi-analytical models was introduced to dictate the set of conditions that determines how the subhalos grow with the snapshots. For each subhalo, the semi-analytical model produces a tree structure, starting with the trunk at an early snapshot and then branching out with time [96]. The initial development was centered around Monte Carlo merging trees, drawing from the foundation of the extended Press-Schechter formalism [97]. These types of merger trees do not produce a mass function for halos, which is well in agreement with the mass function taken directly from N-body

simulations [11]. Furthermore, these trees did not predict the expected merger rates [182].

Later, with the development of higher resolution N-body simulations, more accurate merger trees were built directly from the simulations. Modern hydrodynamical simulations have merger trees built at the subhalo level. There are several different merger tree algorithms being used, and they use different particle types and merit functions to identify progenitors and descendants [191]. In our TNG300 simulation, the merger trees are built using Sublink [168]. In general, the predictions by the merger trees in TNG300 agree well with the observations. For example, galaxy–galaxy merger rate and its redshift dependence for halos with $M_* \gtrsim 10^{10} M_\odot$. But for descendant massive galaxies with $M_* \gtrsim 10^{10} M_\odot$, galaxy-galaxy merger rate becomes steeper with the redshift, while observational studies [141, 113] show approximately a constant or decreasing evolution.

With the availability of merger trees, hydrodynamical simulations provide the opportunity to track the mass-assemble history of a halo. This allows us to use dark-matter and stellar properties as a constraint to filter out mergers and other external interactions with the halo. There is only a handful of work [154, 60] on finding relics in simulations. de Arriba et al. [154] analyzed the old Millenium simulation and used only two conditions; i.e., 1) the halo must be formed by $z \sim 2$, 2) the stellar mass at $z \sim 2$ is greater than 90% of the stellar mass at $z = 0$. They identified a halo is formed by $z \sim 2$, if the halo is identified by the halo finder algorithm at $z \sim 2$. This seems to be a very relaxed criterion for quantifying the formation time, despite that the point at which a halo can be definitively considered to have formed lacks a definition that is consensus among all [101]. The most widely accepted definition of formation time is the point at which the main branch of the halo has accumulated half of its mass at $z = 0$ [96, 99]. However, this definition can lead to significantly different formation times [200].

The other work exploring relics in N-body simulations has been done by Flores-Freitas et al. [60]. They used compactness criteria motivated by observations not solely based on the

history of halo mass assembly. They identified 5 candidates for relic galaxies, but 3 of them show central-satellite switching [9] close to $z \sim 0$, which occurs when a more massive halo/subhalo gets closer to the selected subhalo. This may affect the outer regions of the selected subhalo, hence may not be truly a relic; i.e., tidal effects at outer regions of the halo.

There is a clear requirement for further in-depth research on relic galaxies in N-body simulations, as there are only a few studies on this topic in simulations and none in modern large simulations. Additionally, there are questions about the physical definition of relic galaxies that have not been well explored. What are the ingredients for the definition of relicness? How relicness correlates with dark matter properties (especially dark mater concentration: c_{200}).

3.2 Simulating ETGs with TNG300

We use publicly available raw data for the hydrodynamical cosmological simulation TNG300-1 [139] (which is referred to here as TNG300). It uses the quasi-Lagrangian code AREPO [187] to solve coupled dynamical equations of dark matter and gas. They start from the initial conditions for the universe from Planck 2015 observations [158].

The galaxy formation model of this simulation includes magnetohydrodynamics, isotropic galactic winds improved from older simulations, and modified black hole driven kinetic feedback [157]. It assumes a Chabrier initial mass function [26, 218] for the stellar evolution model. The star formation column density (n_H) threshold for gas to form stars is $\sim 0.1\,\mathrm{cm}^{-3}$ and pressurization of the multiphase ISM is treated as in Springel & Hernquist model [188]. The merger trees are built using SubLink [9] and Lhalo algorithms [189].

The simulation physics runs in a periodic cube of 304 cMpc and a total of 100 snapshots

spanning redshifts $z = 20$ to $z = 0$ are available publicly. Publicly available raw data has 4 particle types: gas, dark matter, stellar and wind, and black holes. For the gravitational interaction between themselves and others, there is a softening length imposed. For DM, stellar and wind particles are fixed at a comoving value of 1.48 ckpc until $z = 1$ and after that 1.48 kpc value up to $z = 0$. The gas particles have an adaptive gravitational softening ($\epsilon_{\rm gas} = 2.5\, r_{\rm cell}$), where $r_{\rm cell}$ is the radius calculated assuming the Voronoi gas cell is a sphere. Mass resolution is set to $1.1 \times 10^7\ M_\odot$ for baryons and $1.1 \times 10^7\ M_\odot$ for dark matter.

3.2.1 Halo selection

All selected subhalos are identified by the SUBFIND algorithm, and the data are publicly available. Motivated by the relic galaxy Mrk 1216 which is a massive compact galaxy ($M_{200} \geq 10^{12} M_\odot$), we choose M_{200} accordingly for the selection at $z = 0$. Although, in the two-phase galaxy formation picture, it is not precisely defined at which redshift the second phase started dominating the first phase (around $z \sim 1.5 - 2$), we choose only $z = 2$ (we explore other redshifts for halo formation time. see the APPENDIX B). We used the LHalo merger tree to find the progenitor (at $z = 2$) of the subhalos at $z = 0$. Summarizes the selection criteria is

- $10^{12} M_\odot \leq M_{200} \leq 5 \times 10^{11} M_\odot$.
- Primary subhalo at $z = 0$ and z = z_i for $i = 1, 2$ where $z_i = 1.5, 2$.
- Subhalo flag = 1.
- ETG at $z = 0$ (based on the definition using sSFR. see Section 2.2.3).

The subhalo flag indicates whether the subhalo has a cosmological origin or not. Not all objects recognized by the SUBFIND could be considered as galaxies. Some subhalos may

not have collapsed as a result of the structure formation process. The subhalo flag = 1 indicates that the subhalo structure has collapsed from the galaxy formation model and has enough baryonic mass.

3.2.2 Method to compute Stellar properties

We use the calculated stellar mass (M_*) as we explained in Chapter 2.1.1, where we imposed a cutoff of 30 kpc from the subhalo center (coordinates of the particle with the least potential identified by SUBFIND). Similarly, we use the same projected half-light radii with dust correction and 30 kpc cut-off from the light center in x-y plane (see Chapter 2.2.5).

To estimate the age of the stellar population of a subhalo, we use the median of mass-weighted stellar age. We use spherical radial bins measured from the subhalo center. Radial bins are evenly spaced from $0.05\,\mathrm{kpc} - 30\,\mathrm{kpc}$ with a bin size of $0.2\,\mathrm{kpc}$. We use publicly available "stellar formation time"[1] to find the scale factor when the stellar cell was born. Then we use the astropy package [4, 3, 2] to calculate the look-back time for each stellar particle in the radial bins under the assumption of Planck 2015 ΛCDM cosmology.

3.2.3 Method to Compute Dark Matter Properties

We employ two distinct methods to define dark matter mass within an aperture around the subhalo center; arbitrary proper length scale and aperture based on a spherical overdensity. Each method is applied at two different redshifts; i.e., redshift 0 and 2. The first method uses a fixed radius (R) as an aperture. In this method, we define the dark matter mass of the halo as the total mass of dark matter particles within R from the subhalo center (assigned by the SUBFIND algorithm). The chosen values for radius (R) are: {30 kpc, 50 kpc, 100 kpc,

[1] `https://www.tng-project.org/data/downloads/TNG300-1/`

120 kpc, 150 kpc, 200 kpc }.

The other method we employed to define dark matter mass of the halo is using a radius based on spherical overdensity which is the standard way to define the boundary of a halo. Such a radius is defined as the radius that encloses a sphere having a chosen average dark matter density. We selected a range of different values for the average density (ρ_{avg}) which is a factor of the critical density (ρ_c) of the universe at each redshift (i.e., $z = 2$ and 0); i.e., $\rho_{\rm avg}/\rho_c = \{$ 200, 500, 2500 $\}$. We use the astropy (a Python package) to calculate ρ_c for Planck 2015 ΛCDM cosmology. This way of defining the halo mass is commonly used in astrophysics, while each factor of ρ_c (i.e., 200, 500, 2500) is more or less sensitive to different physical processes (e.g., larger radii are more sensitive to tidal effects while smaller radii are not).

Next, we compute dark matter concentrations assuming halos follow Navarro-Frenk-White (NFW) profile (for more details see Chapter 5.1). The radial profile of the spherically averaged density ($\rho(r)$) is given by ,

$$\rho(r) = \frac{\delta \rho_c}{(r/r_s)(1 + r/r_s)^2} \tag{3.1}$$

where δ is an arbitrary number[2], r_s is called the scale radius which is assigned to the radius where the logarithmic slope of the density becomes -2. First, we computed c_{200} for all halos within that mass range. All halos dark matter profiles are fitted for the NFW profile. To calculate c_{200} we use the following algorithm, which we adopted from Chen et al. [27].

1. Take equally space radial 20 bins in log space from the halo center to r_{200}

2. for an assumed c_{200}, using the equation calculate expected M_{200} for a NFW profile for

[2]for c_{200} calculation, $\delta = 200$

radial bin "i', ($M_i^{\rm NFW}$)

3. Find the c_{200} minimizing the χ^2 given by,

$$\chi^2(c) = \sum_{i=1}^{20} \frac{[M_i - M_i^{\rm NFW}]^2}{M_i^2/N_i} \tag{3.2}$$

where M_i and N_i are the total dark matter mass from the particle data and the number of dark matter particles in the radial bin 'i' respectively.

$$M(< r) = M_{200} \frac{f(cr/r_{200})}{f(c)} \tag{3.3}$$

where $f(c) = \ln(1+c) - \frac{c}{1+c}$

The χ^2 function includes the number of particles in each bin in order to avoid bias towards mass bins with low particle number resolutions; i.e., in general, the number of particles becomes less for larger log-mass bins, therefore the contribution from such bins becomes less. Our c_{200}-M_{200} relation is in good agreement with other work in the literature. (see Section 5.2)

3.3 Defining Relicness - Standard Method

In this section, we first define the relicness based on dark matter and stellar mass change since $z = 2$, adopting a 100 kpc fixed aperture to define dark matter mass ($M_{\rm dm100}$). As we have discussed in Section 3.2.3, there are numerous ways to define dark matter mass, but we choose a 100 kpc aperture for three main reasons. First, since we adopt a fixed aperture 30 kpc to define stellar mass, it is motivated to select a fixed aperture to define dark matter

mass. Second, since very large radii (e.g., similar to virial radius) are are heavily affected by mergers/flybys, therefore, a mid-range radius has a balanced effect. Third, dark matter mass within an aperture based on overdensity follows a pseudo-evolution since the critical density of the universe decreases with time (i.e., in the ΛCDM model, ρ_c at $z = 2$ is roughly 9 times of ρ_c at $z = 0$) in contrast to mass within a fixed radius does not have such evolution. We explore the best estimators to constrain dark matter and stellar mass evolution. Then we look for the best estimator to capture the lack of dark matter evolution in relics since z_f.

3.3.1 Definition

The definition we use in this section is primarily motivated by the previous work by Arriba et al. [153] two-phase galaxy formation paradigm for massive ETGs. We add an extra criteria; i.e., constraining evolution of the DM mass after $z = 2$, since phase 2 stellar accretion should be accompanied by DM accretion, since typically galaxies reside inside DM halos. The criteria we used to define massive relic galaxies are as follows.

1. $M_* \geq 10^{11} M_\odot$ at $z = 0$.
2. M_* at $z = 2$ is at least 90% of M_* at $z = 0$.
3. $M_{\rm dm100}$ at $z = 2$ is at least 90% of $M_{\rm dm100}$ at $z = 0$.

The selection of 90% as the limit for both stellar and dark matter mass evolution is somewhat arbitrary. We first select 90% as used by Arriba et al. [153], but in Section 3.3.3 we explore how properties of relic galaxies depend on the fraction of mass that was used to constrain.

The stellar mass and effective radii for the sample are displayed in Figure 3.1. Both the stellar mass and the effective radii were inferred using a 30 kpc radial cut as described in Section 2.2.5. To demonstrate how relic galaxies are compact compared to non-relics, we

have added the medians of the two samples (i.e., relics and non-relics) in the plot. As shown in Figure 3.1, relics are roughly 1.7 times more compact than the non-relics. There are only a few ultracompact relic galaxies (a number of 12), and some of the relics show a higher $R_{\rm eff}$.

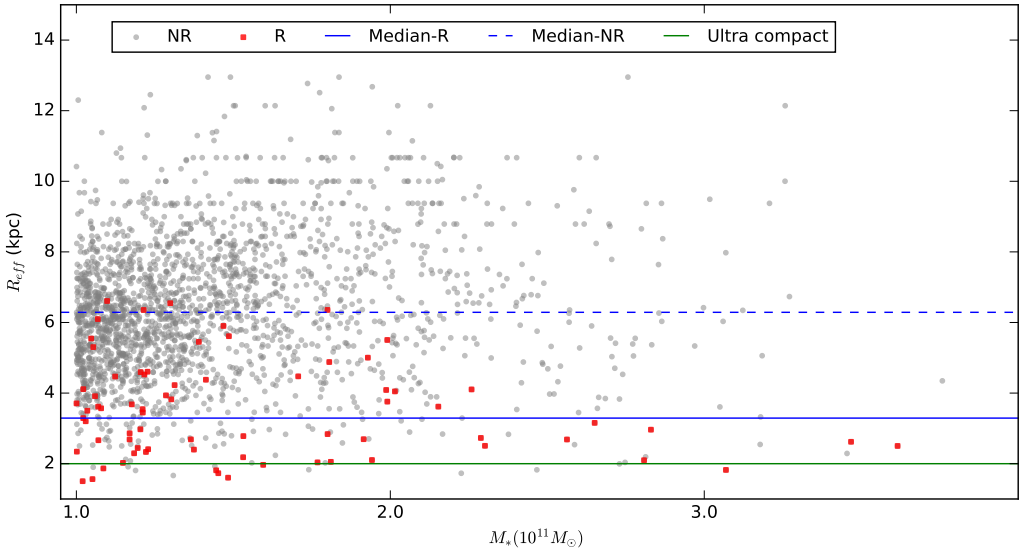

Figure 3.1: Effective radius ($R_{\rm eff}$) and stellar mass (M_*) for ETGs with $M_* \geq 10^{11} M_\odot$ at $z = 0$. Each red and grey dot represents relics and non-relics respectively. Solid blue and dotted blue lines represent the median effective radius of the relics and non relics sample respectively. The green line shows the constraint widely used in the studies [201, 17] to define ultra-compact massive galaxies.

In Figure 3.2 and Figure 3.3, we show stellar mass vs median stellar age and specific star formation rate (sSFR) respectively. As expected from the two-phase galaxy formation paradigm, the relics have an older stellar population. Notice that in Figure 3.3, it depicts that the majority of the relics almost do not have star-forming activities within a 30 kpc radius in the last 1 billion years. The specific star formation rates are adopted from Donnari et al. [51] which has only considered stellar particles within 30 kpc of the subhalo center for the calculation.

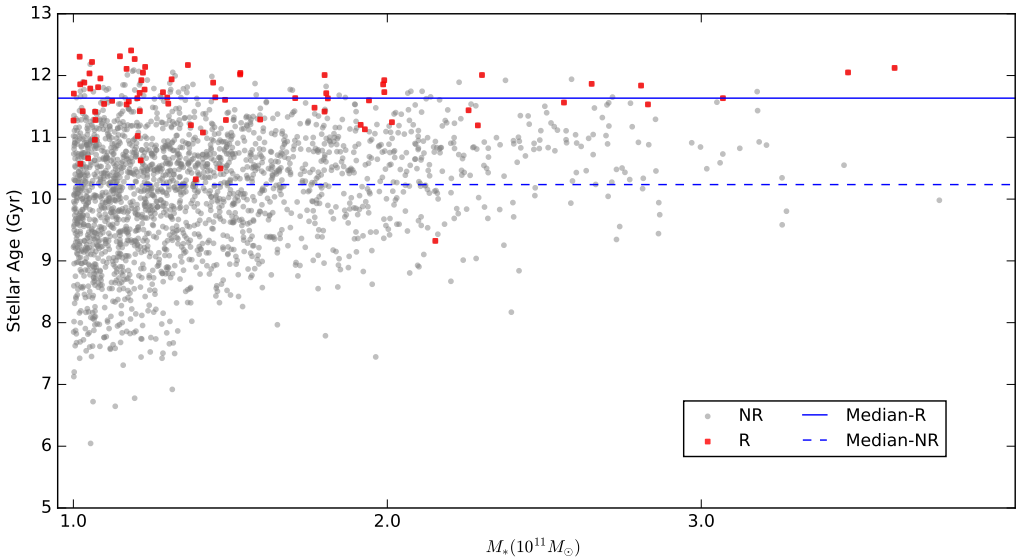

Figure 3.2: Median stellar Age and stellar mass (M_*) for ETGs with $M_* \geq 10^{11}M_\odot$ at $z = 0$. Each red and grey dot represents relic and nonrelic galaxy respectively. Solid blue and dotted blue lines represent the median effective radius of the relics and non relics sample respectively.

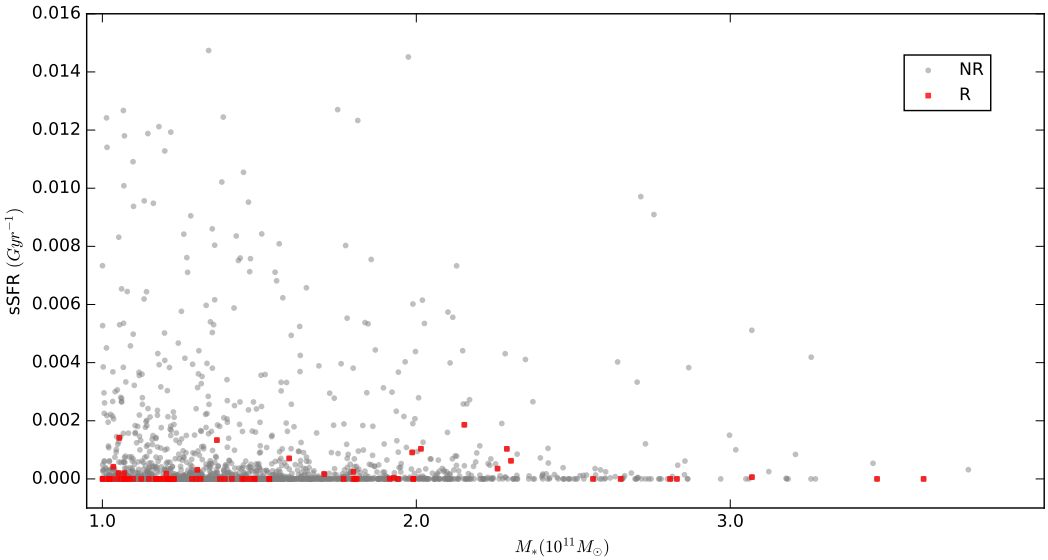

Figure 3.3: Specific star formation rate (sSFR) and stellar mass (M_*) for ETGs with $M_* \geq 10^{11} M_\odot$ at $z = 0$. Each red and grey dot represents relic and nonrelic galaxy respectively. The blue line shows the median of sSFR for the relics.

3.3.2 Varying Dark Matter and Stellar Mass Constraints

The compactness of the selected relic sample is correlated with the physically defined relicness as shown in Figure 3.4. In Figure 3.4, we plot the median effective radius of the relic sample for each value that constrains the dark matter change and the stellar mass change (hereafter "M_* passiveness") after $z = 2$. Each color represents a different fractional value for the constraint that limits stellar mass evolution. For example, the relic sample shown by blue dots only has galaxies with at least 95% of the stellar mass of $z = 0$, has assembled by $z = 2$. As illustrated in the figure, the larger the M_* passiveness, the more compact it becomes. Another important characteristic that the figure shows is how dark matter and stellar mass evolution are correlated. It shows that the higher the M_* passiveness, the more $M_{\rm dm}$ passiveness becomes (see Figure 3.6).

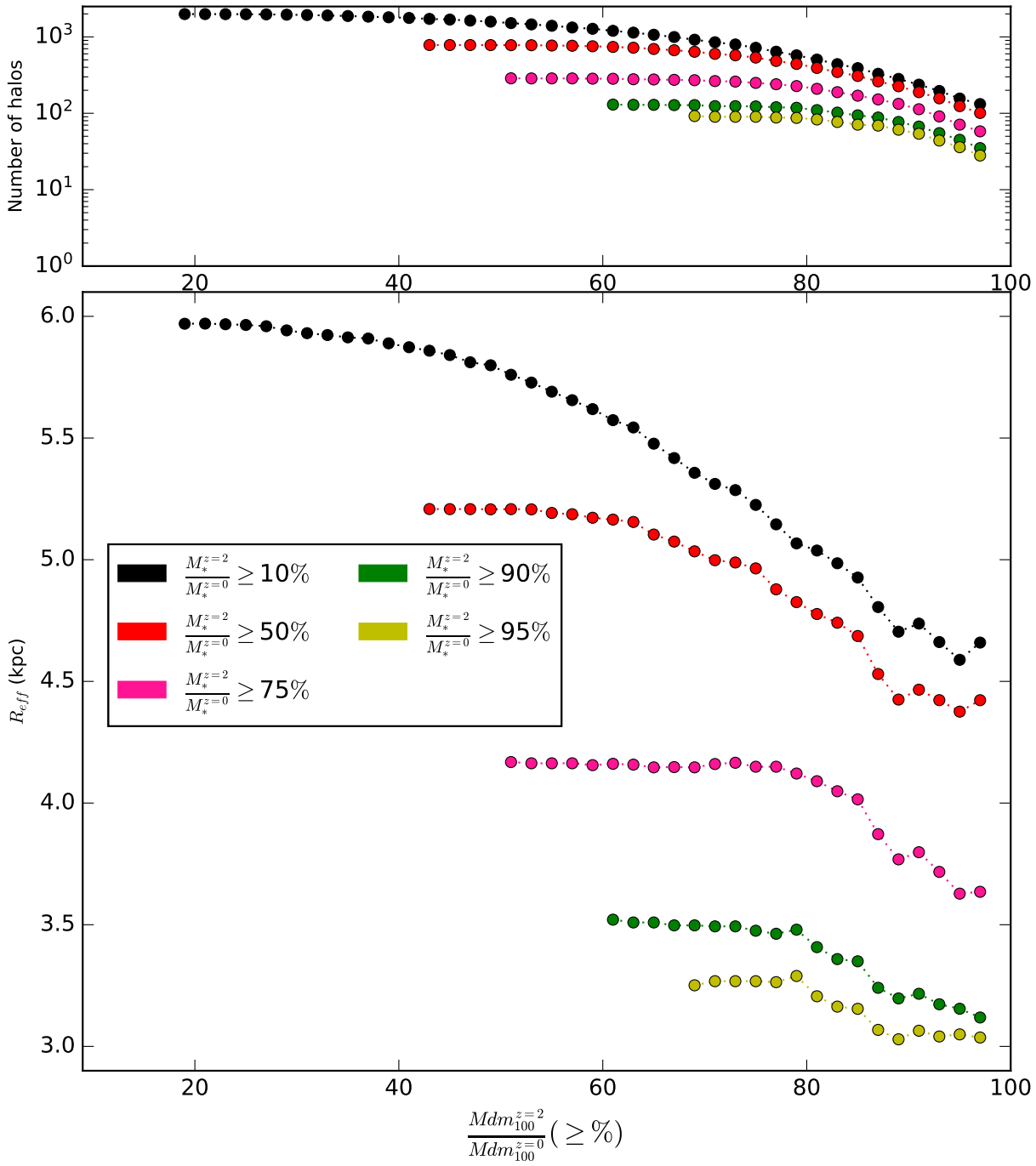

Figure 3.4: (Bottom panel) Median effective radius ($R_{\rm eff}$) of the relics for each relic criteria. Each dot represents the median $R_{\rm eff}$ of the sample which is consistent of ETGs selected by imposing constraints on dark matter and stellar mass evolution since $z = 2$. Different colors corresponds to different constraints on stellar mass evolution and for each sample of relics, the minimum stellar mass ratio $M_*^{z=2}/M_*^{z=0}$ is mentioned in the legend. (Top panel) number of ETGs in each relic sample.

3.3.3 Dark Matter and Stellar Mass Coupling

In the ΛCDM model, dark matter interacts with matter (i.e., gas and stellar particles in TNG300) via gravity; therefore, it is expected that dark matter profile is correlated with stellar mass profile. In Figure 3.5, we plot the fractions of dark matter mass and stellar mass at $z = 2$ with respect to their corresponding mass at $z = 0$. It shows a large positive correlation between the dark matter and the stellar mass as predicted form the theory, although there is considerable scatter. Interestingly, there are some ETGs that lose either stellar mass or dark matter mass or both after the redshift $z = 2$.

The statistics (median, quartiles and quartile range) of the fraction of dark matter evolution for each constraint in the fraction of stellar mass evolution are plotted in Figure 3.6. These statistics demonstrate that stellar mass and dark matter mass are affected similarly in the evolution of massive compact galaxies. Also it shows that the scatter in fraction of dark matter evolution decreases as the constraint for the stellar mass evolution becomes heavier.

As we notice that there are relics that demonstrates mass loss between $0 < z < 2$ (i.e., mass loss is reflected by stellar and dm fractions of evolution > 1) in both Figure 3.5 and Figure 3.6, we wanted to investigate the impact on the statistics of these relics with mass loss. Do they lose the mass due to a physical process (merger or tidal stripping) or is it just due to a numerical issue (misidentification of particles identified by the halo finder)?

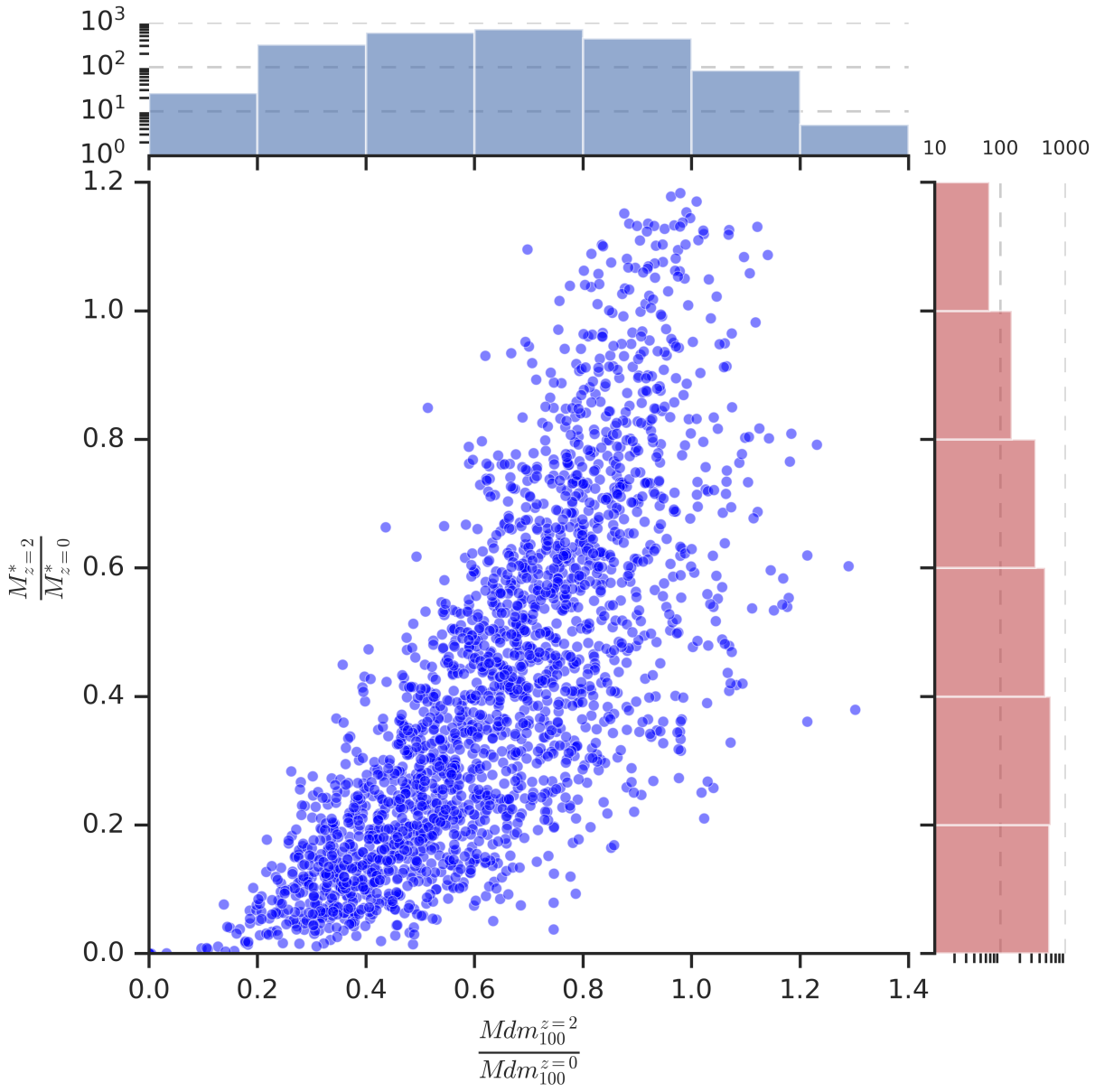

Figure 3.5: Fractions of dark matter mass and stellar mass at $z = 2$ with respect to their corresponding mass at $z = 0$. Stellar mass and dark matter mass is measured within 30 kpc and 100 kpc respectively from the subhalo center. The number of galaxies in each stellar and dark matter fraction bin is displayed respectively by two histograms that surrounds the main plot.

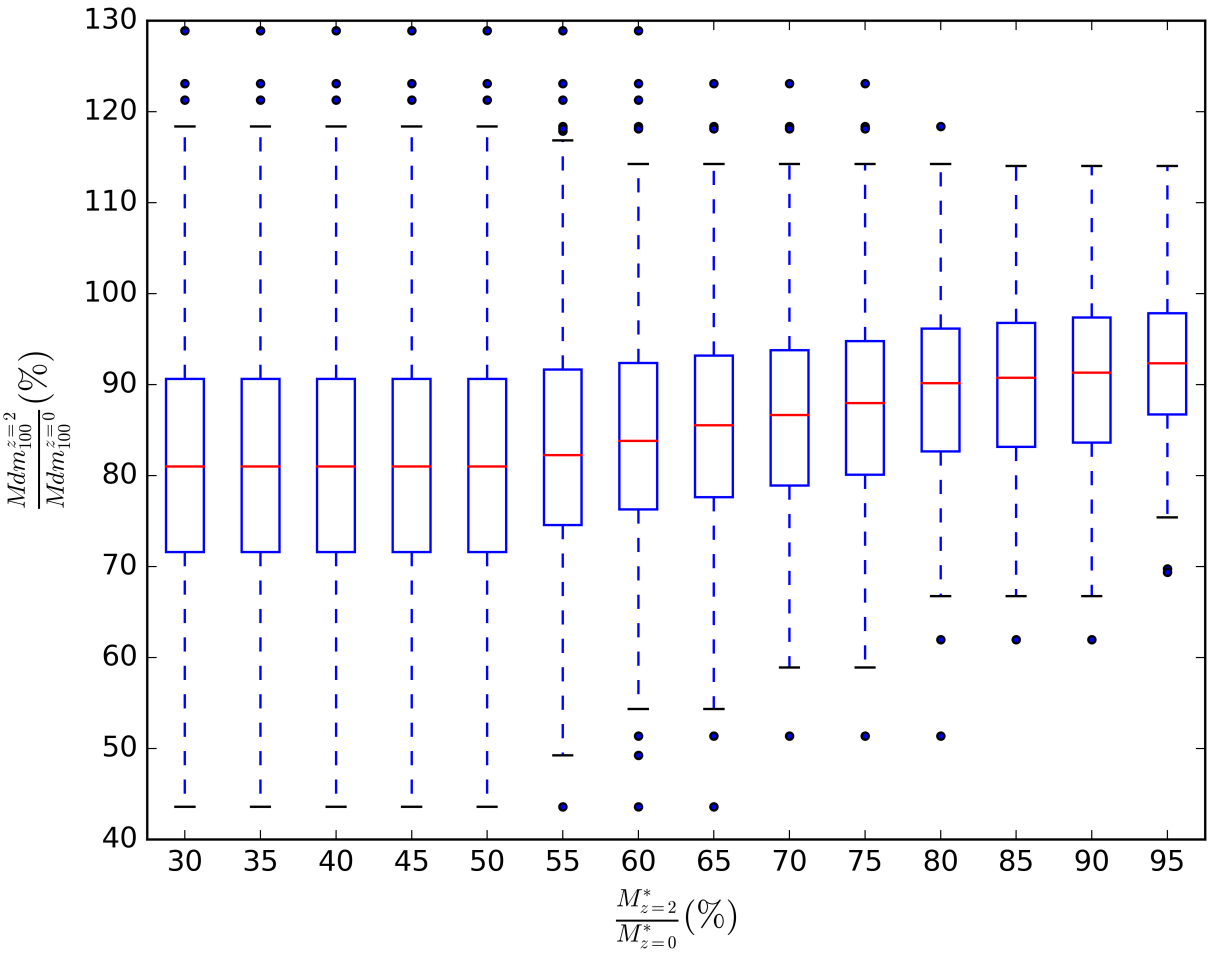

Figure 3.6: Statistics of the fraction of dark matter evolution for each constraint in the fraction of stellar mass evolution. The red line in the middle of each box represents the median of each relic sample. The edges of the box plot represents the two quartiles; Q1 (bottom edge) and Q3 (top edge). The whiskers extend from the box by 1.5x the inter-quartile range. The black dots outside the whiskers can be called as outliers, that have a deviation of more than 90% from the median value.

We categorize the massive ETGs that undergo a mass loss after $z = 2$, into three sets based on the nature of the mass loss, as shown in Figure 3.7. All three sets are selected by choosing ETGs with at least 5% increase in mass in a selected type of mass; i.e., 1) dark matter mass within a radial distance of 30 kpc (blue circle), 2) dark mass within a radial distance of 100 kpc (pink circle), 3) stellar mass within a radial distance of 30 kpc (green circle). The number in each region indicates the number of ETGs that belong only to the region considered. We

explored the mass profile of a few selected ETGs in each region (see APPENDIX), all the mass profiles we investigated do not show any abnormalities in the profile (smooth dark matter and stellar mass profiles at both $z = 2$ and $z = 0$).

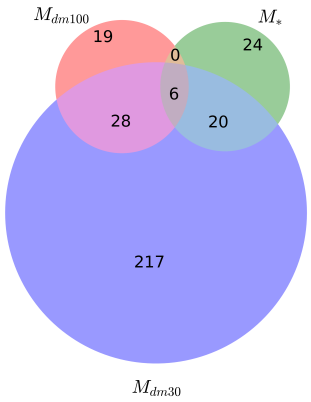

Figure 3.7: Number of relics with mass loss after $z = 2$. The Venn diagram shows different sets that are categorized based on the nature of the mass loss. Purple and green represent the galaxies that lost dark matter mass and stellar mass respectively, within 30 kpc after $z = 2$. Orange relates to the set of galaxies that lost dark matter mass within 100 kpc after $z = 2$.

3.4 Other Methods to Define Relicness

3.4.1 Selecting Dark Matter Mass

We explore how the aperture affects the relic properties of the sample. As explained in detail in Section 3.2.3, we adopt two definitions for the aperture, one with a fixed radial aperture around the subhalo center and second with an aperture enclosing a sphere having an average density of a chosen multiplier of the critical density of the universe.

First, we demonstrate how the median effective radius of selected relic samples behaves when the definition of relicness is varied with the cut-off value and the aperture used to define the dark matter mass. Figure 3.8 shows that smaller apertures (30 kpc and 50 kpc)

are not sensitive to imposing higher constraints on dark matter mass evolution. It shows that the apertures 100 kpc and 120 kpc demonstrate the highest sensitivity to the variation of relicness definitions. To demonstrate how each criterion changes when there is no criterion imposed regarding stellar mass evolution, we have included the median $R_{\rm eff}$ for relics with fraction of stellar mass evolution at least 10% (shown in color black).

Similarly, in Figure 3.9 we demonstrate how the selection of different radius based on over-densities affects the compactness of the relic sample. The fraction of dark matter evolution within R_{2500} (M_{2500}) is the most sensitive criterion to change in relicness. Due to the small sample size of relics, there is some artificial variations for higher dark matter mass fractions ($\sim 50\%$) related to the definitions of relicness using M_{500} and M_{200}.

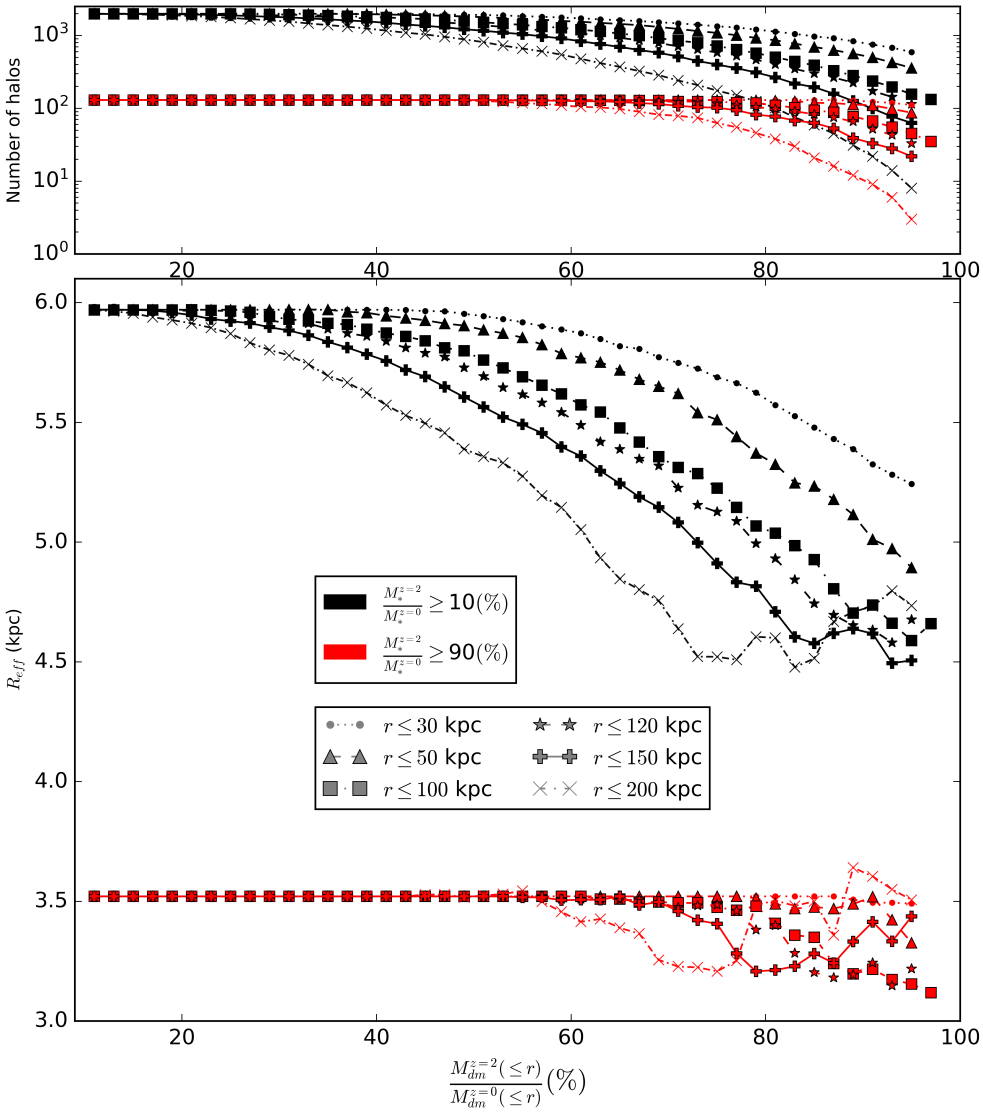

Figure 3.8: (Bottom panel) Median effective radius ($R_{\rm eff}$) of the relics as a function of relicness criteria that are defined using the evolution of dark matter within a fixed aperture. Each dot represents the median $R_{\rm eff}$ of the sample which is consistent of ETGs selected by imposing constraints on dark matter and stellar mass evolution since $z = 2$. Each radius chosen to define the dark matter mass is displayed by a unique shape. The minimum of the fraction of dark matter mass (within a radius "r") evolution ($M_{\rm dm}^{z=2}(\leq r)/M_*^{z=2}(\leq r)$) that used to define relicness, is shown in the x-axis. Blue and red data represents relics selected with a constraint of 10% and 90% in fraction of stellar mass evolution. (Top panel) number of halos in each relic sample.

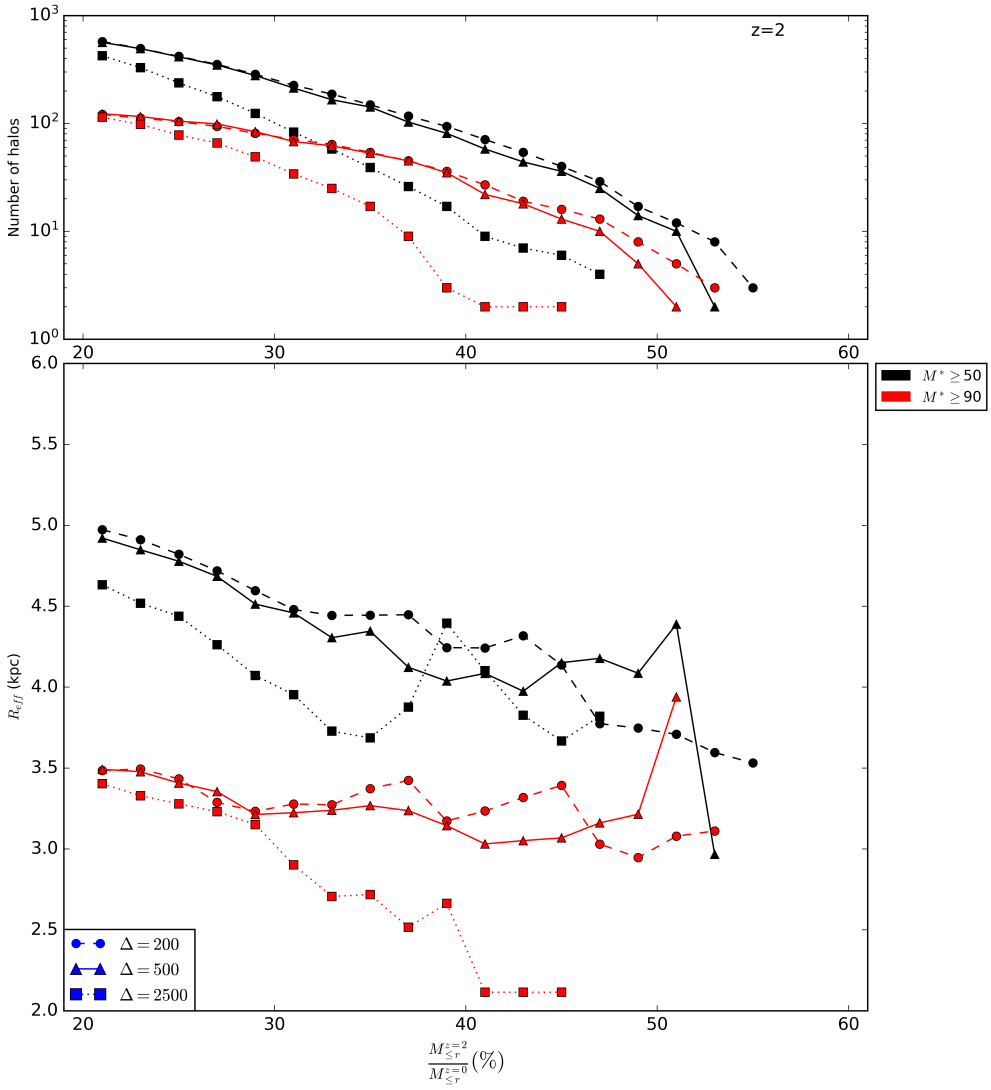

Figure 3.9: (Bottom panel) Median effective radius ($R_{\rm eff}$) of the relics as a function of relicness criteria that are defined using the evolution of dark matter within a overdensity based aperture. Each dot represents the median $R_{\rm eff}$ of the sample which is consistent of ETGs selected by imposing constraints on dark matter and stellar mass evolution since $z = 2$. Each radius chose to define the dark matter mass is displayed by a unique shape. The minimum of the fraction of dark matter mass (within a radius 'r_Δ') evolution ($M^{z=2}_{\rm dm}(\leq r_\Delta)/M^{z=0}_{*}(\leq r_\Delta)$) that used to define relicness, is shown in the x-axis. Blue and red data represents relics selected with a constraint of 10% and 90% in fraction of stellar mass evolution. (Top panel) number of halos in each relic sample.

3.4.2 Using Stellar Age to Define Relicness

In this section, we explore the feasibility of using the median stellar mass age as a criterion to define relicness, instead of using stellar mass evolution (used in the previous section). We keep $M^{z=2}_{\rm dm100}/M^{z=0}_{\rm dm100}$ as the metric to constrain dark matter mass as dark matter mass within a radius of 100 kpc has shown that it is the best metric that captures the compactness of relics. All the median stellar ages are calculated as explained in Section 3.2.2.

The correlation of the median stellar age with $M^{z=2}_{\rm dm100}/M^{z=0}_{\rm dm100}$ is shown in Figure 3.10. As expected, stellar age and dark matter mass evolution are positively correlated. Although for the widely used relicness definition which uses the constraint 90% on $M^{z=2}_{\rm dm100}/M^{z=0}_{\rm dm100}$, some relics show median ages younger than 9 Gyr. In Figure 3.11, we show how defining relics based on the median stellar age, change the compactness of the relics (median effective radius). Although constraining the sample to a median stellar age of 12 Gyr shows the most compact relic sample, it only captures a few relics (roughly 10).

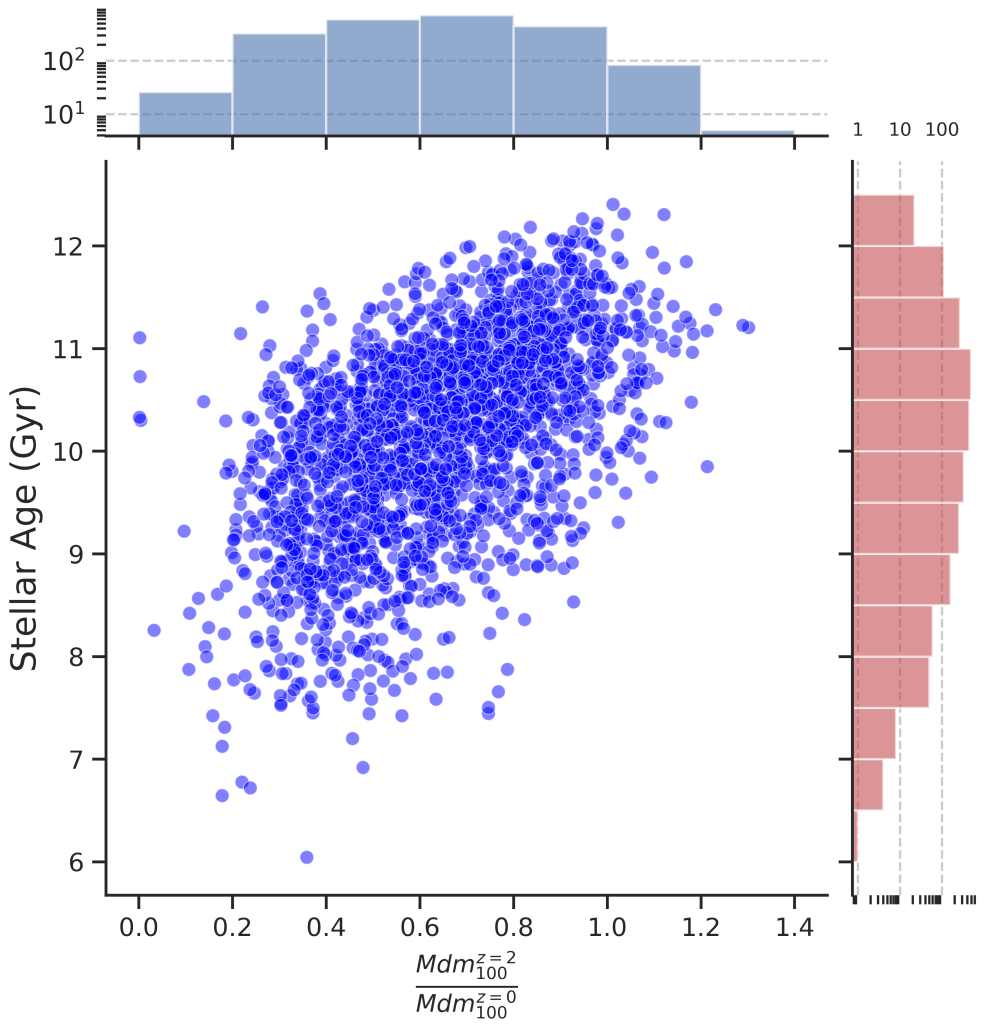

Figure 3.10: Median stellar age and the fraction of dark matter mass evolution for the sample. The bar plots on top and bottom shows the number ETGs in each stellar age and $M^{z=2}_{\rm dm100}/M^{z=0}_{\rm dm100}$ bins respectively.

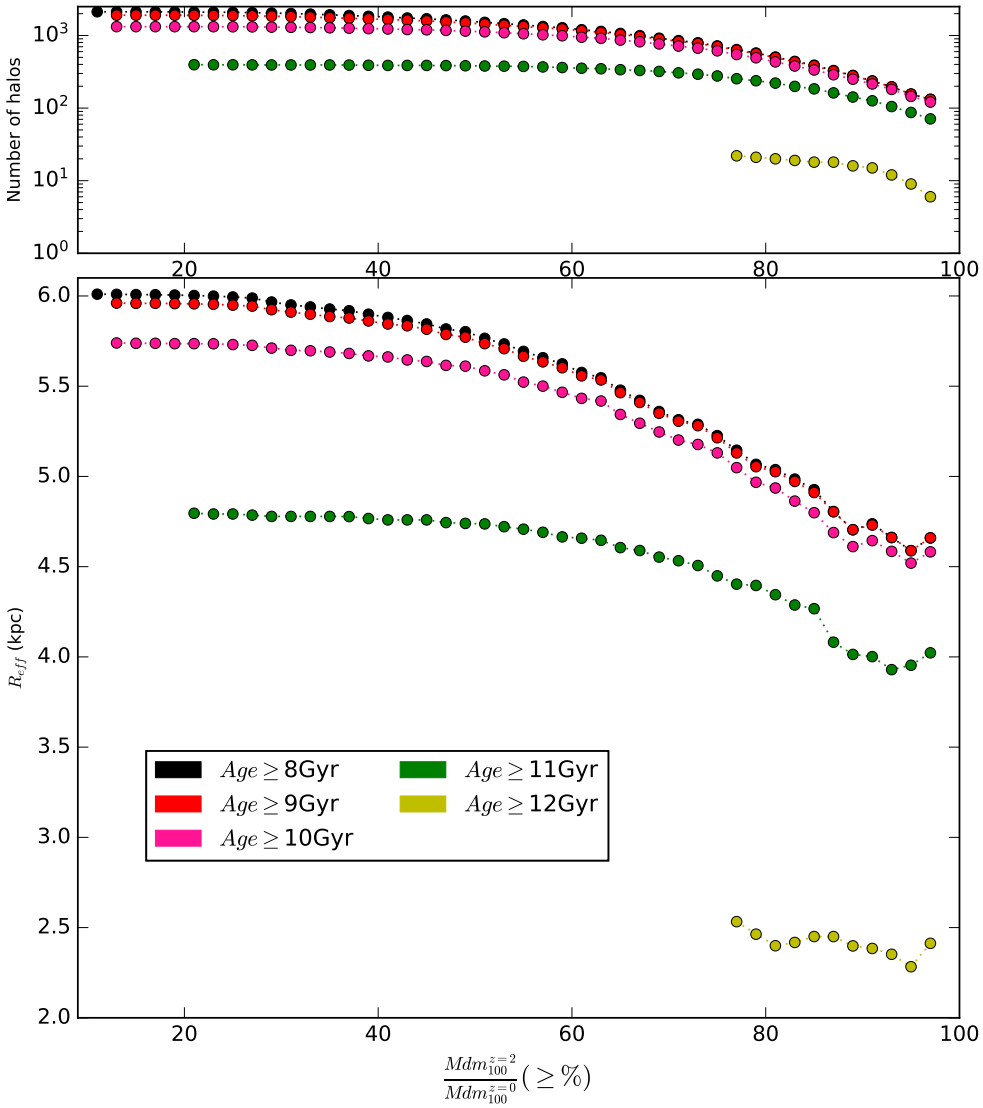

Figure 3.11: Median effective radius and the fraction of dark matter mass evolution of the relic samples, which are selected by cut-offs imposed on the median stellar age and $M^{z=2}_{\rm dm100}/M^{z=0}_{\rm dm100}$.

3.5 Dark Matter Concentration Correlation with Relicness

In this section we explore how the dark matter concentration (c_{200} and c_{2500}) is related to relic galaxies that are selected by physical properties (constraining the evolution of stellar and dark matter mass). c_{200} and c_{2500} are calculated following the procedure in Section 3.2.3.

Since dark matter concentration is negatively correlated with dark matter mass, we calculated the median dark matter concentration of mass bins that are evenly spaced in log space. In figure 3.12, we demonstrate the median c_{200} of each relic sample. It is shown that c_{200} of the relic population is positively correlated with the relicness scale, except for the highest mass bin (shown in pink), which is due to having a smaller sample size. A similar trend is shown for c_{2500} as shown in Figure 3.13.

In Figure 3.14, we plot M_{200} versus c_{200} and compare with the predictions from the ΛCDM relation for relaxed halos from Dutton et al. [53]. Relics (red points) have been selected following the definition in Section 3.3.1. From the figure, it is not evident that the relics have a higher concentration, as the relics are scattered around the ΛCDM relation for relaxed halos from Dutton et al. [53], although halos at the low mass end ($\lesssim 10^{13}\ M_{\odot}$) show a larger postive deviation from the ΛCDM relation.

In Figure 3.15, we plot M_{2500} versus c_{2500} and compare with the predictions from the $c_{2500}M_{2500}$ for relaxed halos derived in Section 5.2.2. Relics (red points) have been selected following the definition in Section 3.3.1. Similarly to the case of c_{200}, it is not evident that the relics have a higher concentration, as the relics are scattered around the ΛCDM relation for relaxed halos from Dutton et al. [53] except halos at the low mass end ($\lesssim 3 \times 10^{12}\ M_{\odot}$) weighted toward having more positive outliers.

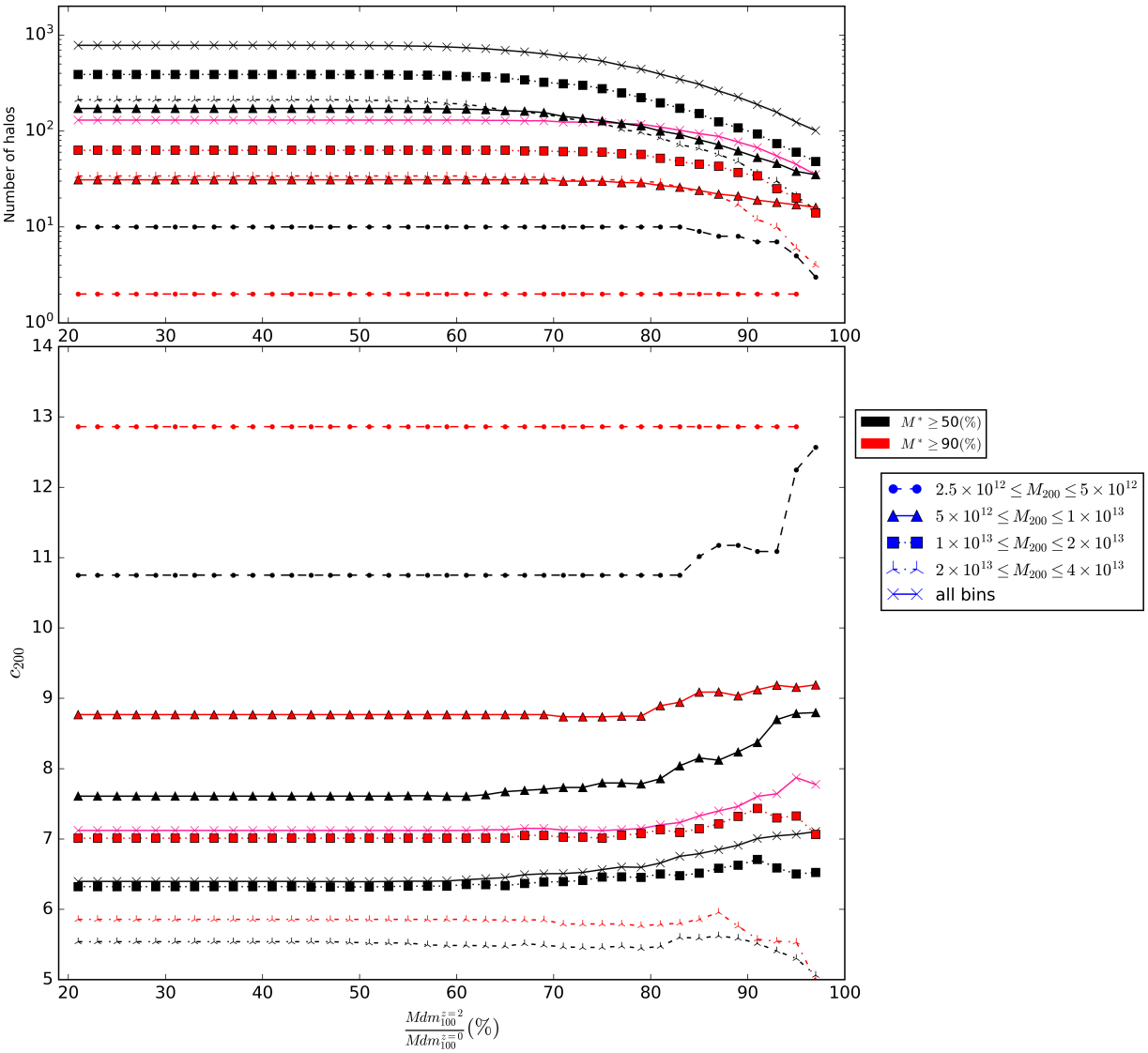

Figure 3.12: Medians c_{200} of relic samples for different M_{200} bins.

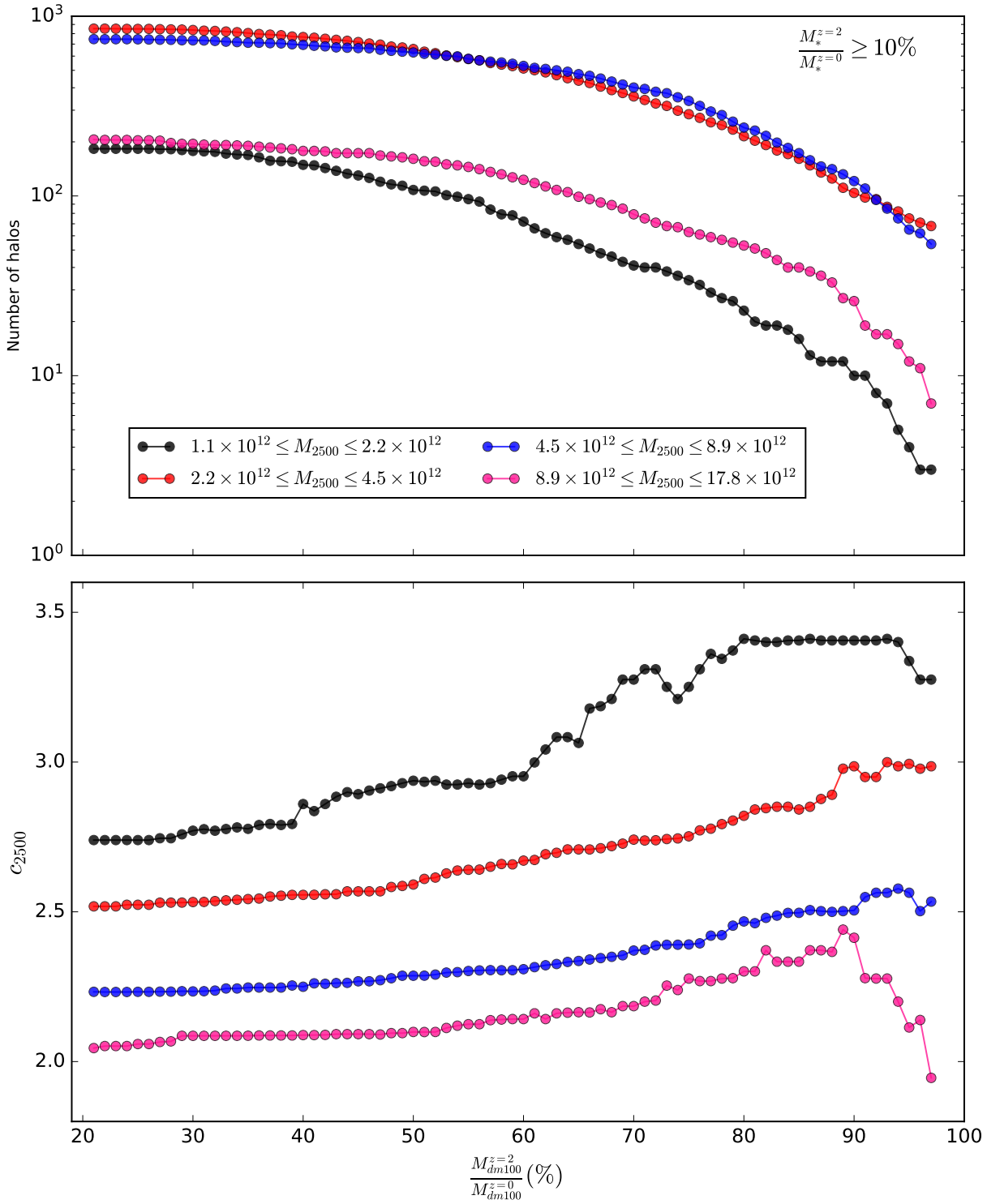

Figure 3.13: Median c_{2500} of relic samples for different M_{2500} bins.

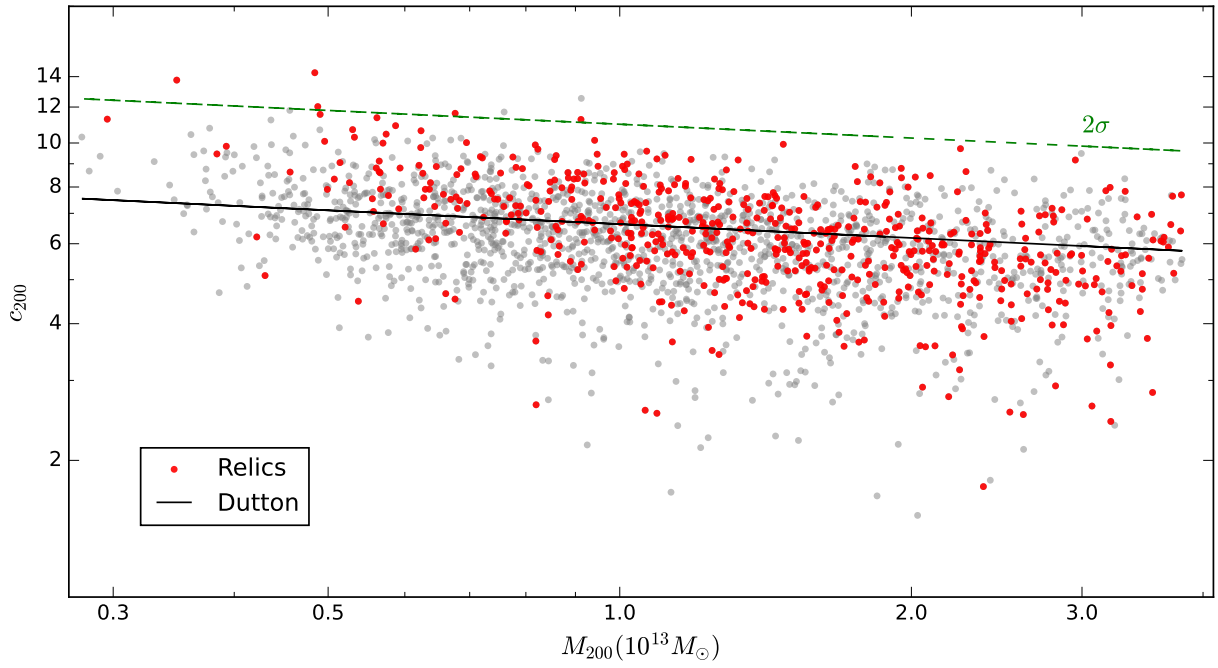

Figure 3.14: Dark matter masses (M_{200}) and dark matter concentration (c_{200}) for the sample. The black line is the ΛCDM relation for relaxed halos from Dutton et al. [53]. The dashed green line is 2σ (scatter in M_{200}-c_{200} relation; adopted from Dutton et al. [53]) above the black line.

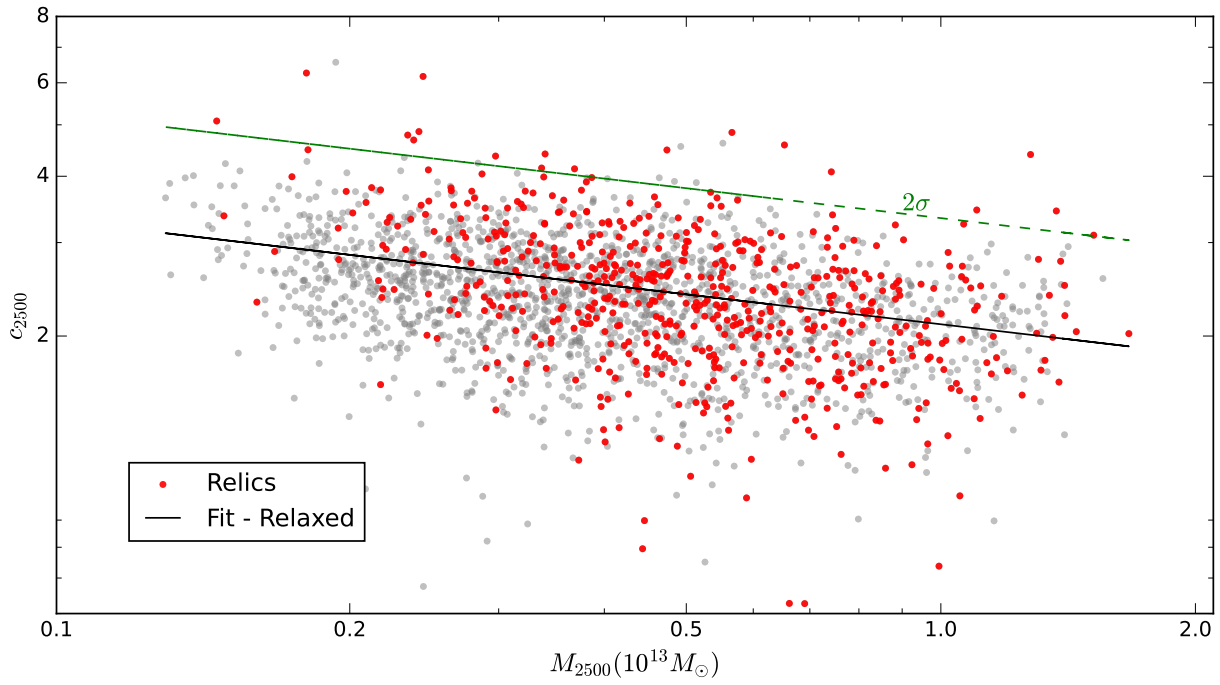

Figure 3.15: Dark matter masses (M_{2500}) and dark matter concentration (c_{2500}) for the sample. The black line is the power law fit for $c_{2500} - M_{2500}$ of relaxed halos derived in Section 5.2.2. The dashed green line is 2σ (scatter in $c_{2500} - M_{2500}$ relation derived in Section 5.2.2) above the black line.

3.6 Discussion

This section quantifies the "relicness", a metric that dictates how passive an ETG has evolved, using different physical criteria. The relic definition motivated by previous work shows promising results, as the median effective radius for relics is almost twice that for non-relics (in Figure 3.1). But the median for relics is roughly 3.5 kpc because a significant number of relics have $R_{\rm eff}$ greater than 4 kpc. Also, there are only a few relics that can be categorized as ultra compact galaxies. This could be primarily due to the fact that inferred effective radii are higher than the median effective radii predicted by $M_* - R_{\rm eff}$ from observations (see Chapter 2.2.6). Overall, the relics selected by this definition agree well with the observed relics, as Figure 3.3 and Figure 3.2 show an old population (age greater than 10 Gyr) of stars in the relics.

As illustrated in Figure 3.6, the evolution of dark matter and stellar mass is coupled. Constraining stellar mass evolution constrains dark matter evolution, although it is not a perfect correlation primarily due to the the difference in the apertures. As shown in Figure 3.5, there is a larger scatter in change in dark matter mass for a given stellar mass change. We believe this is because dark matter mass is measured within a larger radius (100 kpc); therefore, the dark matter mass is affected more by the environmental effects (e.g., tidal stripping, flybys).

Overall, dark matter concentrations of the relic sample gets larger with more constraint in dark matter evolution, therefore perhaps reflecting an isolated evolution. However, Figure 3.14 shows that the relics do not show a large deviation from the ΛCDM relation for relaxed halos. Also, it is important to note that we did not confirm that the relics are relaxed. Perhaps, only considering relaxed halos might impact the statistics of the relic sample.

3.7 Conclusion

We develop criteria to define relic galaxies physically in TNG300 and examine whether they produce the key stellar properties of massive relic galaxies. We showed that just constraining dark matter and stellar mass evolution since $z = 2$ is enough to produce a relic sample that mimics the observed properties of compact galaxies.

By analyzing compactness of the relic samples selected from various relicness definitions (evolution of dark matter mass within fixed and overdensity-based radii and median stellar age), we showed that constraining the evolution of the dark matter within a radius of 100 kpc ($M^{z=2}_{\rm dm100}/M^{z=0}_{\rm dm100}$) combined with constraining the stellar mass evolution ($M^{z=2}_{*}/M^{z=0}_{*}$) is the best metric to define relicness. Finally, we found that the relics selected by the definition in Section 3.3.1 ($M^{z=2}_{\rm dm100}/M^{z=0}_{\rm dm100}$ and $M^{z=2}_{*}/M^{z=0}_{*} \geq 90\%$), do not show a high dark matter concentration except for the lower mass end.

Chapter 4

Selecting Samples of Massive Relics Candidates Based on Compactness in TNG300 Simulation

4.1 Introduction

It is generally accepted that massive ETGs were created through a two-phase process; where phase 1 which produces a compact galaxy (i.e., "red nugget") takes place at early times ($z \gtrsim 2$) followed by the dry merger-driven phase 2 (see Section 1.1.1 for more details). Studying the end of Phase 1 is of great importance, which will shed light on galaxy formation theories; e.g., it will help to obtain a deeper understanding of the processes that drive the growth and transformation of the earliest galaxies. Although the red nuggets provide ideal testing grounds to study the end of Phase 1, unfortunately it is not possible because they are located too far away to obtain detailed full mass mapping (it is only possible within the effective radius). An alternative approach is to study local analogs of red nuggets that are

believed to have not gone through the second-phase evolution; i.e., "relics" [208].

Owing to its importance for our study of relic galaxies, we briefly review how the search for relicness has developed since the first identified relic, describe the process to look for relics following the methods/definitions in the observations and compare with physically defined relics (as in Chapter 3), and finally investigate whether relics show a higher dark matter halo concentration as observed in Mrk 1216.

4.1.1 Historical Development

The first identified massive relic is NGC 1277 [208], which showed a very old stellar population ($\gtrsim$ 10 Gyr) and an effective radius that follows the stellar mass-size relationship for $z \sim 2$. They postulated that this is a passively evolved analogue of massive ETGs at $z \sim 2$. This was not a coincidence for a single galaxy showing such properties, as later there were other similar observations. For example, Yıldırım et al. [226] identified 16 local compact ETGs (including NGC 1277) with such characteristics, from the Hobby-Eberly Telescope Massive Galaxy Survey [212] which was initiated to obtain spatially resolved spectroscopic data of a large number of galaxies with the ultimate goal of measuring the dynamical mass of their supermassive black holes.

Following the development of telescopes and emergence of larger surveys, many more relics were identified (e.g., Buitrago et al. [17] identified 4 relics in the survey "Galaxy and Mass Assembly", Spiniello et al. [185] identified 10 relics at redshifts $0.17 < z < 0.39$ in the survey "The INvestigating Stellar Population In RElics" and Lisiecki et al. [103] identified 77 relics in the survey VIMOS[1]). Nevertheless, the exact definition of a relic galaxy is debatable due to the various criteria for compactness and the lack of consensus on whether to include age limit on stellar populations. Therefore, it is harder to compare directly the relic samples

[1]Not exactly local red nuggets (relics) since they are at a higher redshift $0.5 < z < 1$.

from different studies.

The adoption of various definitions to define relics leads to the idea of "degree of relic" (hereafter we call it "relicness") [58]. Relicness is a measure of how passive an ETG in their evolutionary path; i.e., high relicness means that they are extremely passive (ultra compact and, in some definitions, have an extremely old stellar population). With this idea, the relics are categorized into two groups [185]; i.e., extreme relics and relics. The present state of knowledge does not encompass the physical origin of the relicness; e.g., it is debatable whether it is related to the local environment around the relic (isolated versus dense environments) [58, 179].

One of the most interesting properties that have been observed related to the extreme relic Mrk 1216 is that it has an extremely large dark matter halo concentration [22]. There have been only few studies on the dark matter profiles of relics and even fewer on dark matter concentrations. Therefore, there are many unanswered questions; e.g., do other extreme relics show high dark mater concentrations? Does dark-matter evolution follow the stellar evolution in these relics?

With the development of hydrodynamical simulations, where they are equipped with merger trees that can trace the growth history of halos, it has created a great opportunity to study relics. Nevertheless, only a handful of studies have investigated relics in cosmological simulations, following the definitions of relicness used in observations. For example, Wellons et al. [222] and Wellons et al. [221] studied the evolutionary paths of massive compact galaxies from $z = 2$ in the simulation Illustris (the older version of TNG300). Their main focus was to identify the effect of the environment on massive ETGs that maintained their compactness from $z = 2$ to $z = 0$. One major concern of the two studies is that they do not have a large number of ETGs in their sample, since Illustris is a smaller box and therefore does not produce ETGs with $M_* > 10^{11} M_\odot$ (the maximum sample size of massive ETGs out of these two studies is 35 ETGs). Also, they do not focus on dark matter properties of relics

or consider the idea of relicness in their studies.

Another study that focuses on relics in simulations is done by Flores-Freitas et al. [59], where they use the simulation TNG50 (higher resolution than TNG300 but smaller box size). They used a ranking system to quantify the degree of relicness and used multiple distinct systems to define the relicness. All their systems for the definitions include multiple criteria similar to criteria used in observations; e.g., a maximum size (stellar half-mass radius ≤ 4 kpc or based on stellar mass-size relationship), and age of the stellar population. They identified five relic analogues, but including the most extreme relic, three of them lost dark matter after $z = 2$. They propose that it could possibly be due to tidal effects from galaxy flybys[1]. Therefore, it leads to questioning whether they are truly relics (i.e., where there is no tidal effects from close flybys or infalls). Also, this study suffers from having a small ETG sample because TNG50 has a box size of approximately 50 Mpc at $z = 0$. To the best of our knowledge, so far no one has studied massive relics and their degree of relicness in a large hydrodynamical simulation. Additionally, there is no study exploring the dark matter profiles (especially dark matter halo concentration) of a large relic population.

This chapter is organized as follows. Section 4.2 describes the method used to select ETGs for the study in TNG300. In section 4.3 we compare three different relic definitions from the literature and select the best definition. Next, in Section 4.4, we analyze the dark matter halo concentrations of the selected relics. Finally, Section 4.5 and Section 4.6 provides our discussion and conclusions respectively.

[1]When two independent galaxy halos come into contact with each other (interpenetrate) without merging, it is known as a flyby. See Sinha et al. [178] for more details.

4.2 Sample Selection

Although the stellar masses of massive relics are observed to be approximately $10^{11} M_{\odot}$, there is a variety of mass cuts adopted in different studies (see Table 4.1). We chose ETGs at $z = 0$ with stellar mass[1] (M_*) $\geq 5 \times 10^{10}$ $M_{\odot}$, to illustrate mass and size values for a larger sample. To minimize the artificial effects of subhalo switching, we selected subhalos, which are identified as the primary subhalo of a halo at both redshift 2 and 0. Since we are motivated by Mrk 1216, we impose subhalo's M_{200} to be in between 10^{12} $M_{\odot}$ and 5×10^{13} $M_{\odot}$. This gives us a total of 8554 ETGs.

4.3 Different Definitions for Relics

4.3.1 Definitions

Table 4.1 shows the three different definitions we compare and the extreme relic (ultra compact) definition used in three different studies. All definitions (except the definition for ultra compact relics) impose a stellar mass-dependent effective radius cut-off (column $R_{\rm eff}$ constraint). Damanjov et al. [39] do not apply a cut in stellar mass or age of the stellar population. Although Van der Wel et al. [213] use a cutoff for M_* (i.e., stellar mass above $7.2 \times 10^{10} M_{\odot}$), they do not restrict the age of the stellar population. Trujillo et al. [206] impose constraints on both M_* and the stellar population. In Figure 4.1, we show the three different criteria used to constrain $R_{\rm eff}$ in each definition.

[1]Stellar mass within 30 kpc from the subfind center

Table 4.1: Definitions used in the literature to define massive relic galaxies.

Study	$R_{\rm eff}$ constraint (kpc)	M_* constraint ($M_\odot$)	Stellar Age (Gyr)
Damanjov	$R_{\rm eff}/(M_*/10^{10})^{0.568} \leq 5.55$	None	None
Van der Wel	$R_{\rm eff}/(M_*/10^{11})^{0.75} \leq 2.5$	7.2×10^{10}	None
Trujillo	$R_{\rm eff}/(M_*/10^{11})^{0.56} \leq 2.72$	8×10^{10}	10
Trujillo ultra compact	$R_{\rm eff} \leq 2$	8×10^{10}	10

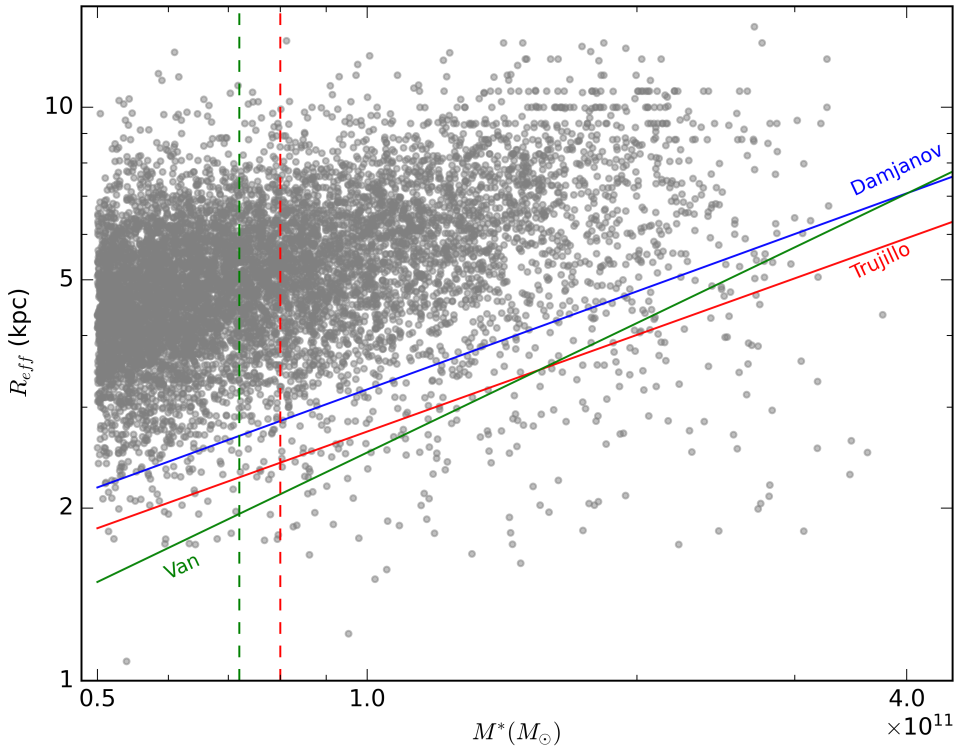

Figure 4.1: Galaxy mass-size constraint for each definition of relics. The blue, green and red lines show the $R_{\rm eff}$ constraints for the definitions Damjanov [39], Van [213], and Trujillo et al. [206] respectively. The vertical dashed lines represents the mass constraints used in the appropriate definitions and they are color coded appropriately. ETGs (grey dots) above each line is considered a relic (for Trujillo and Van, it also requires ETGs to be to the right of the appropriate dashed line).

4.3.2 Performance of Different Definitions

It is ambiguous to quantify how well each definition performs in TNG300 without analyzing the merger history of each and every relic they produce. Analyzing merger history for a large sample is computationally expensive. Nevertheless, it is expected that these relics should not have changed their dark matter and stellar masses after redshift $z \sim 2$. Therefore, we use the fraction of dark matter mass and stellar mass evolution since $z = 2$ (similar to Chapter 3) of the relic samples selected by each definition and compare their statistics (e.g., median, quartiles)[1]. Finally, we chose the best definition based on how well they constrain the dark matter mass and stellar mass evolution (i.e., highest median of stellar and dark matter masses fractions of evolution).

[1]We are not using mean and standard deviation since the the distributions are far from gaussian.

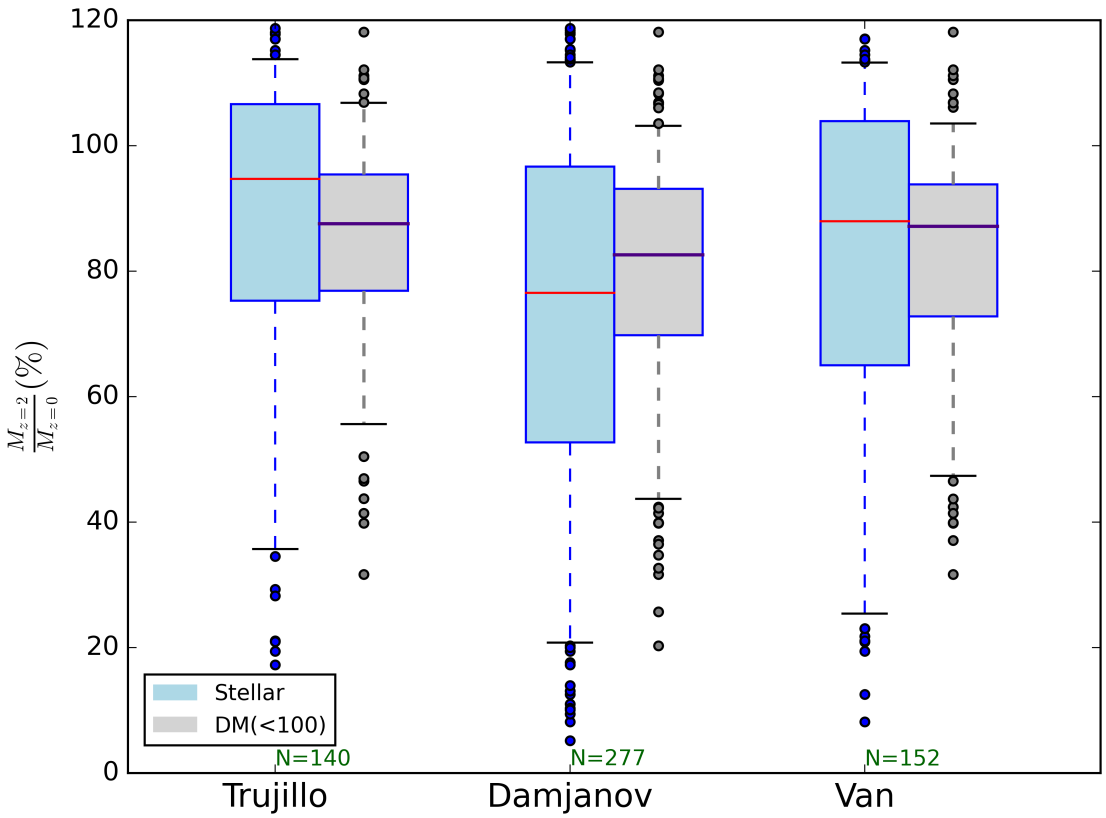

Figure 4.2: The blue and grey color shows the fractional evolution of stellar mass and dark matter mass respectively. The solid lines represents the medians. The boxes top and bottom represents the 75% and 25% quartiles respectively. The whiskers extends to 90% of the fractional mass evolution. The outliers (above or below 90% of the median) are indicated as dots. The number of relics produced by each definition is mentioned at the bottom of each box plot.

Figure 4.2 shows the box plots for the fractional evolution of dark matter and stellar masses predicted by each definition. Dark matter mass is measured within a 100 kpc aperture and stellar mass is within 30 kpc radial distance from the galactic center. Trujillo definition shows the largest median for both dark matter and stellar masses and its dark matter fractional evolution is marginally higher than the other two methods. Therefore, we select Trujillo's definition for the analysis in the following section.

4.4 Dark Matter Concentration of the Relics

We investigate dark matter halo concentration (c_{200}) of the relics that follows the Trujillo definition. c_{200} and M_{200} are calculated as described in Section 3.2.3. Figure 4.3 shows c_{200} and M_{200} values of the whole sample (selected in Section 4.2 with the addition of extra constraint on stellar mass following Turjillo's deifnition; i.e., $M_* \geq 8 \times 10^{10} M_\odot$). c_{200} for all the relics is overall higher than the non-relics and ΛCDM relation for relaxed halos from Dutton et al. [53] (hereafter referred as c_{200} from ΛCDM).

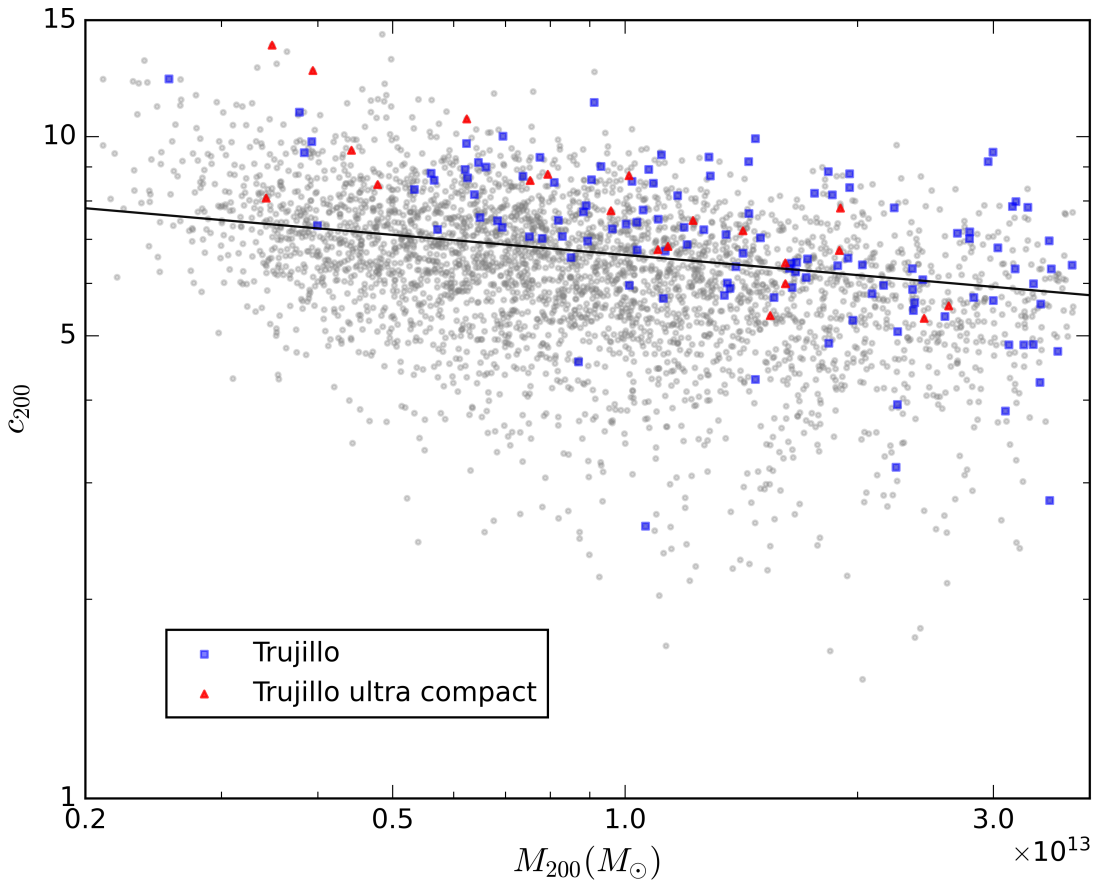

Figure 4.3: $M_{200} - c_{200}$ for the whole sample. Blue squares and red triangles represent relic and extreme relics selected following the Trujillo's definition. The black line shows the ΛCDM relation for relaxed halos from Dutton et al. [53].

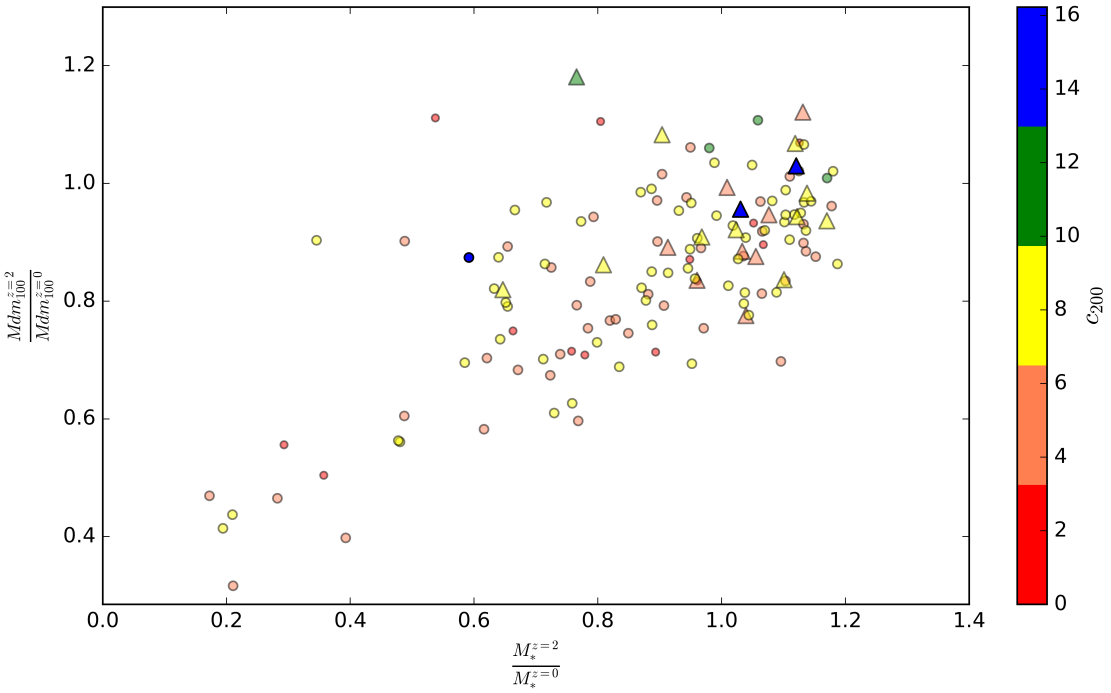

Figure 4.4: Fractional dark matter and stellar masses evolution values for the relics. The color map shows the c_{200}. Triangles represents extreme relics while dots represents relics that are not ultra compact.

4.5 Discussion

This chapter demonstrated how relic galaxies are defined by integrating the idea of "degree of relicness" in the observations and how well it predicts relics in the hydrodynamical simulation TNG300. In the comparison of three different methods in Section 4.3, as Figure 4.2 shows the predictions from Trujillo's definition are not largely different from the other two definitions, as the other two also constrain the stellar mass and dark matter evolution since $z = 2$. Although all three definitions constrain dark matter and stellar mass evolution, there are few ETGs ($\sim 5\%$ of the relics) that show dark matter and/or stellar mass evolution. These relics should be analyzed individually to determine whether the mass loss is due to a physical process (e.g., tidal effects from flybys) or numerical issue (e.g., miss classification of particles related to the halo by the halo finder).

Figure 4.3 shows that the relic sample selected by Trujillo's definition shows a moderately higher c_{200} than the non-relics. The difference is not significant. Assuming the log scatter of c_{200} (σ_{c200}) = 0.1 (scatter in ΛCDM $M_{200} - c_{200}$ from Dutton et al. [53]), the total relic sample showed a median of $0.38\sigma_{c200}$ above from ΛCDM c_{200} relation. Extreme relics (ultra compact) showed a little larger c_{200} ($0.61\sigma_{c200}$ above from ΛCDM c_{200} relation). Although these relics are compared with c_{200} for relaxed halos in the ΛCDM model, the relics are not tested for whether they are relaxed or not. Due to this, the results could be slightly altered.

Figure 4.4 compares the Trujillo's relic definition with physical properties (i.e., evolution of dark matter and stellar masses since $z = 2$). The fraction of relics that fits the physical definition used in Sec 3.3.1 (i.e., at $z = 2$, at least 90% of the dark matter and stellar masses have assembled), is roughly 1/3. Additionally, more than half (57%) of extreme relics will be classified as relics from the physical definition. Also, the figure demonstrates a higher c_{200} for the relics, but there is not enough evidence to propose a correlation between c_{200} and relicness (both methods, which are defined following Trujillo and definition using physical

properties).

4.6 Conclusion

We present the relic analogues in the hydrodynamical simulation TNG300 that was selected following three different definitions used in observational studies, that is based on compactness. We show that the definition used by Trujillo et al. [206], which uses an additional constraint on stellar population's age, is slightly suited for the simulations than the other two.

Relicness defined based on compactness does not follow the definition based on dark matter and stellar mass evolution (used in Section 3.3.1) completely; i.e., only one third of the relics identifed by the compactness criteria are classified by the latter definition. We find a higher dark matter halo concentration but it is not a significant increase ($0.38\ \sigma_{c200}$) from the ΛCDM $c_{200} - M_{200}$ relationship. For extreme relics (ultra compact), this difference is a bit higher ($0.61\,\sigma_{c200}$). Overall, extreme relics show a more constrained dark matter and stellar mass evolution since $z = 2$, but a larger sample of relics is needed.

Chapter 5

Highly Concentrated Dark Matter Halos in the TNG300 Simulation

5.1 Introduction

As we presented in Section 1.1, it is widely accepted that each galaxy is formed within a dark matter halo. The growth of the galaxies and dark matter halos are closely intertwined, therefore, study of the growth history of dark matter halo may serve as a valuable tool to investigate the two-phase galaxy formation. In search of massive relic galaxies, looking for halos that are formed early and went through an isolation growth will serve as an important method distinct from the two other methods we employed in Chapter 3 and Chapter 4. The dark matter halo concentration (e.g., c_{200}) is possibly one of the best estimators that is related to the halo formation history and environment around galaxies. Motivated primarily by the estimation of extremely high dark matter halo concentration (c_{200}) of the massive relic Mrk 1216, we briefly review how well the simulations can be used to compute the concentrations, describe the method we adopted to compute the concentrations

for the hydrodynamical cosmological simulation TNG300, and finally investigate the properties including stellar mass-size, gas fractions, and environmental effects for extremely highly concentrated halos.

5.1.1 Dark Matter Halo Density Profile

Following the spherical collapse model, it is predicted that the initial matter overdensities collapse to form a system that reaches an equilibrium state that satisfies the virial theorem, through violent relaxation[1]. This virialized structure is called dark matter "halo" and for an EdS cosmology[2], it is shown that the dark matter halo can be characterized by an overdensity (ρ); $\rho = 178\,\overline{\rho_m}$ [32] where $\overline{\rho_m}$ is the mean matter density of the universe (since in an EdS universe $\overline{\rho_m}$ is the same as the critical density ρ_c, in general ρ_c is used to define overdensity).

Virialized dark matter halos do not have a well-defined boundary, leading to numerous ways to define the mass and the size of the halo. The most common method is to use the "virial radius" (R_Δ), defined as the radius of a sphere that encloses a spherically averaged overdensity of $\Delta_c\rho_c$, where Δ_c is the critical overdensity for virialization. Although in an EdS universe $\Delta_c \simeq 178$ throughout the whole time, but, in the ΛCDM universe where dark energy becomes dominant at later times, Δ_c drops. Therefore, typically a fixed value (Δ) is used for the overdensity that is greater than Δ_c; e.g., $\Delta = 200$ (most frequently used), 500, 2500. Following the definition of R_Δ, virial mass (M_Δ) is given by

$$M_\Delta = \frac{4\pi}{3}\Delta\rho_c r_\Delta^3 \tag{5.1}$$

[1]It is a collisionless relaxation where orbital energies are redistributed in a strongly-time varying gravitational potential (see Lynden-Bell [106] for more details).

[2]Einstein-de Sitter cosmology defines the universe as flat, matter dominated without the cosmological constant.

Few decades ago, using N-body simulations, Navarro, Frenk, & White [134, 135] showed that the spherically averaged density profile of relaxed halos can be modeled by a two-free parameter function (that is, the NFW model);

$$\rho(r) = \frac{\delta\rho_{crit}}{(r/r_s)(1 + r/r_s)^2} \tag{5.2}$$

where r_s is called the scale radius which is assigned to the radius where the logarithmic slope of the density becomes -2. r_s is related to the concentration of the halo, therefore, it is used to define the concentration (c_Δ) within a virialized region of the halo ($r < R_\Delta$); $c_\Delta = R_\Delta/r_s$. Due to the popularity of overdensity 200 ($\Delta = 200$), it is more common to use c_{200} to quantify concentration. Although in some cases it is more useful to use other estimators; e.g., c_{2500} is frequently used in studies that use X-ray emitting gas to map the halo mass profile of local massive ETGs. Because X-ray observations typically capture data only up to a smaller radius $\sim R_{2500}$ (e.g., Mrk 1216 [22]).

Halo concentration is a vital characteristic of a halo, that depends on various properties of the halo and the environment. The most primary property initially found by Navarro et al. [134], is its mass dependence (M_{200}); i.e., c_{200} is anticorrelated with M_{200} (we discuss in detail in Section 5.1.2). Additionally, Bullock et al. [19] found some interesting characteristics of median $c_{\rm vir}$ for a given halo mass[1]; 1) Redshift dependence; inversely proportional to (1 + z), 2) Environment dependence: greater for halos in dense environment.

Halos interact with their environment constantly and some times it can lead them out of their virial equilibrium which are being called "unrelaxed" halos. There are few different metrics adapted by different studies to classify these two categories, with overlapping conditions [109] and some imposing more constrains [140] and we will discuss in the section It has shown

[1]For halos in the mass ($M_{\rm vir}$) range $10^{11} - 10^{14}\ h^{-1}M_\odot$.

that unrelaxed halos don't follow NFW well compared to relaxed halos [208].

5.1.2 Concentration Dependence on Mass

There is overwhelming evidence for a negatively correlated median halo concentration - mass relationship at a given redshift [19, 52, 53, 163] and usually the relationship is fitted as a power-law. In general, most studies explore the median relation $c_{200} - M_{200}$, but there are few studies conducted on $c_{\rm vir} - M_{\rm vir}$ [19, 53] and $c_{2500} - M_{2500}$ [163]. From here on, we choose $c_{200} - M_{200}$ as the median dark matter halo mass - concentration relationship, unless it is specified.

One of the largest studies on this relation is conducted by Dutton et al. [53], where they have studied more than 90 000 halos at $z = 0$ using 12 N-body simulations. Therefore, it is popular to use their results as the expected relation in ΛCDM model. In this study, it was confirmed that for a given M_{200}, c_{200} follows a log-normal distribution that has a scatter ($\sigma_{\log c} \sim 0.1$) about the median. Bullock et al. [19] argued that the physical origin of the scatter is for various reasons including, due to the complicated formation histories of the halos (i.e., interactions with other halos and tidal stripping that halos go through) and the local environmental effects. The environmental dependence can affect $c_{\rm vir}$ in numerous ways. First, in general, halos in a dense environment typically collapse earlier (because the universe was denser), resulting in a larger $c_{\rm vir}$. Second, halos that reside in a dense environment are likely to experience extreme collapse histories and frequent merger events. Third, tidal stripping may lead to higher a $c_{\rm vir}$ in halos, as it may cause steepening of their outer density profile [145].

5.1.3 Observations

There are a variety of methods to estimate c_{200} in observations. The two most popular methods utilize X-ray emitting gas and gravitational lensing separately. The first method, X-ray observations, hydrostatic equilibrium analysis of the hot gas is employed to estimate the concentration. Although this method produces reliable results, for a massive local ETG, its temperature profile is limited to a smaller radius (e.g., $\sim R_{2500}$), therefore, typically for c_{2500} is calculated and then its extrapolated to R_{200} to estimate c_{200} (under the assumption that the halo density profile follows the NFW profile up to R_{200}).

Few galaxies with extremely high dark matter halo concentrations (i.e., $c_{200} > 5\,\sigma_{c200}$) have been observed including NGC 6482 [20], NGC 1600 [170], Mrk 1216 [22]. While the first two are considered to be fossil groups (isolated elliptical galaxy surrounded by an extended bright X-ray halo [159]), Mrk 1216 is identified as a massive relic galaxy. Since fossil groups have an early formation time, it is expected to have concentrations that are positive outliers in the concentration - mass relation. It is currently uncertain if massive relics are positive outliers in concentration. In Chapter 3 and Chapter 4, we presented evidence that the massive relic population in TNG300 does not show a large positive c_{200}. In this chapter we explore whether extremely highly concentrated halos can be identified as massive relics.

This chapter is organized as follows. Section 5.1.2 presents the method we implemented to derive the concentration-mass relationship for halos in TNG300, Section 5.3 we analyze properties of concentration outliers and search for galaxies similar to Mrk1216, Section 5.4 provides our discussion and finally Section 5.5 provides our conclusions.

5.2 Dark Matter Concentration - Mass Relation in TNG300

5.2.1 Sample Selection

All selected subhalos are identified by the SUBFIND algorithm, and the data are publicly available. Motivated by the relic galaxy Mrk 1216 which is a massive compact galaxy ($M_{200} \geq 10^{12} M_{\odot}$), we choose the M_{200} accordingly for the selection at $z = 0$. The summary of the selection criteria is

- $10^{12} M_{\odot} \leq M_{200} \leq 3 \times 10^{13} M_{\odot}$.
- Primary subhalo at $z = 0$
- Subhalo flag = 1

The subhalo flag indicates whether the subhalo has a cosmological origin or not. Not all objects recognized by the SUBFIND (see Section 2.2.1) could be considered as galaxies. Some subhalos may not have collapsed as a result of the structure formation process. The subhalo flag = 1 indicates that the subhalo structure has collapsed from the galaxy formation model and has enough baryonic mass. This produces a sample of 31060 halos (hereafter sample A).

We also choose a subsample of relaxed halos. Relaxation of a halo is determined by two criteria that depend on the following metrics (following Neto et al. [140]),

- Center of mass displacement (d_{CM}): d_{CM} is defined as the offset between the center of mass (coordinates $X_{\rm cm}$) of the halo and the subhalo center (coordinates X_{gc}); i.e., $d_{CM} = |X_{\rm cm} - X_{gc}|/R_{200}$.

- Substructure mass fraction (f_{sub}): The dark matter mass fraction in resolved subhalos (except the primary subhalo) whose centers (the minimum gravitational potential) lie inside a sphere of radius R_{200}; i.e., $f_{\rm sub} = \Sigma_{i=1}^{N_{\rm sub}} M_{dm}^{i}/M_{200}$.

The relaxation criterion for a halo is $d_{\rm CM} < 0.07$ and $f_{\rm sub} < 0.1$ (the same as in Neto et al. [140]). This resulted in 17124 relaxed halos (hereafter sample R).

5.2.2 Method to compute c_Δ

First, we calculate c_Δ (oversendity $\Delta = 200$, 2500) for all halos within that mass range. All halos dark matter profiles are fitted for the NFW profile. Following the work of Chen et al. [27], we calculate c_Δ using the following algorithm.

1. Take equally space radial 20 bins in log-space from the halo center to r_Δ
2. for an assumed c_Δ, using the equation calculate expected M_Δ for the NFW profile for the radial bin i, (M_i^{NFW})
3. Find the c_Δ minimizing the χ^2 given by,

$$\chi^2(c) = \sum_{i=1}^{20} \frac{[M_i - M_i^{NFW}]^2}{M_i^2/N_i} \tag{5.3}$$

   where M_i and N_i are the total dark matter mass and the number of dark matter particles in the radial bin i, respectively.

$$M(<r) = M_{200} \frac{f(cr/r_{200})}{f(c)} \tag{5.4}$$

where $f(c) = \ln(1+c) - \frac{c}{1+c}$

5.2.3 Concentration - Mass relation

We compare the power law fits (i.e., $c_{200} = AM_{200}^{B}$)for all the halos in the sample and relaxed halos in Figure 5.1. In the left plot, our fit (purple line) agrees well with the ΛCDM relation (maximum deviation of 15% from ΛCDM). Following a similar process, we fit a power law for $c_{2500} - M_{2500}$ (used R_{2500} which is inferred directly using the mass profile; i.e., not using inferred r_{200}) for the same two samples; i.e., all and relaxed halos and it is shown in Figure 5.2. To our knowledge, there are no studies in the literature that have calculated the $c_{2500} - M_{2500}$ relation (Ragagnin et al. [163] has derived, but for galaxy clusters with mass $M_{200} \geq 10^{14} M_{\odot}$). For both relationships, the scatter around the median mass for a mass bin of size 0.2 dex is 0.1 and does not vary much with mass (in the range; 0.10-0.14). At least for c_{200}, this agrees well with the scatter shown in the ΛCDM relation.

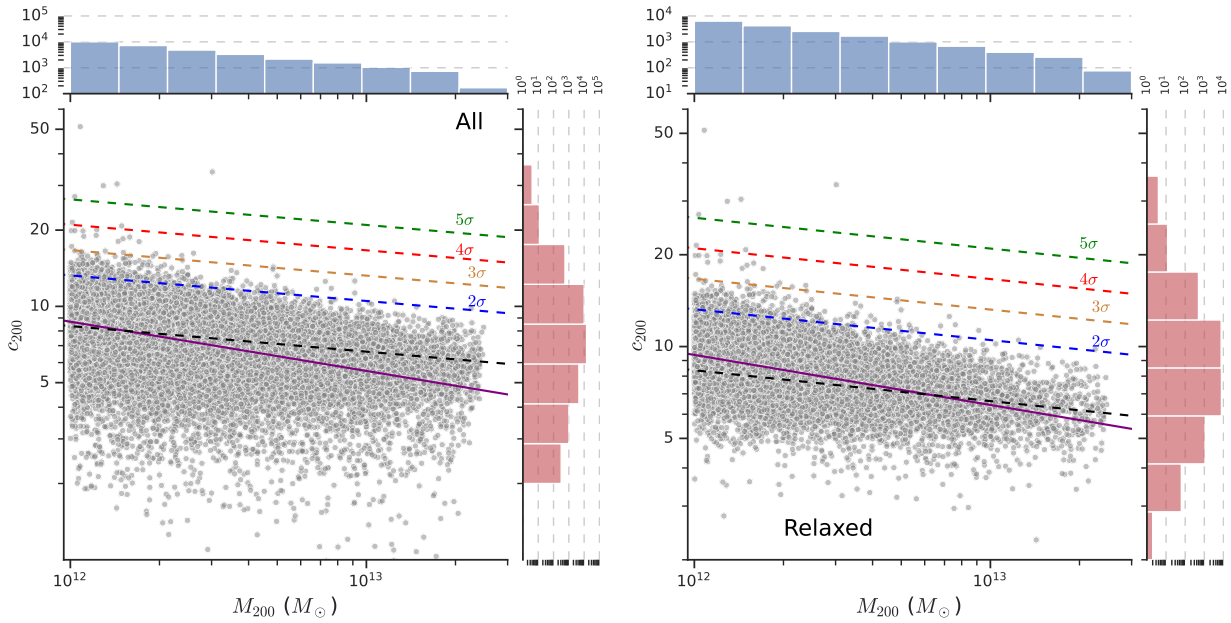

Figure 5.1: c_{200} and M_{200} for all the halos (left) and relaxed halos (right) in the TNG300. The dashed black line is the $c_{200} - M_{200}$ relation for relaxed halos adopted from Dutton et al. [54]. Each dashed line other than black indicates the positive deviation from the Dutton's relation. The number of halos in each M_{200} and c_{200} bin is displayed, respectively, by two histograms that surround each main plot.

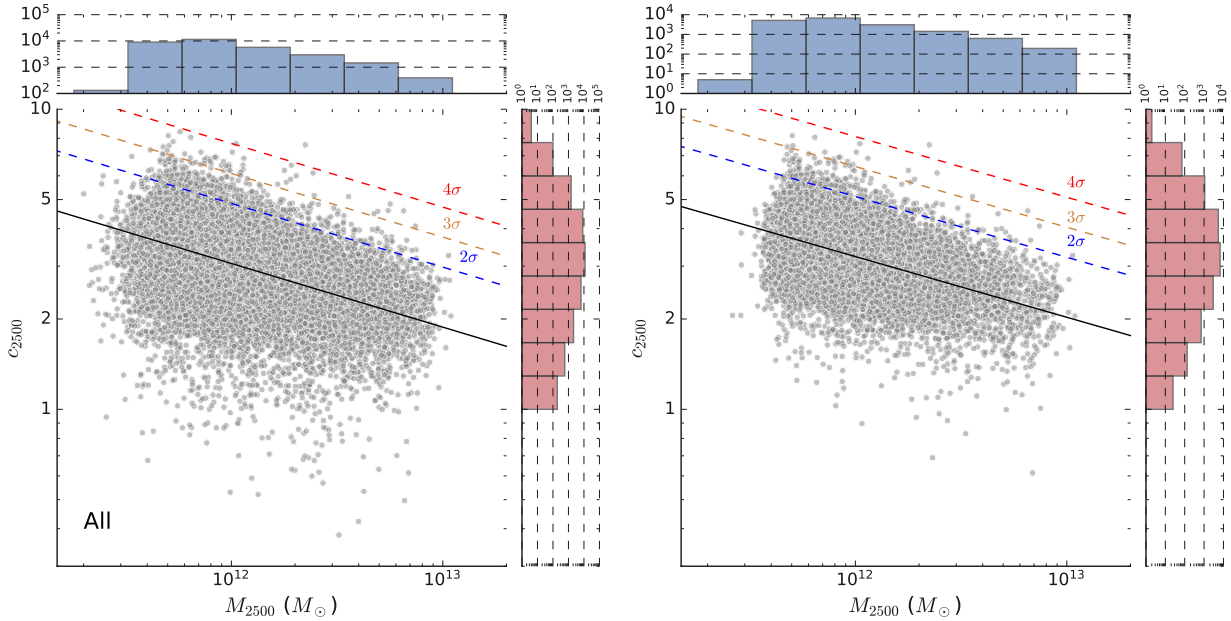

Figure 5.2: c_{2500} and M_{2500} for all the halos (left) and relaxed halos (right) in the TNG300. The black line represents the power-law fit we obtained for each sample. Each dashed line indicates the positive deviation from the $c_{2500} - M_{2500}$ relation (black line) that we obtained. The number of halos in each M_{2500} and c_{2500} bin is displayed, respectively, by two histograms that surround each main plot.

5.3 Highly concentrated dark matter halos

5.3.1 Comparison of c_{2500} with c_{200}

In this section, we select halos that are positive outliers; i.e., at least $2\sigma_{c\Delta}$ above the median ΛCDM relation. In Figure 5.3, we plot the c_{2500} in terms of the deviation from the median ΛCDM relation for the c_{200} outliers. Although there are more outliers in c_{2500} (325 halos) than in c_{200} (191 halos), c_{200} is more spread, reaching over 5σ, while c_{2500} is more concentrated in a smaller range of deviations.

Those two figures illustrate that it is not trivial to assume that if a density profile of a halo follows the NFW profile for $r < R_{2500}$, the validity of the NFW profile can be extended to the outer region. For a selected $\sigma_{c\Delta}$ less than 3, it has a significant scatter, although for c_{2500} outliers the scatter is significantly larger than for c_{200}. We present Figure 5.3 as a control plot to illustrate the scatter for halos near (within 0.005 σ_{c200}) the ΛCDM relation. It shows that there is a significant scatter in c_{2500} for halos that follows $c_{200} - M_{200}$ relation.

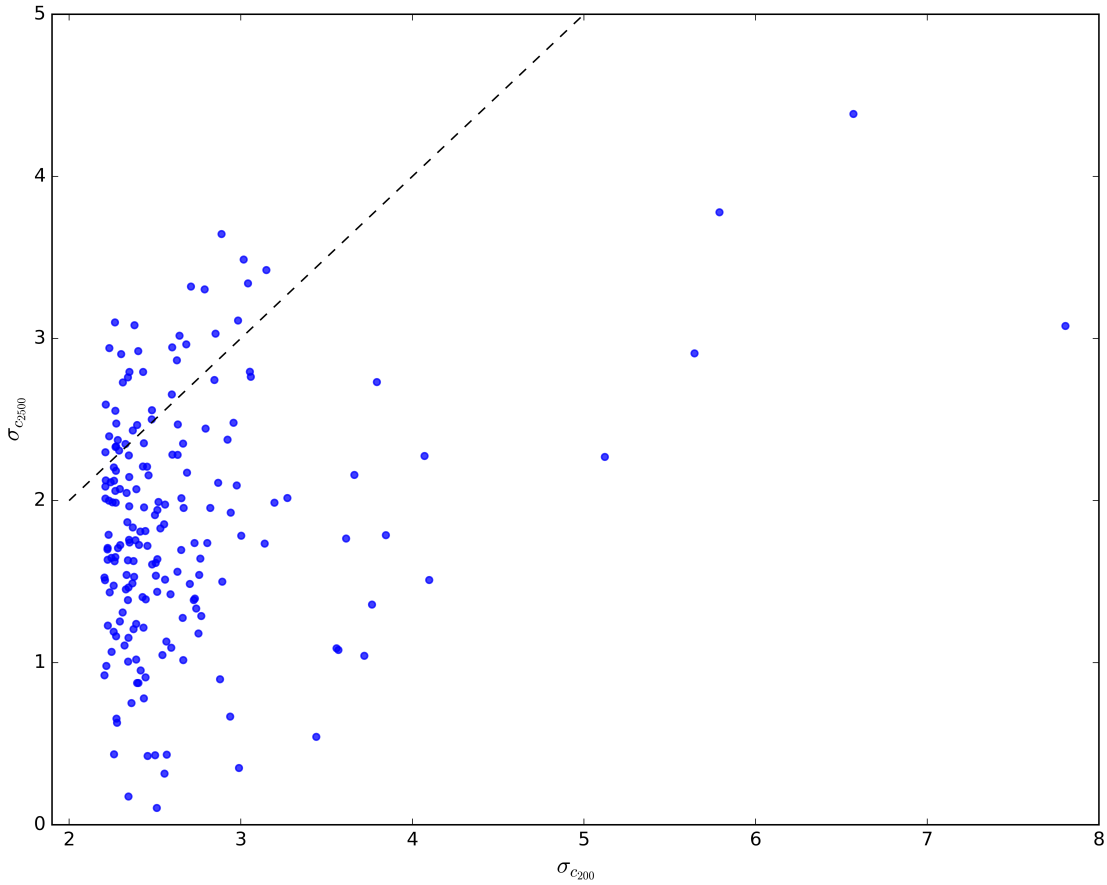

Figure 5.3: σ_{c2500} values for σ_{c200} outliers in the simulation TNG300. Black dashed line represents if the deviations in c_{200} and c_{2500} were same (i.e., $\sigma_{c200} = \sigma_{c2500}$).

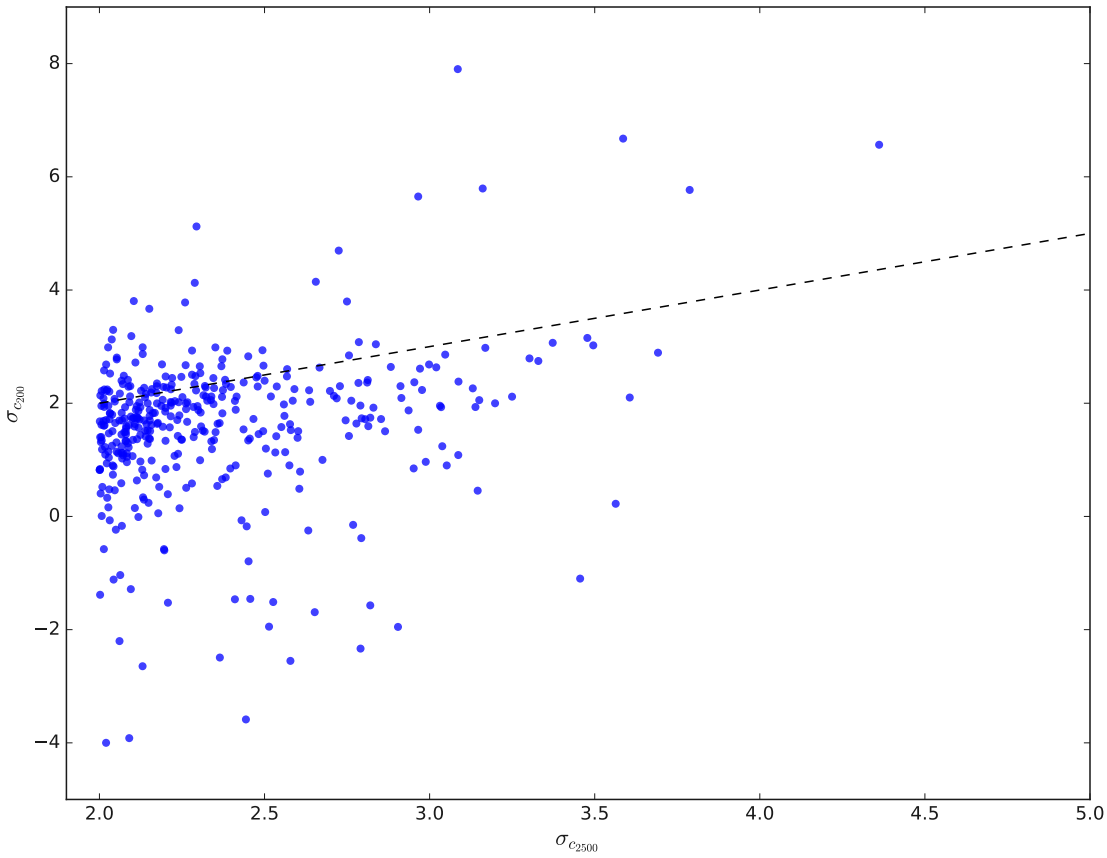

Figure 5.4: σ_{c200} values for σ_{c2500} outliers in the simulation TNG300. Black dashed line represents if the deviations in c_{200} and c_{2500} were same (i.e., $\sigma_{c200} = \sigma_{c2500}$).

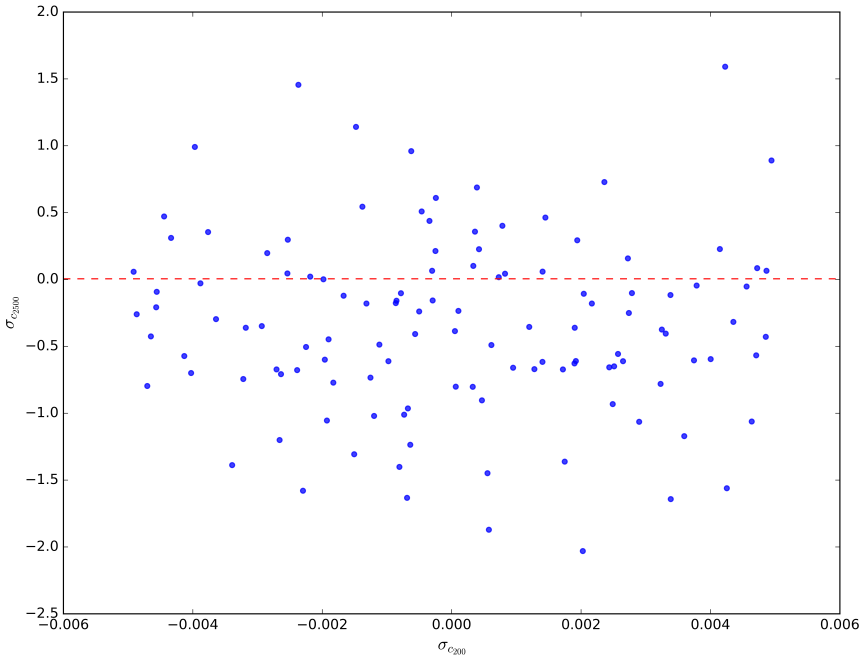

Figure 5.5: σ_{c2500} values for halos with c_{200} that follows the ΛCDM relation (within 0.005 σ_{c200}) in the simulation TNG300. Red dashed line represents $c_{2500} = 0$.

5.3.2 Evolution of Masses

We used the method used in Section 3.3.1 to analyze the evolution of dark matter and stellar mass since $z = 2$. We only considered outliers that are above $2.5\sigma_{c\Delta}$ and separated the outliers into four bins. We plot the fraction of evolution in dark matter and stellar masses for both c_{2500} and c_{200} outliers in Figure 5.2 and Figure 5.1 respectively. In both figures, halos at the highest end of the concentration range (above $3.75\sigma_{c2500}$ or $5\sigma_{c200}$) show a more constrained evolution of dark matter and stellar mass since $z = 2$. All of them show dm fractions above 1; i.e., dark matter mass has lost after $z = 2$. Only 1 of the halo shows a loss in stellar mass after $z = 2$.

The upper middle range ($3-3.5\,\sigma_{c200}$) has most of the halos exhibiting fractional dark matter mass evolution above 1 (70% of the halos in the range), while only a few halos have fractional stellar mass evolution above 1. The smallest outliers shown (e.g., between 2.5-3 σ_{c2500} and

σ_{c200}) have a very flat distribution in stellar fraction between $0 - 1.2$. The dm fraction is more concentrated at large values between $0.7 - 1.05$ though there are some that extend down to 0.3 and up to about 1.4.

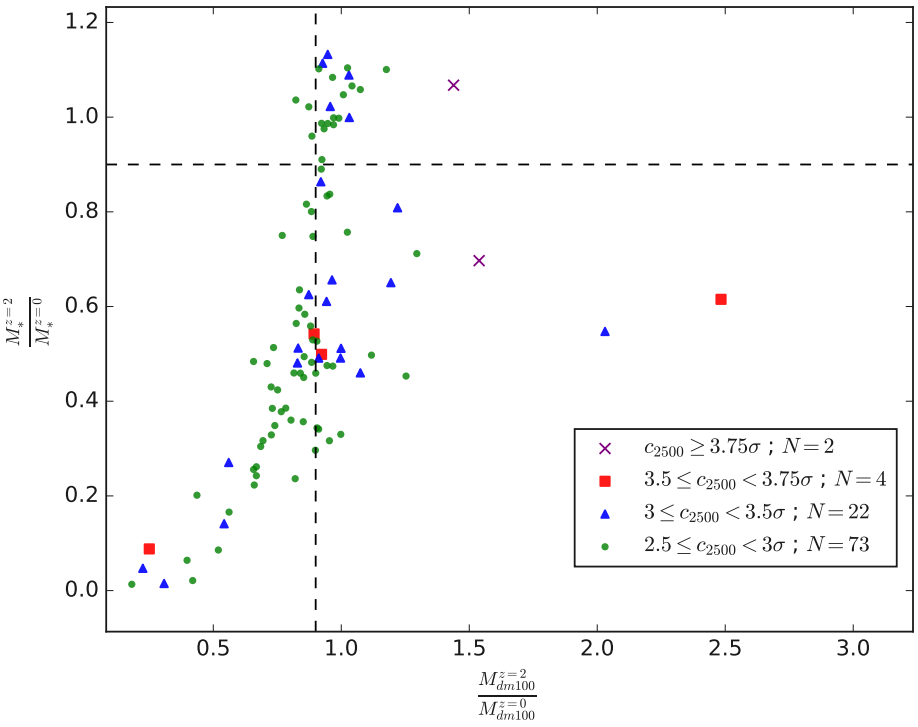

Figure 5.6: Fraction of dark matter and stellar mass evolution for outliers ($\geq 2.5\sigma_{c2500}$) in $c_{2500} - M_{2500}$ TNG300. Halos in the region at the top right corner bounded by the dashed lines, can be identified as relics according to the definition used in Section 3.3.1. N is the number of halos in each c_{2500} bin.

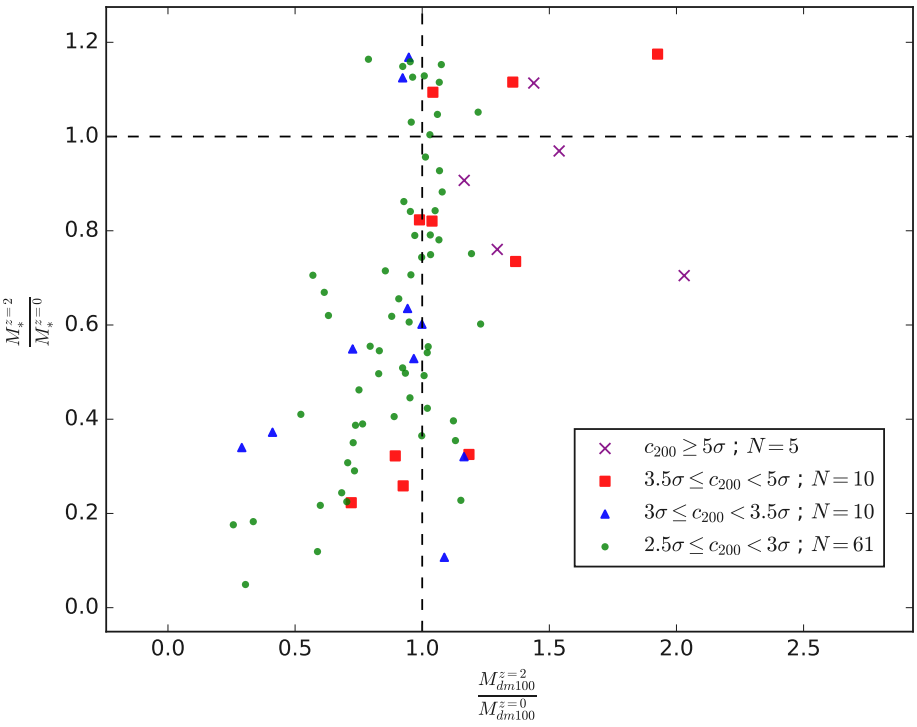

Figure 5.7: Fraction of dark matter and stellar mass evolution for outliers ($\geq 2.5\sigma_{c200}$) in $c_{200} - M_{200}$ TNG300. Halos in the region at the top right corner bounded by the dashed lines, can be identified as relics according to the definition used in Section 3.3.1. N is the number of halos in each c_{200} bin.

5.3.3 Gas Properties

First, we noticed an interesting property that the largest outliers in c_{200} (i.e., $\geq 5\sigma_{c200}$) do not show any trace of gas[1] at $z = 0$. In Figure 5.8, we plot the fraction of halos with a gas mass fraction within R_{2500} of the halo, greater than 0.001, with respect to the total number of outliers more than the appropriate value. For example, the fraction at the first red data point = (Number of outliers with gas and at least $2.5\sigma_{c200}$)/(Number of outliers with at least $2.5\sigma_{c200}$). The gas mass considered for the calculation, is within R_{2500} radius from the subhalo center. We also notice that it produces the same result for the hot gas-mass fraction. Our results suggest that high-concentration halos tend to loose mass, although a larger sample of relics is needed to quantify and confirm such a relation.

[1]Note: Gas includes both hot and cold components.

Then, we separate the gas mass into two components by the temperature (i.e., hot and cold). The temperature of a gas particle is calculated under the assumption of a perfect monoatomic gas (see APPENDIX D for the method we used to calculate the temperature). We defined hot gas as gas particles with a temperature(T) $\geq 10^6$ K. Figure 5.9 shows the hot gas mass fractions within R_{2500} from the subhalo center and halo dark matter concentration (in terms of scatter (σ_Δ) in the $c_\Delta - M_\Delta$ relation).

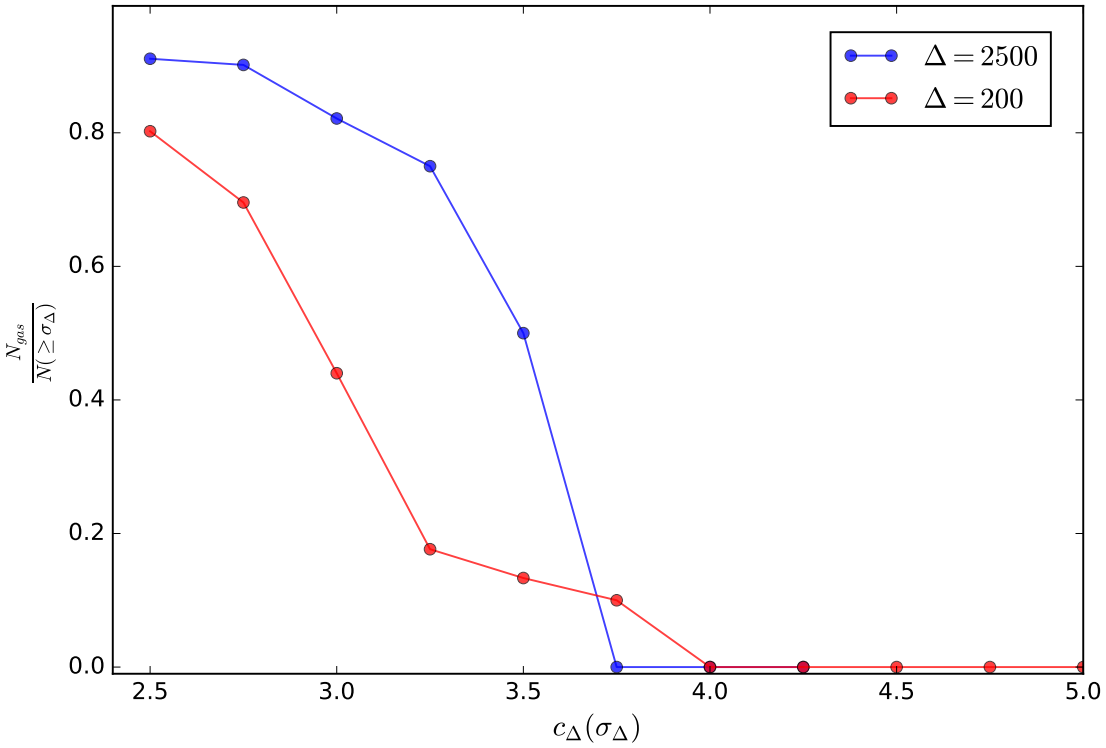

Figure 5.8: Fractions of halos (number of halos with gas/number of halos in the c_Δ interval) in TNG300, with gas (hot + cold gas) and c_Δ (for $\Delta = 200$, 2500) in terms of scatter (σ_Δ) in $c_\Delta - M_\Delta$ relation. We used $\sigma_{Delta} = 0.1$ dex for both $\Delta = 200$, 2500. The fraction is calculated respect to the sample of halos with $c_\Delta \geq \sigma_\Delta$ outliers; e.g., the fraction at the first red data point = (Number of outliers with gas and at least $2.5\,\sigma_{c200}$)/(Number of outliers with at least $2.5\,\sigma_{c200}$). All gas considered are within R_{2500} radius from the subhalo center.

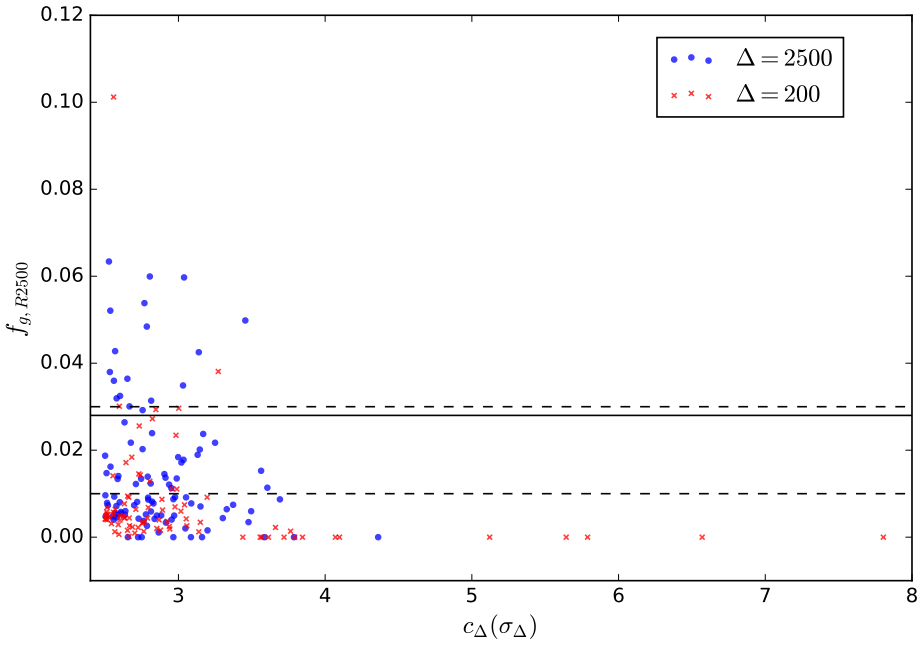

Figure 5.9: Hot gas fraction within a radius of R_{2500} and c_Δ (for $\Delta = 200, 2500$) in terms of scatter (σ_Δ) in $c_\Delta - M_\Delta$ relation. The black solid line represents the gas fraction for Mrk 1216. The dashed line are at fraction values 0.03 and 0.01 which we use to select halos with gas fractions similar to Mrk 1216, for our analysis in the following section.

5.3.4 Environmental Effects

We explore the interaction between the selected halos (outliers $\geq 2.5\sigma_{c200}$) and its neighbourhood. We define the neighborhood as the space inside a cube of size 500 kpc[1] where the halo center (subfind center) is located at the center of the cube. Then we look for any flybys or tidal stripping by looking at the growth history of each halo and if there is any subhalo (at least with a total mass of $0.1 \times M_h(z)$ where $M_h(z)$ is the total mass of the selected outlier halo at redshift z) that moves inside the neighborhood from redshifts $z = 2$ to $z = 0$.

We find an interesting property in the extreme outliers in c_{200} (i.e., $c_{200} \geq 5\sigma_{c200}$; a total of 5 halos), that all showed many flybys after $z = 0$. They all have had a subhalo at least 0.5 times massive as the outlier halo within 100 kpc from the center.

5.3.5 Mrk 1216 Analogues

After a rigorous analysis on mass profiles, growth history, and isolated growth of the concentration outliers, we select a few halos that have properties closest to the relic galaxy Mrk 1216. In Table 5.1 ,we present properties for a couple of selected outliers in c_{2500} that mimic some properties of Mrk 1216. We have included the best-fit values for σ_Δ (row 3), statistical error (1σ), and the value for the strong possibility of adiabatic contraction (AC). Even under the possibility of strong AC, Mrk 1216 is over $4\sigma_\Delta$ outlier. But with the combination of statistical error and the systematic error (i.e., adiabatic contraction), c_{2500} lowers down to $3.5\sigma_{c2500}$ outlier, which is in the range of outliers we found in the TNG300 that are similar to Mrk 1216.

We consider subhalo 1225888 as the closest analogue for Mrk 1216 as it matches the gas and stellar mass closely to Mrk 1216. Also, it does not show a large stellar mass and dark matter

[1]The selection of 500 kpc is somewhat arbitrary. A larger value (e.g., 1 Mpc) can be chosen but it will increase the computational time significantly.

growth after $z = 2$.

Table 5.1: Properties for Mrk 1216 analogues

Id	$\sigma_{2500}(\sigma_{200})$	M_* $(10^{10} M_\odot)$	M_{200} $(10^{12} M_\odot)$	f_{gR2500}	$\frac{Mdm_{z=2}}{Mdm_{z=0}}$	$\frac{M*_{z=2}}{M*_{z=0}}$	Age (Gyr)
1754066	3.61 (2.1)	5.3	1.32	0.086	0.89	0.54	9.5
1225888	3.02 (2.63)	10.39	7.27	0.017	1.22	0.81	11.8
Mrk 1216	5.7 (5.8)	13	1.32[a]	0.028	-	-	12.8
Stat. error	5.17 (5.2)						
Strong AC	4.45 (4.5)						

[a] Enclosed total mass (BH+stars+gas+DM) [22].

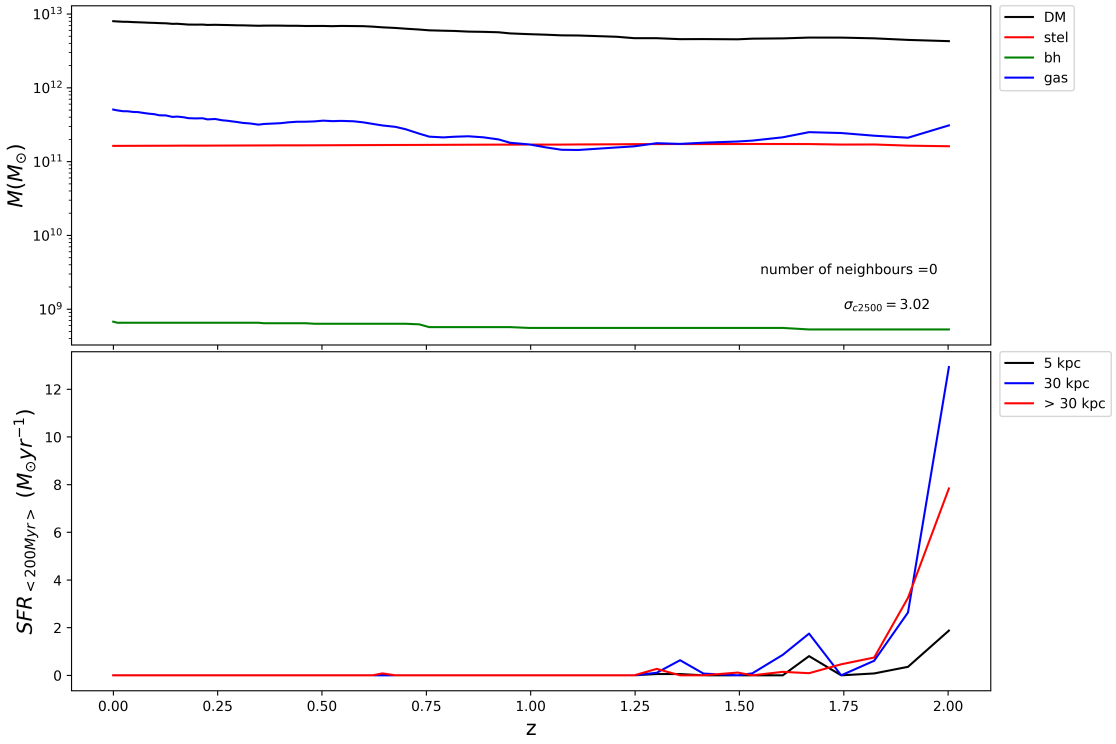

Figure 5.10: Growth history and star formation rates (SFR) history for the subhalo 1225888. (Bottom panel) The values for star formation rates are publicly available [51, 156]. SFR is calculated by taking the time-averaged stellar mass (within a given aperture) that was created within 200 Myr from the considered snapshots. Each color in the bottom panel indicates the aperture used to measure the stellar masses for the SFR calculation. (Top panel) Number of neighbors indicates the total number of neighbors the outlier halo has had since $z = 2$. The mass indicated by different colors represent dark matter (dm), stellar mass (stel), black hole (bh), gas respectively. All the masses include all the particles that are identified by the halo finder.

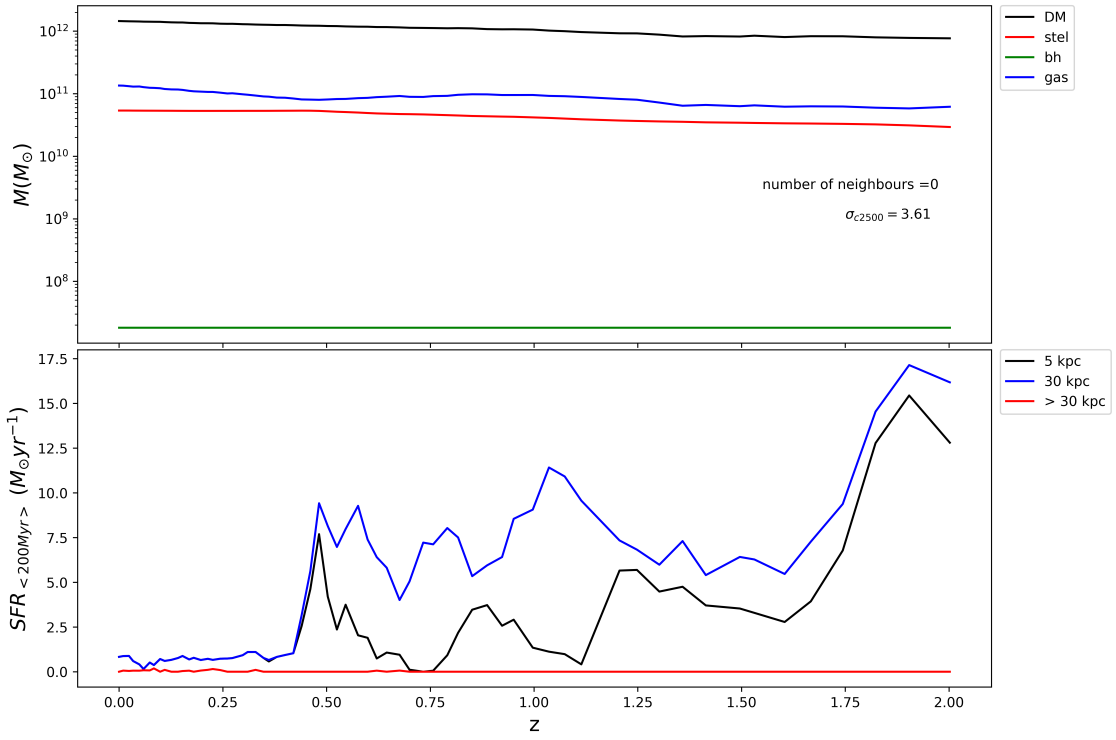

Figure 5.11: Growth history and star formation history for the subhalo 1754066. (bottom panel) The values for star formation rates are publicly available [51, 156]. SFR is calculated by taking the time averaged stellar mass (within a given aperture) that was created within 200 Myr from the considered snapshots. Each color in the bottom panel indicates the aperture used to measure the stellar masses for the SFR calculation. (top panel) Number of neighbors indicates the total number of neighbours the outlier halo had since $z = 2$. The mass indicated by different colors represent dark matter (dm), stellar mass (stel), black hole (bh), gas respectively. All the masses includes all the particles that are identified by the halo finder.

5.4 Discussion

This chapter demonstrates the dark matter concentration and mass relation for primary subhalos in TNG300 simulation. For the power law fit, we considered relaxed halos, which were determined by the definition explained in Section 5.2.2. We did not impose the third criterion (i.e., virial ratio) for relaxed halos that has been used in Neto et al. [140], because it was mentioned in the work by Bhattacharya et al. [15], that it will not significantly change the relaxed halo sample. In the literaure in some occations, mean (e.g., Maccio et al. [108]) or median $c_{200} - M_{200}$ has been derived (e.g., Bhattacharya et al.[15]) which are in consistent with the Dutton et al. result.

We assumed a NFW profile for calculating c_Δ but not all the halos follow the NFW profile. Einasto profile [55] is an alternative which has shown a steeper concentration - mass relation [53]. Although Einasto profile is more robust (more degrees of freedom) than NFW, it introduces numerical complications which make it computationally expensive.

As displayed in Figure 5.7 and Figure 5.6, most of the high c_Δ seem to be the result of flybys. In a flyby, two galaxies come really closer (within ~ 100 kpc for these halos) and their dark matter halos (since they reach out to larger radial distances) interact with each other. As shown in APPENDIX C, such flybys strip off the outer DM (and gas) leaving a steeper (i.e., more concentrated) profile.

There are a variety of methods to compute c_Δ including density profile fit (e.g., Dutton et al. [53]), using the maximum circular velocity (V_{max}) of the halo (e.g., Klypin et al. [87]). The V_{max} and density profile methods produce similar concentrations except for higher redshifts and especially higher masses [160, 53], where the V_{max} method produces higher concentrations. It is expected because any deviations from a NFW profile are expected to cause the scatter in Vmax to increase [53]. We compare only with the V_{max} method, and the results are consistent.

There are only 5 halos with halo concentrations above $5\,\sigma$ of the ΛCDM relation. A low number such as this is expected since there are only $\sim$ 30000 halos in the selected mass range. To have a more rigorous analysis on extremely high concentrated halos, a larger halo sample is needed; i.e., hydrodynamical simulation with a larger box.

5.5 Conclusions

We have explored the dark matter halo concentration - mass relationship for halos within the mass (M_{200}) range $10^{12}M_{\odot} - 3 \times 10^{13}M_{\odot}$, and it is consistent with the median ΛCDM (relationship in Dutton et al. [53]). To our knowledge, for the first time we have presented the median $c_{2500} - M_{2500}$ relationship. Both c_{200} and c_{2500} show a log-normal distribution for a given mass and have the same scatter ($\log_{c\Delta} = 0.1$). Our results indicated that it is not trivial to assume that if a density profile of a halo follows the NFW profile for $r < R_{2500}$, the validity of the NFW profile can be extended to the outer region (i.e., R_{200}).

By calculating gas fraction for the halo dark matter concentration outliers of concentration - mass relation, we have displayed that as concentration gets higher in the outliers sample fewer halos show gas. Extremely high-concentrated halos show no trace of gas at redshift 0. Additionally, they show many interactions with other subhalos since redshift 2. Taken together, these observations suggest that the tidal effects of flybys and gas stripping may produce extremely concentrated halos, although we believe that a larger sample is needed to confirm this hypothesis. These halos might be classified as relics following the physically motivated relicness definition (as in Section 3.3.1), but they all show signs of tidal effects from galaxy flybys, and therefore, they have not gone through passive, isolated evolution.

After going through mass assembly history and interaction with neighboring halos, we have shown that hot gas fractions similar to Mrk 1216, are to be found for less extreme outliers.

Chapter 6

Conclusions

6.1 Summary

This thesis has demonstrated the potential of cosmological simulations to investigate and to provide fresh insights into the theory of galaxy formation and search for massive relic galaxies. First, we derive the galaxy mass-size relation for early-type galaxies (ETGs) and compare it with observations. Then, we explore and compare two distinct approaches to searching for relic galaxies in the simulation TNG300. Finally, to our understanding, for the first time, we investigate halos of galaxies on the massive galaxy scale, which are positive outliers from the ΛCDM dark matter halo concentration- mass relationship. In closing this section, we summarize the key findings as follows.

- In Chapter 2, we derived the median mass-size relationship at two redshifts $z = 0$ and $z = 2$ using multiple estimators for size including the half stellar mass radius and the half light radius, for ETGs with M_{200} between $10^{12} M_{\odot}$ and $5 \times 10^{13} M_{\odot}$. Our derived median mass-size relation for $z = 0$, which adopted the half-light radius estimated for the dust corrected brightness profile, is in good agreement with observations (within

10% of SDSS predictions and 15% of Van14). By showing the existence of massive ETGs that show a difference over 15% between dust-corrected and raw half-light radius, we corroborate the importance of employing dust effects on star light.

- Contrary to the popular application of overdensity-based radius, we showed an aperture of 100 kpc from the halo center is best suited to quantify the passiveness of dark matter mass growth of halos. We have shown that the relicness defined physically corroborates the definition based on compactness that has been used in observations. Although we have presented some evidence that the relicness of ETGs defined by physical criteria is positively correlated with dark matter halo concentration (c_{200}), we did not find conclusive evidence to suggest that the concentration of halos with M_{200} above $10^{13}M_{\odot}$, show a higher concentration than the predicted value from the ΛCDM $c_{200} - M_{200}$ relation.

- Having a number of ways of defining the compactness of massive relic galaxies in the literature, we have shown that the definition adopted by Trujillo et al. [206] is marginally better than the other two definitions we compared with (the median of the fraction of stellar mass at $z = 2$ to $z = 0$ is 5% larger than Van [213] and 20% larger than Damanjov [39]). Interestingly, we have found that the massive relics ($M_* \geq 10^{11}M_{\odot}$) selected from Trujillo's definition show a higher dark matter halo concentration especially for low mass halos ($M_{200} < 10^{13}M_{\odot}$). However, we did not find any extreme outliers of concentration similar to Mrk 1216 in the relic sample.

- The derived $c_{200} - M_{200}$ relationship for halos with mass $10^{12}M_{\odot} \leq M_{200} \leq 5 \times 10^{13}M_{\odot}$ is in good agreement with the relation derived by Dutton et al. [53]. To our knowledge, for the first time we have presented the median $c_{2500} - M_{2500}$ relationship for the galaxies in a simulation (Ragagnin et al. [163] has derived, but for galaxy clusters with mass $M_{200} \geq 10^{14}M_{\odot}$). We have shown that positive outliers in c_{2500} are not necessarily outliers in c_{200} implying that halo dark matter profiles may deviate from the NFW

profile at larger radii. Extremely high-concentrated halos did not show any gas at redshift 0. Furthermore, they showed many interactions with other subhalos after redshift 2. They also showed growth in dark matter mass within 100 kpc from the center after $z = 2$. Combining these observations we have concluded that the extremely high concentration halos in TNG300 have been affected by the tidal effects from flybys, although we believe that a larger sample is needed to confirm this hypothesis as we have only found a handful of high positive outliers in TNG300. In addition, we have shown that some of these halos might be classified as relics following the physically motivated relicness definition (as in Section 3.3.1), but they all show signs of tidal effects from galaxy flybys; therefore, they have not gone through passive, isolated evolution.

- We have explored the dark matter halo concentration - mass relationship for halos within the mass (M_{200}) range $10^{12} M_{\odot} - 3 \times 10^{13} M_{\odot}$, and it is consistent with the median ΛCDM (relationship in Dutton et al. [53]). Both c_{200} and c_{2500} show a log-normal distribution for a given mass and have the same scatter ($\log_{c\Delta} = 0.1$). Our results indicated that it is not trivial to assume that if a density profile of a halo follows the NFW profile for $r < R_{2500}$, the validity of the NFW profile can be extended to the outer region (i.e., R_{200}). By calculating gas fraction for the halo dark matter concentration outliers of concentration - mass relation, we have displayed that as concentration gets higher in the outliers sample fewer halos show gas. Extremely high-concentrated halos show no trace of gas at redshift 0. Additionally, they show many interactions with other subhalos since redshift 2. Taken together, these observations suggest that the tidal effects of flybys and gas stripping may produce extremely concentrated halos, although we believe that a larger sample is needed to confirm this hypothesis.

6.2 Future Prospects

This thesis has provided an initial exploration into areas that have either been scarcely investigated or completely overlooked. To our knowledge, no one has studied massive relic galaxies in cosmological simulations that are isolated similarly to the relic compact galaxy Mrk 1216. Since the few relics we found do not have gas, we have to ask "Do any relic galaxies in simulations have a particularly high concentration of dark matter and gas fraction, such as Mrk 1216?" As shown in Figure 5.8, the number of galaxies of high concentration with gas tends to drop with concentration. Clearly, a detailed study of a larger sample of halos would provide better statistics and test this claim regarding the loss of gas in high concentration galaxies. Do all extremely high concentration halo show tidal effects in their outer shells?

As computational power advances, simulations larger than TNG300 have been developed with a level of resolution comparable to that of TNG300. One of the most promising simulations that has finished its run last year is the simulation "MilleniumTNG" [71]. It is almost 15 times larger than TNG300 in volume. The data will be accessible to the scientific community in 2024. In addition, there is already publicly available hydrodynamical simulation Magneticum Pathfinder Box 2b/hr that has a box size of $\simeq 1000\,\mathrm{Mpc}$. These simulations will provide a great test ground for the search for halos with extremely high concentrations and will answer those questions.

Another path that needed to be explored is the effect of including satellite subhalos in the sample. This may make the sample large enough to produce more extremely high concentration halos, but it may introduce bias effects by having more tidally affected subhalos (Rodriguez et al. [167] showed that satellites in TNG300 are roughly 30% smaller than primary subhalos due mainly to tidal stripping).

The effect of local environment on the halo concentration and mass - size relationship need to be explored. We have explored the environmental effects on high concentration halos in

Section 5.3.5 where we defined the environment as a cubic space with a size of 500 kpc. This definition is somewhat arbitrary and there are numerous ways (see Muldrew et al. [129] for a review) to define the environment including, the distant to the nth nearest neighbor (n = 3, 4, 5..) and aperture based similar to we adapted (e.g., a sphere with a radius of 1 Mpc).

Another important property of relics that we have not investigated is their black hole masses. One interesting property of the local massive ETGs in the work by Yıldırım et al. [226] is that a couple of galaxies (e.g., NGC 1277, Mrk 1216) that are believed to be relics have extremely massive black holes. Although the black hole masses of these ETGs are consistent with the black hole mass - stellar dispersion ($M_{\rm BH}-\sigma_*$ relation, they are overmassive relative to the black hole mass - bulge luminosity ($M_{\rm BH}-L_{\rm bul}$) and black hole mass - bulge mass ($M_{\rm BH}-M_{\rm bul}$) scaling relations [31]. Do the relic galaxies or dark matter halo concentration outliers show a similar trend? A direct evaluation would be difficult as it has shown by Li et al. [100] that hydrodynamical simulations similar to TNG300 (e.g., TNG100) produce a $M_{\rm BH}-\sigma_*$ with a noticeable deviation from the observed $M_{\rm BH}-\sigma_*$.

As we have only employed a nonparammetric method to infer sizes, there are other methods that are worth exploring including Sersic fitting. To our knowledge, no one has studied how the multicomponent Sersic fits would affect the mass-size relation in hydrodynamical simulations. For example, although ETGs are less structured compared to spiral galaxies, Huang et al. [77] proposed that local ellipticals generally contain three structural components; therefore, the majority of ellipticals are not well described by a single-component Sersic fit but by a three-component Sersic fit. Is there a better suited radius to investigate the formation of ETGs other than a half-light radius fitted from a single component Sersic profile or nonparametric method?".

I hope these questions will find solutions with the upcoming and existing cosmological simulations.

Bibliography

[1] N. J. Adams, R. A. A. Bowler, M. J. Jarvis, B. Häußler, and C. D. P. Lagos. Evolution of the galaxy stellar mass function: evidence for an increasing M* from z = 2 to the present day. *Monthly Notices of the Royal Astronomical Society*, 506(4):4933–4951, Oct. 2021.

[2] Astropy Collaboration, A. M. Price-Whelan, P. L. Lim, N. Earl, N. Starkman, L. Bradley, D. L. Shupe, A. A. Patil, L. Corrales, C. E. Brasseur, M. N"othe, A. Donath, E. Tollerud, B. M. Morris, A. Ginsburg, E. Vaher, B. A. Weaver, J. Tocknell, W. Jamieson, M. H. van Kerkwijk, T. P. Robitaille, B. Merry, M. Bachetti, H. M. G"unther, T. L. Aldcroft, J. A. Alvarado-Montes, A. M. Archibald, A. B'odi, S. Bapat, G. Barentsen, J. Baz'an, M. Biswas, M. Boquien, D. J. Burke, D. Cara, M. Cara, K. E. Conroy, S. Conseil, M. W. Craig, R. M. Cross, K. L. Cruz, F. D'Eugenio, N. Dencheva, H. A. R. Devillepoix, J. P. Dietrich, A. D. Eigenbrot, T. Erben, L. Ferreira, D. Foreman-Mackey, R. Fox, N. Freij, S. Garg, R. Geda, L. Glattly, Y. Gondhalekar, K. D. Gordon, D. Grant, P. Greenfield, A. M. Groener, S. Guest, S. Gurovich, R. Handberg, A. Hart, Z. Hatfield-Dodds, D. Homeier, G. Hosseinzadeh, T. Jenness, C. K. Jones, P. Joseph, J. B. Kalmbach, E. Karamehmetoglu, M. Kaluszy'nski, M. S. P. Kelley, N. Kern, W. E. Kerzendorf, E. W. Koch, S. Kulumani, A. Lee, C. Ly, Z. Ma, C. MacBride, J. M. Maljaars, D. Muna, N. A. Murphy, H. Norman, R. O'Steen, K. A. Oman, C. Pacifici, S. Pascual, J. Pascual-Granado, R. R. Patil, G. I. Perren, T. E. Pickering, T. Rastogi, B. R. Roulston, D. F. Ryan, E. S. Rykoff, J. Sabater, P. Sakurikar, J. Salgado, A. Sanghi, N. Saunders, V. Savchenko, L. Schwardt, M. Seifert-Eckert, A. Y. Shih, A. S. Jain, G. Shukla, J. Sick, C. Simpson, S. Singanamalla, L. P. Singer, J. Singhal, M. Sinha, B. M. SipHocz, L. R. Spitler, D. Stansby, O. Streicher, J. Sumak, J. D. Swinbank, D. S. Taranu, N. Tewary, G. R. Tremblay, M. d. Val-Borro, S. J. Van Kooten, Z. Vasovi'c, S. Verma, J. V. de Miranda Cardoso, P. K. G. Williams, T. J. Wilson, B. Winkel, W. M. Wood-Vasey, R. Xue, P. Yoachim, C. Zhang, A. Zonca, and Astropy Project Contributors. The Astropy Project: Sustaining and Growing a Community-oriented Open-source Project and the Latest Major Release (v5.0) of the Core Package. *The Astrophysical Journal*, 935(2):167, Aug. 2022.

[3] Astropy Collaboration, A. M. Price-Whelan, B. M. Sipőcz, H. M. Günther, P. L. Lim, S. M. Crawford, S. Conseil, D. L. Shupe, M. W. Craig, N. Dencheva, A. Ginsburg, J. T. Vand erPlas, L. D. Bradley, D. Pérez-Suárez, M. de Val-Borro, T. L. Aldcroft, K. L. Cruz, T. P. Robitaille, E. J. Tollerud, C. Ardelean, T. Babej, Y. P. Bach,

M. Bachetti, A. V. Bakanov, S. P. Bamford, G. Barentsen, P. Barmby, A. Baumbach, K. L. Berry, F. Biscani, M. Boquien, K. A. Bostroem, L. G. Bouma, G. B. Brammer, E. M. Bray, H. Breytenbach, H. Buddelmeijer, D. J. Burke, G. Calderone, J. L. Cano Rodríguez, M. Cara, J. V. M. Cardoso, S. Cheedella, Y. Copin, L. Corrales, D. Crichton, D. D'Avella, C. Deil, É. Depagne, J. P. Dietrich, A. Donath, M. Droettboom, N. Earl, T. Erben, S. Fabbro, L. A. Ferreira, T. Finethy, R. T. Fox, L. H. Garrison, S. L. J. Gibbons, D. A. Goldstein, R. Gommers, J. P. Greco, P. Greenfield, A. M. Groener, F. Grollier, A. Hagen, P. Hirst, D. Homeier, A. J. Horton, G. Hosseinzadeh, L. Hu, J. S. Hunkeler, Ž. Ivezić, A. Jain, T. Jenness, G. Kanarek, S. Kendrew, N. S. Kern, W. E. Kerzendorf, A. Khvalko, J. King, D. Kirkby, A. M. Kulkarni, A. Kumar, A. Lee, D. Lenz, S. P. Littlefair, Z. Ma, D. M. Macleod, M. Mastropietro, C. McCully, S. Montagnac, B. M. Morris, M. Mueller, S. J. Mumford, D. Muna, N. A. Murphy, S. Nelson, G. H. Nguyen, J. P. Ninan, M. Nöthe, S. Ogaz, S. Oh, J. K. Parejko, N. Parley, S. Pascual, R. Patil, A. A. Patil, A. L. Plunkett, J. X. Prochaska, T. Rastogi, V. Reddy Janga, J. Sabater, P. Sakurikar, M. Seifert, L. E. Sherbert, H. Sherwood-Taylor, A. Y. Shih, J. Sick, M. T. Silbiger, S. Singanamalla, L. P. Singer, P. H. Sladen, K. A. Sooley, S. Sornarajah, O. Streicher, P. Teuben, S. W. Thomas, G. R. Tremblay, J. E. H. Turner, V. Terrón, M. H. van Kerkwijk, A. de la Vega, L. L. Watkins, B. A. Weaver, J. B. Whitmore, J. Woillez, V. Zabalza, and Astropy Contributors. The Astropy Project: Building an Open-science Project and Status of the v2.0 Core Package. *The Astronomical Journal*, 156(3):123, Sept. 2018.

[4] Astropy Collaboration, T. P. Robitaille, E. J. Tollerud, P. Greenfield, M. Droettboom, E. Bray, T. Aldcroft, M. Davis, A. Ginsburg, A. M. Price-Whelan, W. E. Kerzendorf, A. Conley, N. Crighton, K. Barbary, D. Muna, H. Ferguson, F. Grollier, M. M. Parikh, P. H. Nair, H. M. Unther, C. Deil, J. Woillez, S. Conseil, R. Kramer, J. E. H. Turner, L. Singer, R. Fox, B. A. Weaver, V. Zabalza, Z. I. Edwards, K. Azalee Bostroem, D. J. Burke, A. R. Casey, S. M. Crawford, N. Dencheva, J. Ely, T. Jenness, K. Labrie, P. L. Lim, F. Pierfederici, A. Pontzen, A. Ptak, B. Refsdal, M. Servillat, and O. Streicher. Astropy: A community Python package for astronomy. *Astronomy & Astrophysics*, 558:A33, Oct. 2013.

[5] I. K. Baldry, T. Sullivan, R. Rani, and S. Turner. Compact galaxies and the size–mass galaxy distribution from a colour-selected sample at $0.04 \leq z \leq 0.15$ supplemented by ugrizYJHK photometric redshifts. *Monthly Notices of the Royal Astronomical Society*, 500(2):1557–1574, 10 2020.

[6] J. E. Barnes. Encounters of Disk/Halo Galaxies. *The Astrophysical Journal*, 331:699, Aug. 1988.

[7] R. Bassett, C. Papovich, J. M. Lotz, E. F. Bell, S. L. Finkelstein, J. A. Newman, K.-V. Tran, O. Almaini, C. Lani, M. Cooper, D. Croton, A. Dekel, H. C. Ferguson, D. D. Kocevski, A. M. Koekemoer, D. C. Koo, E. J. McGrath, D. H. McIntosh, and R. Wechsler. CANDELS Observations of the Environmental Dependence of the Color-Mass-Morphology Relation at $z = 1.6$. *The Astrophysical Journal*, 770(1):58, June 2013.

[8] J. Bédorf and S. Portegies Zwart. The effect of many minor mergers on the size growth of compact quiescent galaxies. *Monthly Notices of the Royal Astronomical Society*, 431(1):767–780, May 2013.

[9] P. Behroozi, A. Knebe, F. R. Pearce, P. Elahi, J. Han, H. Lux, Y.-Y. Mao, S. I. Muldrew, D. Potter, and C. Srisawat. Major mergers going Notts: challenges for modern halo finders. *Monthly Notices of the Royal Astronomical Society*, 454(3):3020–3029, Dec. 2015.

[10] A. J. Benson. Galaxy formation theory. *Physics Reports*, 495(2-3):33–86, Oct. 2010.

[11] A. J. Benson, F. R. Pearce, C. S. Frenk, C. M. Baugh, and A. Jenkins. A comparison of semi-analytic and smoothed particle hydrodynamics galaxy formation. *Monthly Notices of the Royal Astronomical Society*, 320(2):261–280, Jan. 2001.

[12] M. Bernardi, R. K. Sheth, H. Domínguez Sánchez, B. Margalef-Bentabol, D. Bizyaev, and R. R. Lane. The half-mass radius of MaNGA galaxies: effect of IMF gradients. *Monthly Notices of the Royal Astronomical Society*, 518(3):3494–3508, Jan. 2023.

[13] M. Bernardi, R. K. Sheth, J. L. Fischer, A. Meert, K. H. Chae, H. Dominguez-Sanchez, M. Huertas-Company, F. Shankar, and V. Vikram. Stellar mass functions and implications for a variable IMF. *Monthly Notices of the Royal Astronomical Society*, 475(1):757–771, Mar. 2018.

[14] R. Bezanson, P. G. van Dokkum, T. Tal, D. Marchesini, M. Kriek, M. Franx, and P. Coppi. The Relation Between Compact, Quiescent High-redshift Galaxies and Massive Nearby Elliptical Galaxies: Evidence for Hierarchical, Inside-Out Growth. *The Astrophysical Journal*, 697(2):1290–1298, June 2009.

[15] S. Bhattacharya, S. Habib, K. Heitmann, and A. Vikhlinin. Dark Matter Halo Profiles of Massive Clusters: Theory versus Observations. *The Astrophysical Journal*, 766(1):32, Mar. 2013.

[16] J. Binney and S. Tremaine. *Galactic dynamics*. 1987.

[17] F. Buitrago, I. Ferreras, L. S. Kelvin, I. K. Baldry, L. Davies, J. Angthopo, S. Khochfar, A. M. Hopkins, S. P. Driver, S. Brough, J. Sabater, C. J. Conselice, J. Liske, B. W. Holwerda, M. N. Bremer, S. Phillipps, Á. R. López-Sánchez, and A. W. Graham. Galaxy and Mass Assembly (GAMA): Accurate number densities and environments of massive ultra-compact galaxies at $0.02 < z < 0.3$. *Astronomy & Astrophysics*, 619:A137, Nov. 2018.

[18] F. Buitrago, I. Trujillo, C. J. Conselice, R. J. Bouwens, M. Dickinson, and H. Yan. Size Evolution of the Most Massive Galaxies at $1.7 < z < 3$ from GOODS NICMOS Survey Imaging. *The Astrophysical Journal Letters*, 687(2):L61, Nov. 2008.

[19] J. S. Bullock, T. S. Kolatt, Y. Sigad, R. S. Somerville, A. V. Kravtsov, A. A. Klypin, J. R. Primack, and A. Dekel. Profiles of dark haloes: evolution, scatter and environment. *Monthly Notices of the Royal Astronomical Society*, 321(3):559–575, Mar. 2001.

[20] D. A. Buote. The Unusually High Halo Concentration of the Fossil Group NGC 6482: Evidence for Weak Adiabatic Contraction. *The Astrophysical Journal*, 834(2):164, Jan. 2017.

[21] D. A. Buote and A. J. Barth. The extremely high dark matter halo concentration of the relic compact elliptical galaxy mrk 1216. *The Astrophysical Journal*, 877(2):91, may 2019.

[22] D. A. Buote and A. J. Barth. The Extremely High Dark Matter Halo Concentration of the Relic Compact Elliptical Galaxy Mrk 1216. *The Astrophysical Journal*, 877(2):91, June 2019.

[23] P. Capak, R. G. Abraham, R. S. Ellis, B. Mobasher, N. Scoville, K. Sheth, and A. Koekemoer. The effects of environment on morphological evolution at 0 lt; z lt; 1.2 in the cosmos survey*. *The Astrophysical Journal Supplement Series*, 172(1):284, sep 2007.

[24] A. Cattaneo, G. A. Mamon, K. Warnick, and A. Knebe. How do galaxies acquire their mass? *Astronomy & Astrophysics*, 533:A5, Sept. 2011.

[25] M. Cebrián and I. Trujillo. The effect of the environment on the stellar mass-size relationship for present-day galaxies. *Monthly Notices of the Royal Astronomical Society*, 444(1):682–699, Oct. 2014.

[26] G. Chabrier. Galactic Stellar and Substellar Initial Mass Function. *Publications of the Astronomical Society of the Pacific*, 115(809):763–795, July 2003.

[27] Y. Chen, H. J. Mo, C. Li, H. Wang, X. Yang, Y. Zhang, and K. Wang. Relating the Structure of Dark Matter Halos to Their Assembly and Environment. *The Astrophysical Journal*, 899(1):81, Aug. 2020.

[28] A. Cimatti, P. Cassata, L. Pozzetti, J. Kurk, M. Mignoli, A. Renzini, E. Daddi, M. Bolzonella, M. Brusa, G. Rodighiero, M. Dickinson, A. Franceschini, G. Zamorani, S. Berta, P. Rosati, and C. Halliday. GMASS ultradeep spectroscopy of galaxies at z ~2. II. Superdense passive galaxies: how did they form and evolve? *Astronomy & Astrophysics*, 482(1):21–42, Apr. 2008.

[29] A. Cimatti, F. Fraternali, and C. Nipoti. Introduction to Galaxy Formation and Evolution. From Primordial Gas to Present-Day Galaxies. *arXiv e-prints*, page arXiv:1912.06216, Dec. 2019.

[30] L. Ciotti and G. Bertin. Analytical properties of the $R^{1/m}$ law. *Astronomy & Astrophysics*, 352:447–451, Dec. 1999.

[31] J. H. Cohn, J. L. Walsh, B. D. Boizelle, A. J. Barth, K. Gebhardt, K. Gültekin, A. Yıldırım, D. A. Buote, J. Darling, A. J. Baker, L. C. Ho, and K. M. Kabasares. An ALMA Gas-dynamical Mass Measurement of the Supermassive Black Hole in the Local Compact Galaxy UGC 2698. *The Astrophysical Journal*, 919(2):77, Oct. 2021.

[32] S. Cole and C. Lacey. The structure of dark matter haloes in hierarchical clustering models. *Monthly Notices of the Royal Astronomical Society*, 281:716, July 1996.

[33] C. Conroy, J. E. Gunn, and M. White. The Propagation of Uncertainties in Stellar Population Synthesis Modeling. I. The Relevance of Uncertain Aspects of Stellar Evolution and the Initial Mass Function to the Derived Physical Properties of Galaxies. *The Astrophysical Journal*, 699(1):486–506, July 2009.

[34] C. J. Conselice, C. J. Mundy, L. Ferreira, and K. Duncan. A direct measurement of galaxy major and minor merger rates and stellar mass accretion histories at $z < 3$ using galaxy pairs in the REFINE survey. *arXiv e-prints*, page arXiv:2207.03984, July 2022.

[35] M. C. Cooper, R. L. Griffith, J. A. Newman, A. L. Coil, M. Davis, A. A. Dutton, S. M. Faber, P. Guhathakurta, D. C. Koo, J. M. Lotz, B. J. Weiner, C. N. A. Willmer, and R. Yan. The DEEP3 Galaxy Redshift Survey: the impact of environment on the size evolution of massive early-type galaxies at intermediate redshift. *Monthly Notices of the Royal Astronomical Society*, 419(4):3018–3027, Feb. 2012.

[36] S. Courteau, M. Cappellari, R. S. de Jong, A. A. Dutton, E. Emsellem, H. Hoekstra, L. V. E. Koopmans, G. A. Mamon, C. Maraston, T. Treu, and L. M. Widrow. Galaxy masses. *Reviews of Modern Physics*, 86(1):47–119, Jan. 2014.

[37] T. J. Cox, S. N. Dutta, T. Di Matteo, L. Hernquist, P. F. Hopkins, B. Robertson, and V. Springel. The Kinematic Structure of Merger Remnants. *The Astrophysical Journal*, 650(2):791–811, Oct. 2006.

[38] E. Daddi, A. Renzini, N. Pirzkal, A. Cimatti, S. Malhotra, M. Stiavelli, C. Xu, A. Pasquali, J. E. Rhoads, M. Brusa, S. di Serego Alighieri, H. C. Ferguson, A. M. Koekemoer, L. A. Moustakas, N. Panagia, and R. A. Windhorst. Passively Evolving Early-Type Galaxies at $1.4 < z < 2.5$ in the Hubble Ultra Deep Field. *The Astrophysical Journal*, 626(2):680–697, June 2005.

[39] I. Damjanov, M. J. Geller, H. J. Zahid, and H. S. Hwang. Quiescent compact galaxies at intermediate redshift in the cosmos field. the number density. *The Astrophysical Journal*, 806(2):158, jun 2015.

[40] I. Damjanov, P. J. McCarthy, R. G. Abraham, K. Glazebrook, H. Yan, E. Mentuch, D. Le Borgne, S. Savaglio, D. Crampton, R. Murowinski, S. Juneau, R. G. Carlberg, I. Jørgensen, K. Roth, H.-W. Chen, and R. O. Marzke. Red Nuggets at z ~1.5: Compact Passive Galaxies and the Formation of the Kormendy Relation. *The Astrophysical Journal*, 695(1):101–115, Apr. 2009.

[41] R. Davari, L. C. Ho, C. Y. Peng, and S. Huang. How Robust are the Size Measurements of High-redshift Compact Galaxies? *The Astrophysical Journal*, 787(1):69, May 2014.

[42] M. Davis, G. Efstathiou, C. S. Frenk, and S. D. M. White. The evolution of large-scale structure in a universe dominated by cold dark matter. *The Astrophysical Journal*, 292:371–394, May 1985.

[43] A. de Graaff, J. Trayford, M. Franx, M. Schaller, J. Schaye, and A. van der Wel. Observed structural parameters of EAGLE galaxies: reconciling the mass-size relation in simulations with local observations. *Monthly Notices of the Royal Astronomical Society*, 511(2):2544–2564, Apr. 2022.

[44] G. de Vaucouleurs. Recherches sur les Nebuleuses Extragalactiques. *Annales d'Astrophysique*, 11:247, Jan. 1948.

[45] A. Dekel and Y. Birnboim. Galaxy bimodality due to cold flows and shock heating. *Monthly Notices of the Royal Astronomical Society*, 368(1):2–20, May 2006.

[46] A. Dekel and T. J. Cox. The dissipative merger progenitors of elliptical galaxies. *Monthly Notices of the Royal Astronomical Society*, 370(3):1445–1453, Aug. 2006.

[47] A. Dekel, R. Sari, and D. Ceverino. Formation of Massive Galaxies at High Redshift: Cold Streams, Clumpy Disks, and Compact Spheroids. *The Astrophysical Journal*, 703(1):785–801, Sept. 2009.

[48] P. Di Matteo, A. Pipino, M. D. Lehnert, F. Combes, and B. Semelin. On the survival of metallicity gradients to major dry-mergers. *Astronomy & Astrophysics*, 499(2):427–437, May 2009.

[49] K. Dolag, S. Borgani, G. Murante, and V. Springel. Substructures in hydrodynamical cluster simulations. *Monthly Notices of the Royal Astronomical Society*, 399(2):497–514, Oct. 2009.

[50] H. Domínguez Sánchez, P. G. Pérez-González, P. Esquej, M. C. Eliche-Moral, G. Barro, A. Cava, A. M. Koekemoer, B. Alcalde Pampliega, A. Alonso Herrero, G. Bruzual, N. Cardiel, J. Cenarro, D. Ceverino, S. Charlot, and A. Hernán Caballero. Pathways to quiescence: SHARDS view on the star formation histories of massive quiescent galaxies at $1.0 < z < 1.5$. *Monthly Notices of the Royal Astronomical Society*, 457(4):3743–3768, Apr. 2016.

[51] M. Donnari, A. Pillepich, D. Nelson, M. Vogelsberger, S. Genel, R. Weinberger, F. Marinacci, V. Springel, and L. Hernquist. The star formation activity of IllustrisTNG galaxies: main sequence, UVJ diagram, quenched fractions, and systematics. *Monthly Notices of the Royal Astronomical Society*, 485(4):4817–4840, June 2019.

[52] A. R. Duffy, J. Schaye, S. T. Kay, and C. Dalla Vecchia. Dark matter halo concentrations in the Wilkinson Microwave Anisotropy Probe year 5 cosmology. *Monthly Notices of the Royal Astronomical Society*, 390(1):L64–L68, Oct. 2008.

[53] A. A. Dutton and A. V. Macciò. Cold dark matter haloes in the Planck era: evolution of structural parameters for Einasto and NFW profiles. *Monthly Notices of the Royal Astronomical Society*, 441(4):3359–3374, July 2014.

[54] A. A. Dutton and A. V. Macciò. Cold dark matter haloes in the Planck era: evolution of structural parameters for Einasto and NFW profiles. *Mon. Not. Roy. Astron. Soc.*, 441(4):3359–3374, 2014.

[55] J. Einasto. On the Construction of a Composite Model for the Galaxy and on the Determination of the System of Galactic Parameters. *Trudy Astrofizicheskogo Instituta Alma-Ata*, 5:87–100, Jan. 1965.

[56] S. M. Faber. Quadratic programming applied to the problem of galaxy population synthesis. *Astronomy & Astrophysics*, 20:361, Sept. 1972.

[57] M. Fagioli, C. M. Carollo, A. Renzini, S. J. Lilly, M. Onodera, and S. Tacchella. Minor mergers or progenitor bias? the stellar ages of small and large quenched galaxies. *The Astrophysical Journal*, 831(2):173, nov 2016.

[58] A. Ferré-Mateu, I. Trujillo, I. Martín-Navarro, A. Vazdekis, M. Mezcua, M. Balcells, and L. Domínguez. Two new confirmed massive relic galaxies: red nuggets in the present-day Universe. *Monthly Notices of the Royal Astronomical Society*, 467(2):1929–1939, May 2017.

[59] R. Flores-Freitas, A. L. Chies-Santos, C. Furlanetto, M. E. De Rossi, L. Ferreira, L. J. Zenocratti, and K. A. Alamo-Martínez. Relic galaxy analogues in TNG50 simulation: the formation pathways of surviving red nuggets in a cosmological simulation. *Monthly Notices of the Royal Astronomical Society*, 512(1):245–264, May 2022.

[60] R. Flores-Freitas, A. L. Chies-Santos, C. Furlanetto, M. E. D. Rossi, L. Ferreira, L. J. Zenocratti, and K. A. Alamo-Martínez. Relic galaxy analogues in TNG50 simulation: the formation pathways of surviving red nuggets in a cosmological simulation. *Monthly Notices of the Royal Astronomical Society*, 512(1):245–264, feb 2022.

[61] D. A. Forbes, L. R. Spitler, J. Strader, A. J. Romanowsky, J. P. Brodie, and C. Foster. Evidence for two phases of galaxy formation from radial trends in the globular cluster system of NGC 1407. *Monthly Notices of the Royal Astronomical Society*, 413(4):2943–2949, June 2011.

[62] M. Furlong, R. G. Bower, R. A. Crain, J. Schaye, T. Theuns, J. W. Trayford, Y. Qu, M. Schaller, M. Berthet, and J. C. Helly. Size evolution of normal and compact galaxies in the EAGLE simulation. *Monthly Notices of the Royal Astronomical Society*, 465(1):722–738, Feb. 2017.

[63] A. Gargiulo, P. Saracco, S. Tamburri, I. Lonoce, and F. Ciocca. Ultramassive dense early-type galaxies: Velocity dispersions and number density evolution since z = 1.6. *Astronomy & Astrophysics*, 592:A132, Aug. 2016.

[64] F. Gastaldello, D. A. Buote, P. J. Humphrey, L. Zappacosta, J. S. Bullock, F. Brighenti, and W. G. Mathews. Probing the Dark Matter and Gas Fraction in Relaxed Galaxy Groups with X-Ray Observations from Chandra and XMM-Newton. *The Astrophysical Journal*, 669(1):158–183, Nov. 2007.

[65] S. Genel, D. Nelson, A. Pillepich, V. Springel, R. Pakmor, R. Weinberger, L. Hernquist, J. Naiman, M. Vogelsberger, F. Marinacci, and P. Torrey. The size evolution of star-forming and quenched galaxies in the IllustrisTNG simulation. *Monthly Notices of the Royal Astronomical Society*, 474(3):3976–3996, Mar. 2018.

[66] C. Grillo, R. Gobat, P. Rosati, and M. Lombardi. Stellar mass estimates in early-type galaxies from lensing+dynamical and photometric measurements. *Astronomy & Astrophysics*, 477(2):L25–L28, Jan. 2008.

[67] J. E. Gunn. Massive galactic halos. I. Formation and evolution. *The Astrophysical Journal*, 218:592–598, Dec. 1977.

[68] J. E. Gunn and I. Gott, J. Richard. On the Infall of Matter Into Clusters of Galaxies and Some Effects on Their Evolution. *The Astrophysical Journal*, 176:1, Aug. 1972.

[69] B. Häußler, S. P. Bamford, M. Vika, A. L. Rojas, M. Barden, L. S. Kelvin, M. Alpaslan, A. S. G. Robotham, S. P. Driver, I. K. Baldry, S. Brough, A. M. Hopkins, J. Liske, R. C. Nichol, C. C. Popescu, and R. J. Tuffs. MegaMorph - multiwavelength measurement of galaxy structure: complete Sérsic profile information from modern surveys. *Monthly Notices of the Royal Astronomical Society*, 430(1):330–369, Mar. 2013.

[70] B. Häussler, D. H. McIntosh, M. Barden, E. F. Bell, H.-W. Rix, A. Borch, S. V. W. Beckwith, J. A. R. Caldwell, C. Heymans, K. Jahnke, S. Jogee, S. E. Koposov, K. Meisenheimer, S. F. Sánchez, R. S. Somerville, L. Wisotzki, and C. Wolf. GEMS: Galaxy Fitting Catalogs and Testing Parametric Galaxy Fitting Codes: GALFIT and GIM2D. *The Astrophysical Journal Supplement*, 172(2):615–633, Oct. 2007.

[71] C. Hernández-Aguayo, V. Springel, R. Pakmor, M. Barrera, F. Ferlito, S. D. M. White, L. Hernquist, B. Hadzhiyska, A. M. Delgado, R. Kannan, S. Bose, and C. Frenk. The MillenniumTNG Project: high-precision predictions for matter clustering and halo statistics. *Monthly Notices of the Royal Astronomical Society*, 524(2):2556–2578, Sept. 2023.

[72] A. R. Hill, A. van der Wel, M. Franx, A. Muzzin, R. E. Skelton, I. Momcheva, P. van Dokkum, and K. E. Whitaker. High-redshift Massive Quiescent Galaxies Are as Flat as Star-forming Galaxies: The Flattening of Galaxies and the Correlation with Structural Properties in CANDELS/3D-HST. *The Astrophysical Journal*, 871(1):76, Jan. 2019.

[73] M. Hilz, T. Naab, and J. P. Ostriker. How do minor mergers promote inside-out growth of ellipticals, transforming the size, density profile and dark matter fraction? *Monthly Notices of the Royal Astronomical Society*, 429(4):2924–2933, Mar. 2013.

[74] B. P. Holden, A. van der Wel, H.-W. Rix, and M. Franx. A Constant Limiting Mass Scale for Flat Early-type Galaxies from z ~1 to z = 0: Density Evolves but Shapes Do Not. *The Astrophysical Journal*, 749(2):96, Apr. 2012.

[75] P. F. Hopkins, L. Hernquist, T. J. Cox, D. Keres, and S. Wuyts. Dissipation and extra light in galactic nuclei. iv. evolution in the scaling relations of spheroids. *The Astrophysical Journal*, 691(2):1424, feb 2009.

[76] P. F. Hopkins, L. Hernquist, T. J. Cox, D. Keres, and S. Wuyts. Dissipation and Extra Light in Galactic Nuclei. IV. Evolution in the Scaling Relations of Spheroids. *The Astrophysical Journal*, 691(2):1424–1458, Feb. 2009.

[77] S. Huang, L. C. Ho, C. Y. Peng, Z.-Y. Li, and A. J. Barth. The Carnegie-Irvine Galaxy Survey. III. The Three-component Structure of Nearby Elliptical Galaxies. *The Astrophysical Journal*, 766(1):47, Mar. 2013.

[78] S. Huang, L. C. Ho, C. Y. Peng, Z.-Y. Li, and A. J. Barth. The Carnegie-Irvine Galaxy Survey. IV. A Method to Determine the Average Mass Ratio of Mergers That Built Massive Elliptical Galaxies. *arXiv e-prints*, page arXiv:1603.00876, Mar. 2016.

[79] M. Huertas-Company, S. Mei, F. Shankar, L. Delaye, A. Raichoor, G. Covone, A. Finoguenov, J. P. Kneib, F. O. Le, and M. Povic. The evolution of the mass–size relation for early-type galaxies from z 1 to the present: dependence on environment, mass range and detailed morphology. *Monthly Notices of the Royal Astronomical Society*, 428(2):1715–1742, 11 2012.

[80] P. J. Humphrey, D. A. Buote, F. Gastaldello, L. Zappacosta, J. S. Bullock, F. Brighenti, and W. G. Mathews. A Chandra View of Dark Matter in Early-Type Galaxies. *The Astrophysical Journal*, 646(2):899–918, Aug. 2006.

[81] J. B. Hyde and M. Bernardi. Curvature in the scaling relations of early-type galaxies. *Monthly Notices of the Royal Astronomical Society*, 394(4):1978–1990, 04 2009.

[82] J. B. Hyde and M. Bernardi. The luminosity and stellar mass Fundamental Plane of early-type galaxies. *Monthly Notices of the Royal Astronomical Society*, 396(2):1171–1185, June 2009.

[83] K. Kelkar, A. Aragón-Salamanca, M. E. Gray, D. Maltby, B. Vulcani, G. De Lucia, B. M. Poggianti, and D. Zaritsky. Galaxy sizes as a function of environment at intermediate redshift from the ESO Distant Cluster Survey. *Monthly Notices of the Royal Astronomical Society*, 450(2):1246–1255, 04 2015.

[84] L. S. Kelvin, S. P. Driver, A. S. G. Robotham, D. T. Hill, M. Alpaslan, I. K. Baldry, S. P. Bamford, J. Bland-Hawthorn, S. Brough, A. W. Graham, B. Häussler, A. M. Hopkins, J. Liske, J. Loveday, P. Norberg, S. Phillipps, C. C. Popescu, M. Prescott, E. N. Taylor, and R. J. Tuffs. Galaxy And Mass Assembly (GAMA): Structural Investigation of Galaxies via Model Analysis. *Monthly Notices of the Royal Astronomical Society*, 421(2):1007–1039, Apr. 2012.

[85] R. Kennedy, S. P. Bamford, I. Baldry, B. Häußler, B. W. Holwerda, A. M. Hopkins, L. S. Kelvin, R. Lange, A. J. Moffett, C. C. Popescu, E. N. Taylor, R. J. Tuffs, M. Vika, and B. Vulcani. Galaxy And Mass Assembly (GAMA): the wavelength dependence of galaxy structure versus redshift and luminosity. *Monthly Notices of the Royal Astronomical Society*, 454(1):806–817, Nov. 2015.

[86] S. Khochfar and J. Silk. Dry mergers: a crucial test for galaxy formation. *Monthly Notices of the Royal Astronomical Society*, 397(1):506–510, July 2009.

[87] A. A. Klypin, S. Trujillo-Gomez, and J. Primack. Dark Matter Halos in the Standard Cosmological Model: Results from the Bolshoi Simulation. *The Astrophysical Journal*, 740(2):102, Oct. 2011.

[88] C. Kobayashi. GRAPE-SPH chemodynamical simulation of elliptical galaxies - I. Evolution of metallicity gradients. *Monthly Notices of the Royal Astronomical Society*, 347(3):740–758, Jan. 2004.

[89] A. M. Koekemoer, S. M. Faber, H. C. Ferguson, N. A. Grogin, D. D. Kocevski, D. C. Koo, K. Lai, J. M. Lotz, R. A. Lucas, E. J. McGrath, S. Ogaz, A. Rajan, A. G. Riess, S. A. Rodney, L. Strolger, S. Casertano, M. Castellano, T. Dahlen, M. Dickinson, T. Dolch, A. Fontana, M. Giavalisco, A. Grazian, Y. Guo, N. P. Hathi, K.-H. Huang, A. van der Wel, H.-J. Yan, V. Acquaviva, D. M. Alexander, O. Almaini, M. L. N. Ashby, M. Barden, E. F. Bell, F. Bournaud, T. M. Brown, K. I. Caputi, P. Cassata, P. J. Challis, R.-R. Chary, E. Cheung, M. Cirasuolo, C. J. Conselice, A. Roshan Cooray, D. J. Croton, E. Daddi, R. Davé, D. F. de Mello, L. de Ravel, A. Dekel, J. L. Donley, J. S. Dunlop, A. A. Dutton, D. Elbaz, G. G. Fazio, A. V. Filippenko, S. L. Finkelstein, C. Frazer, J. P. Gardner, P. M. Garnavich, E. Gawiser, R. Gruetzbauch, W. G. Hartley, B. Häussler, J. Herrington, P. F. Hopkins, J.-S. Huang, S. W. Jha, A. Johnson, J. S. Kartaltepe, A. A. Khostovan, R. P. Kirshner, C. Lani, K.-S. Lee, W. Li, P. Madau, P. J. McCarthy, D. H. McIntosh, R. J. McLure, C. McPartland, B. Mobasher, H. Moreira, A. Mortlock, L. A. Moustakas, M. Mozena, K. Nandra, J. A. Newman, J. L. Nielsen, S. Niemi, K. G. Noeske, C. J. Papovich, L. Pentericci, A. Pope, J. R. Primack, S. Ravindranath, N. A. Reddy, A. Renzini, H.-W. Rix, A. R. Robaina, D. J. Rosario, P. Rosati, S. Salimbeni, C. Scarlata, B. Siana, L. Simard, J. Smidt, D. Snyder, R. S. Somerville, H. Spinrad, A. N. Straughn, O. Telford, H. I. Teplitz, J. R. Trump, C. Vargas, C. Villforth, C. R. Wagner, P. Wandro, R. H. Wechsler, B. J. Weiner, T. Wiklind, V. Wild, G. Wilson, S. Wuyts, and M. S. Yun. CANDELS: The Cosmic Assembly Near-infrared Deep Extragalactic Legacy Survey—The Hubble Space Telescope Observations, Imaging Data Products, and Mosaics. *The Astrophysical Journal Supplement*, 197(2):36, Dec. 2011.

[90] L. V. E. Koopmans, T. Treu, A. S. Bolton, S. Burles, and L. A. Moustakas. The Sloan Lens ACS Survey. III. The Structure and Formation of Early-Type Galaxies and Their Evolution since z ~1. *The Astrophysical Journal*, 649(2):599–615, Oct. 2006.

[91] J. Kormendy, D. B. Fisher, M. E. Cornell, and R. Bender. Structure and Formation of

Elliptical and Spheroidal Galaxies. *The Astrophysical Journal Supplement*, 182(1):216–309, May 2009.

[92] M. Kriek, P. G. van Dokkum, I. Labbé, M. Franx, G. D. Illingworth, D. Marchesini, and R. F. Quadri. An ultra-deep near-infrared spectrum of a compact quiescent galaxy at z = 2.2. *The Astrophysical Journal*, 700(1):221, jul 2009.

[93] P. Kroupa. On the variation of the initial mass function. *Monthly Notices of the Royal Astronomical Society*, 322(2):231–246, Apr. 2001.

[94] F. La Barbera, R. R. de Carvalho, I. G. de la Rosa, P. A. A. Lopes, J. L. Kohl-Moreira, and H. V. Capelato. Spheroid's Panchromatic Investigation in Different Environmental Regions (SPIDER) - I. Sample and galaxy parameters in the grizYJHK wavebands. *arXiv e-prints*, page arXiv:0912.4547, Dec. 2009.

[95] F. La Barbera, R. R. de Carvalho, I. G. de la Rosa, P. A. A. Lopes, J. L. Kohl-Moreira, and H. V. Capelato. SPIDER – I. Sample and galaxy parameters in the grizYJHK wavebands. *Monthly Notices of the Royal Astronomical Society*, 408(3):1313–1334, 10 2010.

[96] C. Lacey and S. Cole. Merger rates in hierarchical models of galaxy formation. *Monthly Notices of the Royal Astronomical Society*, 262(3):627–649, June 1993.

[97] C. Lacey and S. Cole. Merger Rates in Hierarchical Models of Galaxy Formation - Part Two - Comparison with N-Body Simulations. *Monthly Notices of the Royal Astronomical Society*, 271:676, Dec. 1994.

[98] R. Lange, S. P. Driver, A. S. G. Robotham, L. S. Kelvin, A. W. Graham, M. Alpaslan, S. K. Andrews, I. K. Baldry, S. Bamford, J. Bland-Hawthorn, S. Brough, M. E. Cluver, C. J. Conselice, L. J. M. Davies, B. Haeussler, I. S. Konstantopoulos, J. Loveday, A. J. Moffett, P. Norberg, S. Phillipps, E. N. Taylor, Á. R. López-Sánchez, and S. M. Wilkins. Galaxy And Mass Assembly (GAMA): mass-size relations of $z < 0.1$ galaxies subdivided by Sérsic index, colour and morphology. *Monthly Notices of the Royal Astronomical Society*, 447(3):2603–2630, Mar. 2015.

[99] G. Lemson and G. Kauffmann. Environmental influences on dark matter haloes and consequences for the galaxies within them. *Monthly Notices of the Royal Astronomical Society*, 302(1):111–117, Jan. 1999.

[100] Y. Li, M. Habouzit, S. Genel, R. Somerville, B. A. Terrazas, E. F. Bell, A. Pillepich, D. Nelson, R. Weinberger, V. Rodriguez-Gomez, C.-P. Ma, R. Pakmor, L. Hernquist, and M. Vogelsberger. Correlations between Black Holes and Host Galaxies in the Illustris and IllustrisTNG Simulations. *The Astrophysical Journal*, 895(2):102, June 2020.

[101] Y. Li, H. J. Mo, and L. Gao. On halo formation times and assembly bias. *Monthly Notices of the Royal Astronomical Society*, 389(3):1419–1426, Sept. 2008.

[102] L. Lin, M. C. Cooper, H.-Y. Jian, D. C. Koo, D. R. Patton, R. Yan, C. N. A. Willmer, A. L. Coil, T. Chiueh, D. J. Croton, B. F. Gerke, J. Lotz, P. Guhathakurta, and J. A. Newman. WHERE DO WET, DRY, AND MIXED GALAXY MERGERS OCCUR? a STUDY OF THE ENVIRONMENTS OF CLOSE GALAXY PAIRS IN THE DEEP2 GALAXY REDSHIFT SURVEY. *The Astrophysical Journal*, 718(2):1158–1170, jul 2010.

[103] K. Lisiecki, K. Małek, M. Siudek, A. Pollo, J. Krywult, A. Karska, and Junais. The first catalogue of spectroscopically confirmed red nuggets at z $\sim$ 0.7 from the VIPERS survey. Linking high-z red nuggets and local relics. *Astronomy & Astrophysics*, 669:A95, Jan. 2023.

[104] J. M. Lotz, P. Jonsson, T. J. Cox, D. Croton, J. R. Primack, R. S. Somerville, and K. Stewart. The Major and Minor Galaxy Merger Rates at z < 1.5. *The Astrophysical Journal*, 742(2):103, Dec. 2011.

[105] S. Lower, D. Narayanan, J. Leja, B. D. Johnson, C. Conroy, and R. Davé. How Well Can We Measure the Stellar Mass of a Galaxy: The Impact of the Assumed Star Formation History Model in SED Fitting. *The Astrophysical Journal*, 904(1):33, Nov. 2020.

[106] D. Lynden-Bell. Statistical mechanics of violent relaxation in stellar systems. *Monthly Notices of the Royal Astronomical Society*, 136:101, Jan. 1967.

[107] L. A. MacArthur, S. Courteau, and J. A. Holtzman. Structure of Disk-dominated Galaxies. I. Bulge/Disk Parameters, Simulations, and Secular Evolution. *The Astrophysical Journal*, 582(2):689–722, Jan. 2003.

[108] A. V. Macciò, A. A. Dutton, and F. C. van den Bosch. Concentration, spin and shape of dark matter haloes as a function of the cosmological model: WMAP1, WMAP3 and WMAP5 results. *Monthly Notices of the Royal Astronomical Society*, 391(4):1940–1954, Dec. 2008.

[109] A. V. Macciò, A. A. Dutton, F. C. van den Bosch, B. Moore, D. Potter, and J. Stadel. Concentration, spin and shape of dark matter haloes: scatter and the dependence on mass and environment. *Monthly Notices of the Royal Astronomical Society*, 378(1):55–71, June 2007.

[110] P. Madau and M. Dickinson. Cosmic Star Formation History. *Ann. Rev. Astron. Astrophys.*, 52:415–486, 2014.

[111] D. T. Maltby, A. Aragón-Salamanca, M. E. Gray, M. Barden, B. Häußler, C. Wolf, C. Y. Peng, K. Jahnke, D. H. McIntosh, A. Böhm, and E. van Kampen. The environmental dependence of the stellar-mass-size relation in STAGES galaxies. *Monthly Notices of the Royal Astronomical Society*, 402(1):282–294, Feb. 2010.

[112] A. W. S. Man, S. Toft, A. W. Zirm, S. Wuyts, and A. van der Wel. The Pair Fraction of Massive Galaxies at $0 \leq z \leq 3$. *The Astrophysical Journal*, 744(2):85, Jan. 2012.

[113] A. W. S. Man, A. W. Zirm, and S. Toft. Resolving the Discrepancy of Galaxy Merger Fraction Measurements at z $\sim$ 0-3. *The Astrophysical Journal*, 830(2):89, Oct. 2016.

[114] A. W. S. Man, A. W. Zirm, and S. Toft. RESOLVING THE DISCREPANCY OF GALAXY MERGER FRACTION MEASUREMENTS ATiz/i$\sim$ 0–3. *The Astrophysical Journal*, 830(2):89, oct 2016.

[115] F. Marinacci, M. Vogelsberger, R. Pakmor, P. Torrey, V. Springel, L. Hernquist, D. Nelson, R. Weinberger, A. Pillepich, J. Naiman, and S. Genel. First results from the IllustrisTNG simulations: radio haloes and magnetic fields. *Monthly Notices of the Royal Astronomical Society*, 480(4):5113–5139, Nov. 2018.

[116] G. Martin, S. Kaviraj, J. E. G. Devriendt, Y. Dubois, C. Laigle, and C. Pichon. The limited role of galaxy mergers in driving stellar mass growth over cosmic time. *Monthly Notices of the Royal Astronomical Society*, 472(1):L50–L54, Nov. 2017.

[117] I. Martín-Navarro, G. van de Ven, and A. Yıldırım. Star formation quenching imprinted on the internal structure of naked red nuggets. *Monthly Notices of the Royal Astronomical Society*, 487(4):4939–4950, 06 2019.

[118] M. Matteuzzi, F. Marinacci, C. Nipoti, and S. Andreon. Newcomers and suburbanites can drive the evolution of the size-stellar mass relation of early-type galaxies in galaxy clusters. *Monthly Notices of the Royal Astronomical Society*, 513(3):3893–3905, July 2022.

[119] A. Meert, V. Vikram, and M. Bernardi. Simulations of single- and two-component galaxy decompositions for spectroscopically selected galaxies from the Sloan Digital Sky Survey. *Monthly Notices of the Royal Astronomical Society*, 433(2):1344–1361, Aug. 2013.

[120] A. Meert, V. Vikram, and M. Bernardi. A catalogue of 2D photometric decompositions in the SDSS-DR7 spectroscopic main galaxy sample: preferred models and systematics. *Monthly Notices of the Royal Astronomical Society*, 446(4):3943–3974, 12 2014.

[121] T. B. Miller, P. van Dokkum, L. Mowla, and A. van der Wel. A New View of the Size-Mass Distribution of Galaxies: Using r $_{20}$ and r $_{80}$ Instead of r $_{50}$. *The Astrophysical Journal Letters*, 872(1):L14, Feb. 2019.

[122] H. Mo, F. C. van den Bosch, and S. White. *Galaxy Formation and Evolution*. 2010.

[123] B. Moore, G. Lake, and N. Katz. Morphological Transformation from Galaxy Harassment. *The Astrophysical Journal*, 495(1):139–151, Mar. 1998.

[124] S. More, A. V. Kravtsov, N. Dalal, and S. Gottlöber. The Overdensity and Masses of the Friends-of-friends Halos and Universality of Halo Mass Function. *The Astrophysical Journal Supplement*, 195(1):4, July 2011.

[125] M. Mosleh, S. Hosseinnejad, S. Z. Hosseini-ShahiSavandi, and S. Tacchella. Galaxy Sizes Since z = 2 from the Perspective of Stellar Mass Distribution within Galaxies. *The Astrophysical Journal*, 905(2):170, Dec. 2020.

[126] M. Mosleh, S. Tavasoli, and S. Tacchella. Stellar Mass Profiles of Quiescent Galaxies in Different Environments at z $\sim$ 0. *The Astrophysical Journal*, 861(2):101, July 2018.

[127] M. Mosleh, R. J. Williams, and M. Franx. On the Robustness of z = 0-1 Galaxy Size Measurements through Model and Non-parametric Fits. *The Astrophysical Journal*, 777(2):117, Nov. 2013.

[128] L. A. Mowla, P. van Dokkum, G. B. Brammer, I. Momcheva, A. van der Wel, K. Whitaker, E. Nelson, R. Bezanson, A. Muzzin, M. Franx, J. MacKenty, J. Leja, M. Kriek, and D. Marchesini. COSMOS-DASH: The Evolution of the Galaxy Size-Mass Relation since z $\sim$ 3 from New Wide-field WFC3 Imaging Combined with CANDELS/3D-HST. *The Astrophysical Journal*, 880(1):57, July 2019.

[129] S. I. Muldrew, D. J. Croton, R. A. Skibba, F. R. Pearce, H. B. Ann, I. K. Baldry, S. Brough, Y.-Y. Choi, C. J. Conselice, N. B. Cowan, A. Gallazzi, M. E. Gray, R. Grützbauch, I. H. Li, C. Park, S. V. Pilipenko, B. J. Podgorzec, A. S. G. Robotham, D. J. Wilman, X. Yang, Y. Zhang, and S. Zibetti. Measures of galaxy environment - I. What is 'environment'? *Monthly Notices of the Royal Astronomical Society*, 419(3):2670–2682, Jan. 2012.

[130] A. Muzzin, D. Marchesini, M. Stefanon, M. Franx, H. J. McCracken, B. Milvang-Jensen, J. S. Dunlop, J. P. U. Fynbo, G. Brammer, I. Labbé, and P. G. van Dokkum. The Evolution of the Stellar Mass Functions of Star-forming and Quiescent Galaxies to z = 4 from the COSMOS/UltraVISTA Survey. *The Astrophysical Journal*, 777(1):18, Nov. 2013.

[131] A. Muzzin, D. Marchesini, P. G. van Dokkum, I. Labbé, M. Kriek, and M. Franx. A Near-Infrared Spectroscopic Survey of K-Selected Galaxies at z~2.3: Comparison of Stellar Population Synthesis Codes and Constraints from the Rest-Frame NIR. *The Astrophysical Journal*, 701(2):1839–1864, Aug. 2009.

[132] T. Naab, P. H. Johansson, and J. P. Ostriker. MINOR MERGERS AND THE SIZE EVOLUTION OF ELLIPTICAL GALAXIES. *The Astrophysical Journal*, 699(2):L178–L182, jun 2009.

[133] P. B. Nair, S. van den Bergh, and R. G. Abraham. The Environmental Dependence of the Luminosity-Size Relation for Galaxies. *The Astrophysical Journal*, 715(1):606–622, May 2010.

[134] J. F. Navarro, C. S. Frenk, and S. D. M. White. The Structure of Cold Dark Matter Halos. *The Astrophysical Journal*, 462:563, May 1996.

[135] J. F. Navarro, C. S. Frenk, and S. D. M. White. A Universal Density Profile from Hierarchical Clustering. *The Astrophysical Journal*, 490(2):493–508, Dec. 1997.

[136] K. V. Nedkova, B. Häußler, D. Marchesini, P. Dimauro, G. Brammer, P. Eigenthaler, A. D. Feinstein, H. C. Ferguson, M. Huertas-Company, E. J. Johnston, E. Kado-Fong, J. S. Kartaltepe, I. Labbé, D. Lange-Vagle, N. S. Martis, E. J. McGrath, A. Muzzin, P. Oesch, Y. Ordenes-Briceño, T. Puzia, H. V. Shipley, B. D. Simmons, R. E. Skelton, M. Stefanon, A. van der Wel, and K. E. Whitaker. Extending the evolution of the stellar mass-size relation at z $\leq$ 2 to low stellar mass galaxies from HFF and CANDELS. *Monthly Notices of the Royal Astronomical Society*, 506(1):928–956, Sept. 2021.

[137] D. Nelson et al. The IllustrisTNG Simulations: Public Data Release. 12 2018.

[138] D. Nelson, A. Pillepich, V. Springel, R. Weinberger, L. Hernquist, R. Pakmor, S. Genel, P. Torrey, M. Vogelsberger, G. Kauffmann, F. Marinacci, and J. Naiman. First results from the IllustrisTNG simulations: the galaxy colour bimodality. *Monthly Notices of the Royal Astronomical Society*, 475(1):624–647, Mar. 2018.

[139] D. Nelson, V. Springel, A. Pillepich, V. Rodriguez-Gomez, P. Torrey, S. Genel, M. Vogelsberger, R. Pakmor, F. Marinacci, R. Weinberger, L. Kelley, M. Lovell, B. Diemer, and L. Hernquist. The IllustrisTNG simulations: public data release. *Computational Astrophysics and Cosmology*, 6(1):2, May 2019.

[140] A. F. Neto, L. Gao, P. Bett, S. Cole, J. F. Navarro, C. S. Frenk, S. D. M. White, V. Springel, and A. Jenkins. The statistics of Λ CDM halo concentrations. *Monthly Notices of the Royal Astronomical Society*, 381(4):1450–1462, Nov. 2007.

[141] A. B. Newman, R. S. Ellis, K. Bundy, and T. Treu. Can Minor Merging Account for the Size Growth of Quiescent Galaxies? New Results from the CANDELS Survey. *The Astrophysical Journal*, 746(2):162, Feb. 2012.

[142] A. B. Newman, R. S. Ellis, T. Treu, and K. Bundy. Keck Spectroscopy of z ¿ 1 Field Spheroidals: Dynamical Constraints on the Growth Rate of Red "Nuggets". *The Astrophysical Journal Letters*, 717(2):L103–L107, July 2010.

[143] A. Niemiec, E. Jullo, C. Giocoli, M. Limousin, and M. Jauzac. Dark matter stripping in galaxy clusters: a look at the stellar-to-halo mass relation in the Illustris simulation. *Monthly Notices of the Royal Astronomical Society*, 487(1):653–666, July 2019.

[144] E. Noordeh, R. E. A. Canning, J. P. Willis, S. W. Allen, A. Mantz, S. A. Stanford, and G. Brammer. Quiescent galaxies in a virialized cluster at redshift 2: evidence for accelerated size growth. *Monthly Notices of the Royal Astronomical Society*, 507(4):5272–5280, Nov. 2021.

[145] T. Okamoto and A. Habe. Formation and Evolution of Galactic Halos in Clusters of Galaxies. *The Astrophysical Journal*, 516(2):591–603, May 1999.

[146] L. Oser, T. Naab, J. P. Ostriker, and P. H. Johansson. The Cosmological Size and Velocity Dispersion Evolution of Massive Early-type Galaxies. *The Astrophysical Journal*, 744(1):63, Jan. 2012.

[147] L. Oser, J. P. Ostriker, T. Naab, P. H. Johansson, and A. Burkert. THE TWO PHASES OF GALAXY FORMATION. *The Astrophysical Journal*, 725(2):2312–2323, dec 2010.

[148] T. Parsotan, R. K. Cochrane, C. C. Hayward, D. Anglés-Alcázar, R. Feldmann, C. A. Faucher-Giguère, S. Wellons, and P. F. Hopkins. Realistic mock observations of the sizes and stellar mass surface densities of massive galaxies in FIRE-2 zoom-in simulations. *Monthly Notices of the Royal Astronomical Society*, 501(2):1591–1602, Feb. 2021.

[149] P. J. E. Peebles. Large-scale background temperature and mass fluctuations due to scale-invariant primeval perturbations. *The Astrophysical Journal Letters*, 263:L1–L5, Dec. 1982.

[150] P. J. E. Peebles. Issues for the next generation of galaxy surveys. *Philosophical Transactions of the Royal Society of London Series A*, 357(1750):21, Jan. 1999.

[151] C. Y. Peng, L. C. Ho, C. D. Impey, and H.-W. Rix. Detailed Decomposition of Galaxy Images. II. Beyond Axisymmetric Models. *The Astronomical Journal*, 139(6):2097–2129, June 2010.

[152] Z. Penoyre, B. P. Moster, D. Sijacki, and S. Genel. The origin and evolution of fast and slow rotators in the Illustris simulation. *Monthly Notices of the Royal Astronomical Society*, 468(4):3883–3906, July 2017.

[153] L. Peralta de Arriba, V. Quilis, I. Trujillo, M. Cebrián, and M. Balcells. Massive relic galaxies prefer dense environments. *Monthly Notices of the Royal Astronomical Society*, 461(1):156–163, Sept. 2016.

[154] L. Peralta de Arriba, V. Quilis, I. Trujillo, M. Cebrián, and M. Balcells. Massive relic galaxies prefer dense environments. *Monthly Notices of the Royal Astronomical Society*, 461(1):156–163, 05 2016.

[155] J. Pforr, C. Maraston, and C. Tonini. Recovering galaxy stellar population properties from broad-band spectral energy distribution fitting - II. The case with unknown redshift. *Monthly Notices of the Royal Astronomical Society*, 435(2):1389–1425, Oct. 2013.

[156] A. Pillepich, D. Nelson, V. Springel, R. Pakmor, P. Torrey, R. Weinberger, M. Vogelsberger, F. Marinacci, S. Genel, A. van der Wel, and L. Hernquist. First results from the TNG50 simulation: the evolution of stellar and gaseous discs across cosmic time. *Monthly Notices of the Royal Astronomical Society*, 490(3):3196–3233, Dec. 2019.

[157] A. Pillepich, V. Springel, D. Nelson, S. Genel, J. Naiman, R. Pakmor, L. Hernquist, P. Torrey, M. Vogelsberger, R. Weinberger, and F. Marinacci. Simulating galaxy formation with the IllustrisTNG model. *Monthly Notices of the Royal Astronomical Society*, 473(3):4077–4106, Jan. 2018.

[158] Planck Collaboration, P. A. R. Ade, N. Aghanim, M. Arnaud, M. Ashdown, J. Aumont, C. Baccigalupi, A. J. Banday, R. B. Barreiro, J. G. Bartlett, N. Bartolo, E. Battaner, R. Battye, K. Benabed, A. Benoît, A. Benoit-Lévy, J. P. Bernard, M. Bersanelli, P. Bielewicz, J. J. Bock, A. Bonaldi, L. Bonavera, J. R. Bond, J. Borrill, F. R. Bouchet, F. Boulanger, M. Bucher, C. Burigana, R. C. Butler, E. Calabrese, J. F. Cardoso, A. Catalano, A. Challinor, A. Chamballu, R. R. Chary, H. C. Chiang, J. Chluba, P. R. Christensen, S. Church, D. L. Clements, S. Colombi, L. P. L. Colombo, C. Combet, A. Coulais, B. P. Crill, A. Curto, F. Cuttaia, L. Danese, R. D. Davies, R. J. Davis, P. de Bernardis, A. de Rosa, G. de Zotti, J. Delabrouille, F. X. Désert, E. Di Valentino, C. Dickinson, J. M. Diego, K. Dolag, H. Dole, S. Donzelli, O. Doré, M. Douspis, A. Ducout, J. Dunkley, X. Dupac, G. Efstathiou, F. Elsner, T. A. Enßlin, H. K. Eriksen, M. Farhang, J. Fergusson, F. Finelli, O. Forni, M. Frailis, A. A. Fraisse, E. Franceschi, A. Frejsel, S. Galeotta, S. Galli, K. Ganga, C. Gauthier, M. Gerbino, T. Ghosh, M. Giard, Y. Giraud-Héraud, E. Giusarma, E. Gjerløw, J. González-Nuevo, K. M. Górski, S. Gratton, A. Gregorio, A. Gruppuso, J. E. Gudmundsson, J. Hamann, F. K. Hansen, D. Hanson, D. L. Harrison, G. Helou, S. Henrot-Versillé, C. Hernández-Monteagudo, D. Herranz, S. R. Hildebrandt, E. Hivon, M. Hobson, W. A. Holmes, A. Hornstrup, W. Hovest, Z. Huang, K. M. Huffenberger, G. Hurier, A. H. Jaffe, T. R. Jaffe, W. C. Jones, M. Juvela, E. Keihänen, R. Keskitalo, T. S. Kisner, R. Kneissl, J. Knoche, L. Knox, M. Kunz, H. Kurki-Suonio, G. Lagache, A. Lähteenmäki, J. M. Lamarre, A. Lasenby, M. Lattanzi, C. R. Lawrence, J. P. Leahy, R. Leonardi, J. Lesgourgues, F. Levrier, A. Lewis, M. Liguori, P. B. Lilje, M. Linden-Vørnle, M. López-Caniego, P. M. Lubin, J. F. Macías-Pérez, G. Maggio, D. Maino, N. Mandolesi, A. Mangilli, A. Marchini, M. Maris, P. G. Martin, M. Martinelli, E. Martínez-González, S. Masi, S. Matarrese, P. McGehee, P. R. Meinhold, A. Melchiorri, J. B. Melin, L. Mendes, A. Mennella, M. Migliaccio, M. Millea, S. Mitra, M. A. Miville-Deschênes, A. Moneti, L. Montier, G. Morgante, D. Mortlock, A. Moss, D. Munshi, J. A. Murphy, P. Naselsky, F. Nati, P. Natoli, C. B. Netterfield, H. U. Nørgaard-Nielsen, F. Noviello, D. Novikov, I. Novikov, C. A. Oxborrow, F. Paci, L. Pagano, F. Pajot, R. Paladini, D. Paoletti, B. Partridge, F. Pasian, G. Patanchon, T. J. Pearson, O. Perdereau, L. Perotto, F. Perrotta, V. Pettorino, F. Piacentini, M. Piat, E. Pierpaoli, D. Pietrobon, S. Plaszczynski, E. Pointecouteau, G. Polenta, L. Popa, G. W. Pratt, G. Prézeau, S. Prunet, J. L. Puget, J. P. Rachen, W. T. Reach, R. Rebolo, M. Reinecke, M. Remazeilles, C. Renault, A. Renzi, I. Ristorcelli, G. Rocha, C. Rosset, M. Rossetti, G. Roudier, B. Rouillé d'Orfeuil, M. Rowan-Robinson, J. A. Rubiño-Martín, B. Rusholme, N. Said, V. Salvatelli, L. Salvati, M. Sandri, D. Santos, M. Savelainen, G. Savini, D. Scott, M. D. Seiffert, P. Serra, E. P. S. Shellard, L. D. Spencer, M. Spinelli, V. Stolyarov, R. Stompor, R. Sudiwala, R. Sunyaev, D. Sutton, A. S. Suur-Uski, J. F. Sygnet, J. A. Tauber, L. Terenzi, L. Toffolatti, M. Tomasi, M. Tristram, T. Trombetti, M. Tucci, J. Tuovinen, M. Türler, G. Umana, L. Valenziano, J. Valiviita, F. Van Tent, P. Vielva, F. Villa, L. A. Wade, B. D. Wandelt, I. K. Wehus, M. White, S. D. M. White, A. Wilkinson, D. Yvon, A. Zacchei, and A. Zonca. Planck 2015 results. XIII. Cosmological parameters. *Astronomy & Astrophysics*, 594:A13, Sept. 2016.

[159] T. J. Ponman, D. J. Allan, L. R. Jones, M. Merrifield, I. M. McHardy, H. J. Lehto,

and G. A. Luppino. A possible fossil galaxy group. *Nature*, 369(6480):462–464, June 1994.

[160] F. Prada, A. A. Klypin, A. J. Cuesta, J. E. Betancort-Rijo, and J. Primack. Halo concentrations in the standard Λ cold dark matter cosmology. *Monthly Notices of the Royal Astronomical Society*, 423(4):3018–3030, July 2012.

[161] W. H. Press and P. Schechter. Formation of Galaxies and Clusters of Galaxies by Self-Similar Gravitational Condensation. *The Astrophysical Journal*, 187:425–438, Feb. 1974.

[162] V. Quilis and I. Trujillo. Expected Number of Massive Galaxy Relics in the Present Day Universe. *The Astrophysical Journal Letters*, 773(1):L8, Aug. 2013.

[163] A. Ragagnin, A. Saro, P. Singh, and K. Dolag. Cosmology dependence of halo masses and concentrations in hydrodynamic simulations. *Monthly Notices of the Royal Astronomical Society*, 500(4):5056–5071, Jan. 2021.

[164] P. Ramachandran, A. Bhosale, K. Puri, P. Negi, A. Muta, A. Dinesh, D. Menon, R. Govind, S. Sanka, A. S. Sebastian, A. Sen, R. Kaushik, A. Kumar, V. Kurapati, M. Patil, D. Tavker, P. Pandey, C. Kaushik, A. Dutt, and A. Agarwal. PySPH: A Python-based Framework for Smoothed Particle Hydrodynamics. *ACM Transactions on Mathematical Software*, 47(4):1–38, Dec. 2021.

[165] R.-S. Remus and D. A. Forbes. Accreted or Not Accreted? The Fraction of Accreted Mass in Galaxies from the Magneticum Simulations and Observations. *The Astrophysical Journal*, 935(1):37, Aug. 2022.

[166] J. H. Reynolds. The light curve of the Andromeda nebula (NGC 224). *Monthly Notices of the Royal Astronomical Society*, 74:132–136, Dec. 1913.

[167] F. Rodriguez, A. D. Montero-Dorta, R. E. Angulo, M. C. Artale, and M. Merchán. The galaxy size-halo mass scaling relations and clustering properties of central and satellite galaxies. *Monthly Notices of the Royal Astronomical Society*, 505(3):3192–3205, Aug. 2021.

[168] V. Rodriguez-Gomez, S. Genel, M. Vogelsberger, D. Sijacki, A. Pillepich, L. V. Sales, P. Torrey, G. Snyder, D. Nelson, V. Springel, C.-P. Ma, and L. Hernquist. The merger rate of galaxies in the Illustris simulation: a comparison with observations and semi-empirical models. *Monthly Notices of the Royal Astronomical Society*, 449(1):49–64, May 2015.

[169] V. Rodriguez-Gomez, G. F. Snyder, J. M. Lotz, D. Nelson, A. Pillepich, V. Springel, S. Genel, R. Weinberger, S. Tacchella, R. Pakmor, P. Torrey, F. Marinacci, M. Vogelsberger, L. Hernquist, and D. A. Thilker. The optical morphologies of galaxies in the IllustrisTNG simulation: a comparison to Pan-STARRS observations. *Monthly Notices of the Royal Astronomical Society*, 483(3):4140–4159, Mar. 2019.

[170] J. Runge, S. A. Walker, and M. S. Mirakhor. The unusually high dark matter concentration of the galaxy group NGC 1600. *Monthly Notices of the Royal Astronomical Society*, 509(2):2647–2653, Jan. 2022.

[171] P. Santini, H. C. Ferguson, A. Fontana, B. Mobasher, G. Barro, M. Castellano, S. L. Finkelstein, A. Grazian, L. T. Hsu, B. Lee, S. K. Lee, J. Pforr, M. Salvato, T. Wiklind, S. Wuyts, O. Almaini, M. C. Cooper, A. Galametz, B. Weiner, R. Amorin, K. Boutsia, C. J. Conselice, T. Dahlen, M. E. Dickinson, M. Giavalisco, N. A. Grogin, Y. Guo, N. P. Hathi, D. Kocevski, A. M. Koekemoer, P. Kurczynski, E. Merlin, A. Mortlock, J. A. Newman, D. Paris, L. Pentericci, R. Simons, and S. P. Willner. Stellar Masses from the CANDELS Survey: The GOODS-South and UDS Fields. *The Astrophysical Journal*, 801(2):97, Mar. 2015.

[172] P. Saracco, A. Gargiulo, F. Ciocca, and D. Marchesini. Cluster and field elliptical galaxies at z 1.3. The marginal role of the environment and the relevance of the galaxy central regions. *Astronomy & Astrophysics*, 597:A122, Jan. 2017.

[173] D. Scognamiglio, C. Tortora, M. Spavone, C. Spiniello, N. R. Napolitano, G. D'Ago, F. La Barbera, F. Getman, N. Roy, M. A. Raj, M. Radovich, M. Brescia, S. Cavuoti, L. V. E. Koopmans, K. H. Kuijken, G. Longo, and C. E. Petrillo. Building the Largest Spectroscopic Sample of Ultracompact Massive Galaxies with the Kilo Degree Survey. *The Astrophysical Journal*, 893(1):4, Apr. 2020.

[174] J. L. Sérsic. Influence of the atmospheric and instrumental dispersion on the brightness distribution in a galaxy. *Boletin de la Asociacion Argentina de Astronomia La Plata Argentina*, 6:41–43, Feb. 1963.

[175] F. Shankar, F. Marulli, M. Bernardi, X. Dai, J. B. Hyde, and R. K. Sheth. Sizes and ages of SDSS ellipticals: comparison with hierarchical galaxy formation models. *Monthly Notices of the Royal Astronomical Society*, 403(1):117–128, Mar. 2010.

[176] S. Shen, H. J. Mo, S. D. M. White, M. R. Blanton, G. Kauffmann, W. Voges, J. Brinkmann, and I. Csabai. The size distribution of galaxies in the Sloan Digital Sky Survey. *Monthly Notices of the Royal Astronomical Society*, 343(3):978–994, Aug. 2003.

[177] L. Simard, C. N. A. Willmer, N. P. Vogt, V. L. Sarajedini, A. C. Phillips, B. J. Weiner, D. C. Koo, M. Im, G. D. Illingworth, and S. M. Faber. The DEEP Groth Strip Survey. II. Hubble Space Telescope Structural Parameters of Galaxies in the Groth Strip. *The Astrophysical Journal Supplement*, 142(1):1–33, Sept. 2002.

[178] M. Sinha and K. Holley-Bockelmann. A First Look at Galaxy Flyby Interactions. I. Characterizing the Frequency of Flybys in a Cosmological Context. *The Astrophysical Journal*, 751(1):17, May 2012.

[179] M. Siudek, K. Lisiecki, J. Krywult, D. Donevski, C. P. Haines, A. Karska, K. Małek, T. Moutard, and A. Pollo. Environments of red nuggets at z 0.7 from the VIPERS

survey. *Monthly Notices of the Royal Astronomical Society*, 523(3):4294–4308, Aug. 2023.

[180] M. Siudek, K. Lisiecki, J. Krywult, D. Donevski, C. P. Haines, A. Karska, K. Małek, T. Moutard, and A. Pollo. Environments of red nuggets at z 0.7 from the VIPERS survey. *Monthly Notices of the Royal Astronomical Society*, 523(3):4294–4308, 06 2023.

[181] R. Smith, H. Choi, J. Lee, J. Rhee, R. Sanchez-Janssen, and S. K. Yi. The Preferential Tidal Stripping of Dark Matter versus Stars in Galaxies. *The Astrophysical Journal*, 833(1):109, Dec. 2016.

[182] R. S. Somerville, G. Lemson, T. S. Kolatt, and A. Dekel. Evaluating approximations for halo merging histories. *Monthly Notices of the Royal Astronomical Society*, 316(3):479–490, Aug. 2000.

[183] C. Spiniello, C. Tortora, G. D'Ago, L. Coccato, F. L. Barbera, A. Ferré -Mateu, C. Pulsoni, M. Arnaboldi, A. Gallazzi, L. Hunt, N. R. Napolitano, M. Radovich, D. Scognamiglio, M. Spavone, and S. Zibetti. INSPIRE: INvestigating stellar population in RElics. *Astronomy &amp Astrophysics*, 654:A136, oct 2021.

[184] C. Spiniello, C. Tortora, G. D'Ago, L. Coccato, F. La Barbera, A. Ferré-Mateu, N. R. Napolitano, M. Spavone, D. Scognamiglio, M. Arnaboldi, A. Gallazzi, L. Hunt, S. Moehler, M. Radovich, and S. Zibetti. INSPIRE: INvestigating Stellar Population In RElics. I. Survey presentation and pilot study. *Astronomy & Astrophysics*, 646:A28, Feb. 2021.

[185] C. Spiniello, C. Tortora, G. D'Ago, L. Coccato, F. La Barbera, A. Ferré-Mateu, C. Pulsoni, M. Arnaboldi, A. Gallazzi, L. Hunt, N. R. Napolitano, M. Radovich, D. Scognamiglio, M. Spavone, and S. Zibetti. INSPIRE: INvestigating Stellar Population In RElics. II. First data release (DR1). *Astronomy & Astrophysics*, 654:A136, Oct. 2021.

[186] H. Spinrad and B. J. Taylor. The Stellar Content of the Nuclei of Nearby Galaxies. I. M31, M32, and M81. *The Astrophysical Journal Supplement*, 22:445, Apr. 1971.

[187] V. Springel. E pur si muove: Galilean-invariant cosmological hydrodynamical simulations on a moving mesh. *Monthly Notices of the Royal Astronomical Society*, 401(2):791–851, Jan. 2010.

[188] V. Springel and L. Hernquist. Cosmological smoothed particle hydrodynamics simulations: a hybrid multiphase model for star formation. *Monthly Notices of the Royal Astronomical Society*, 339(2):289–311, Feb. 2003.

[189] V. Springel, S. D. M. White, A. Jenkins, C. S. Frenk, N. Yoshida, L. Gao, J. Navarro, R. Thacker, D. Croton, J. Helly, J. A. Peacock, S. Cole, P. Thomas, H. Couchman, A. Evrard, J. Colberg, and F. Pearce. Simulations of the formation, evolution and clustering of galaxies and quasars. *Nature*, 435(7042):629–636, June 2005.

[190] V. Springel, S. D. M. White, G. Tormen, and G. Kauffmann. Populating a cluster of galaxies – I. Results at z = 0. *Monthly Notices of the Royal Astronomical Society*, 328(3):726–750, 12 2001.

[191] C. Srisawat, A. Knebe, F. R. Pearce, A. Schneider, P. A. Thomas, P. Behroozi, K. Dolag, P. J. Elahi, J. Han, J. Helly, Y. Jing, I. Jung, J. Lee, Y.-Y. Mao, J. Onions, V. Rodriguez-Gomez, D. Tweed, and S. K. Yi. Sussing Merger Trees: The Merger Trees Comparison Project. *Monthly Notices of the Royal Astronomical Society*, 436(1):150–162, Nov. 2013.

[192] C. L. Steinhardt, J. R. Weaver, J. Maxfield, I. Davidzon, A. L. Faisst, D. Masters, M. Schemel, and S. Toft. A Method to Distinguish Quiescent and Dusty Star-forming Galaxies with Machine Learning. *The Astrophysical Journal*, 891(2):136, Mar. 2020.

[193] D. Steinhauser, S. Schindler, and V. Springel. Simulations of ram-pressure stripping in galaxy-cluster interactions. *Astronomy & Astrophysics*, 591:A51, June 2016.

[194] M. Stringer, I. Trujillo, C. Dalla Vecchia, and I. Martinez-Valpuesta. A cosmological context for compact massive galaxies. *Monthly Notices of the Royal Astronomical Society*, 449(3):2396–2404, 04 2015.

[195] K. A. Suess, M. Kriek, S. H. Price, and G. Barro. Half-mass Radii for ∼7000 Galaxies at $1.0 \leq z \leq 2.5$: Most of the Evolution in the Mass-Size Relation Is Due to Color Gradients. *The Astrophysical Journal*, 877(2):103, June 2019.

[196] D. Szomoru, M. Franx, P. G. van Dokkum, M. Trenti, G. D. Illingworth, I. Labbé, and P. Oesch. The Stellar Mass Structure of Massive Galaxies from z = 0 to z = 2.5: Surface Density Profiles and Half-mass Radii. *The Astrophysical Journal*, 763(2):73, Feb. 2013.

[197] L. Tang, W. Lin, W. Cui, X. Kang, Y. Wang, E. Contini, and Y. Yu. An investigation of intracluster light evolution using cosmological hydrodynamical simulations. *The Astrophysical Journal*, 859(2):85, may 2018.

[198] B. M. Tinsley. Evolution of the Stars and Gas in Galaxies. *The Astrophysical Journal*, 151:547, Feb. 1968.

[199] S. Toft, P. van Dokkum, M. Franx, I. Labbe, N. M. Förster Schreiber, S. Wuyts, T. Webb, G. Rudnick, A. Zirm, M. Kriek, P. van der Werf, J. P. Blakeslee, G. Illingworth, H. W. Rix, C. Papovich, and A. Moorwood. Hubble Space Telescope and Spitzer Imaging of Red and Blue Galaxies at z ˜2.5: A Correlation between Size and Star Formation Activity from Compact Quiescent Galaxies to Extended Star-forming Galaxies. *The Astrophysical Journal*, 671(1):285–302, Dec. 2007.

[200] R. Tojeiro, E. Eardley, J. A. Peacock, P. Norberg, M. Alpaslan, S. P. Driver, B. Henriques, A. M. Hopkins, P. R. Kafle, A. S. G. Robotham, P. Thomas, C. Tonini, and V. Wild. Galaxy and Mass Assembly (GAMA): halo formation times and halo assembly bias on the cosmic web. *Monthly Notices of the Royal Astronomical Society*, 470(3):3720–3741, Sept. 2017.

[201] C. Tortora, F. La Barbera, N. R. Napolitano, N. Roy, M. Radovich, S. Cavuoti, M. Brescia, G. Longo, F. Getman, M. Capaccioli, A. Grado, K. H. Kuijken, J. T. A. de Jong, J. P. McFarland, and E. Puddu. Towards a census of supercompact massive galaxies in the Kilo Degree Survey. *Monthly Notices of the Royal Astronomical Society*, 457(3):2845–2854, Apr. 2016.

[202] C. Tortora, N. R. Napolitano, M. Radovich, C. Spiniello, L. Hunt, N. Roy, L. Moscardini, D. Scognamiglio, M. Spavone, M. Brescia, S. Cavuoti, G. D'Ago, G. Longo, F. Bellagamba, M. Maturi, and M. Roncarelli. Nature versus nurture: relic nature and environment of the most massive passive galaxies at $z < 0.5$. *Astronomy & Astrophysics*, 638:L11, June 2020.

[203] C. Tortora, A. J. Romanowsky, and N. R. Napolitano. An Inventory of the Stellar Initial Mass Function in Early-type Galaxies. *The Astrophysical Journal*, 765(1):8, Mar. 2013.

[204] T. Treu and L. V. E. Koopmans. The Internal Structure and Formation of Early-Type Galaxies: The Gravitational Lens System MG 2016+112 at z = 1.004. *The Astrophysical Journal*, 575(1):87–94, Aug. 2002.

[205] T. Treu and L. V. E. Koopmans. Massive Dark Matter Halos and Evolution of Early-Type Galaxies to z ~1. *The Astrophysical Journal*, 611(2):739–760, Aug. 2004.

[206] I. Trujillo, A. J. Cenarro, A. de Lorenzo-Cáceres, A. Vazdekis, I. G. de la Rosa, and A. Cava. Superdense Massive Galaxies in the Nearby Universe. *The Astrophysical Journal Letters*, 692(2):L118–L122, Feb. 2009.

[207] I. Trujillo, C. J. Conselice, K. Bundy, M. C. Cooper, P. Eisenhardt, and R. S. Ellis. Strong size evolution of the most massive galaxies since $z \sim 2$. *Monthly Notices of the Royal Astronomical Society*, 382(1):109–120, Nov. 2007.

[208] I. Trujillo, A. Ferré-Mateu, M. Balcells, A. Vazdekis, and P. Sánchez-Blázquez. NGC 1277: A Massive Compact Relic Galaxy in the Nearby Universe. *The Astrophysical Journal Letters*, 780(2):L20, Jan. 2014.

[209] I. Trujillo, G. Feulner, Y. Goranova, U. Hopp, M. Longhetti, P. Saracco, R. Bender, V. Braito, R. Della Ceca, N. Drory, F. Mannucci, and P. Severgnini. Extremely compact massive galaxies at z~1.4. *arXiv e-prints*, pages astro–ph/0608657, Aug. 2006.

[210] I. Trujillo, A. W. Graham, and N. Caon. On the estimation of galaxy structural parameters: the Sérsic model. *Monthly Notices of the Royal Astronomical Society*, 326(3):869–876, Sept. 2001.

[211] J. van de Sande, M. Kriek, M. Franx, P. G. van Dokkum, R. Bezanson, K. E. Whitaker, G. Brammer, I. Labbé, P. J. Groot, and L. Kaper. The Stellar Velocity Dispersion of a Compact Massive Galaxy at z = 1.80 Using X-Shooter: Confirmation of the Evolution in the Mass-Size and Mass-Dispersion Relations. *The Astrophysical Journal Letters*, 736(1):L9, July 2011.

[212] R. C. E. van den Bosch, K. Gebhardt, K. Gültekin, A. Yıldırım, and J. L. Walsh. Hunting for Supermassive Black Holes in Nearby Galaxies With the Hobby-Eberly Telescope. *The Astrophysical Journal Supplement*, 218(1):10, May 2015.

[213] A. van der Wel, M. Franx, P. G. van Dokkum, R. E. Skelton, I. G. Momcheva, K. E. Whitaker, G. B. Brammer, E. F. Bell, H. W. Rix, S. Wuyts, H. C. Ferguson, B. P. Holden, G. Barro, A. M. Koekemoer, Y.-Y. Chang, E. J. McGrath, B. Häussler, A. Dekel, P. Behroozi, M. Fumagalli, J. Leja, B. F. Lundgren, M. V. Maseda, E. J. Nelson, D. A. Wake, S. G. Patel, I. Labbé, S. M. Faber, N. A. Grogin, and D. D. Kocevski. 3D-HST+CANDELS: The Evolution of the Galaxy Size-Mass Distribution since z = 3. *The Astrophysical Journal*, 788(1):28, June 2014.

[214] A. van der Wel, B. P. Holden, A. W. Zirm, M. Franx, A. Rettura, G. D. Illingworth, and H. C. Ford. Recent Structural Evolution of Early-Type Galaxies: Size Growth from z = 1 to z = 0. *The Astrophysical Journal*, 688(1):48–58, Nov. 2008.

[215] P. G. van Dokkum. Evidence of Cosmic Evolution of the Stellar Initial Mass Function. *The Astrophysical Journal*, 674(1):29–50, Feb. 2008.

[216] P. G. van Dokkum, K. E. Whitaker, G. Brammer, M. Franx, M. Kriek, I. Labbé, D. Marchesini, R. Quadri, R. Bezanson, G. D. Illingworth, A. Muzzin, G. Rudnick, T. Tal, and D. Wake. The Growth of Massive Galaxies Since z = 2. *The Astrophysical Journal*, 709(2):1018–1041, Feb. 2010.

[217] P. Virtanen, R. Gommers, T. E. Oliphant, M. Haberland, T. Reddy, D. Cournapeau, E. Burovski, P. Peterson, W. Weckesser, J. Bright, S. J. van der Walt, M. Brett, J. Wilson, K. J. Millman, N. Mayorov, A. R. J. Nelson, E. Jones, R. Kern, E. Larson, C. J. Carey, İ. Polat, Y. Feng, E. W. Moore, J. VanderPlas, D. Laxalde, J. Perktold, R. Cimrman, I. Henriksen, E. A. Quintero, C. R. Harris, A. M. Archibald, A. H. Ribeiro, F. Pedregosa, P. van Mulbregt, and SciPy 1.0 Contributors. SciPy 1.0: Fundamental Algorithms for Scientific Computing in Python. *Nature Methods*, 17:261–272, 2020.

[218] M. Vogelsberger, S. Genel, D. Sijacki, P. Torrey, V. Springel, and L. Hernquist. A model for cosmological simulations of galaxy formation physics. *Monthly Notices of the Royal Astronomical Society*, 436(4):3031–3067, Dec. 2013.

[219] Y. Wang, M. Vogelsberger, D. Xu, S. Mao, V. Springel, H. Li, D. Barnes, L. Hernquist, A. Pillepich, F. Marinacci, R. Pakmor, R. Weinberger, and P. Torrey. Early-type galaxy density profiles from IllustrisTNG - I. Galaxy correlations and the impact of baryons. *Monthly Notices of the Royal Astronomical Society*, 491(4):5188–5215, Feb. 2020.

[220] R. H. Wechsler, J. S. Bullock, J. R. Primack, A. V. Kravtsov, and A. Dekel. Concentrations of Dark Halos from Their Assembly Histories. *The Astrophysical Journal*, 568(1):52–70, Mar. 2002.

[221] S. Wellons, P. Torrey, C.-P. Ma, V. Rodriguez-Gomez, A. Pillepich, D. Nelson, S. Genel, M. Vogelsberger, and L. Hernquist. The diverse evolutionary paths of simulated high-z

massive, compact galaxies to z = 0. *Monthly Notices of the Royal Astronomical Society*, 456(1):1030–1048, Feb. 2016.

[222] S. Wellons, P. Torrey, C.-P. Ma, V. Rodriguez-Gomez, M. Vogelsberger, M. Kriek, P. van Dokkum, E. Nelson, S. Genel, A. Pillepich, V. Springel, D. Sijacki, G. Snyder, D. Nelson, L. Sales, and L. Hernquist. The formation of massive, compact galaxies at z = 2 in the Illustris simulation. *Monthly Notices of the Royal Astronomical Society*, 449(1):361–372, May 2015.

[223] S. D. M. White and C. S. Frenk. Galaxy Formation through Hierarchical Clustering. *The Astrophysical Journal*, 379:52, Sept. 1991.

[224] D. Xu, V. Springel, D. Sluse, P. Schneider, A. Sonnenfeld, D. Nelson, M. Vogelsberger, and L. Hernquist. The inner structure of early-type galaxies in the Illustris simulation. *Monthly Notices of the Royal Astronomical Society*, 469(2):1824–1848, Aug. 2017.

[225] A. Yıldırım, R. C. E. van den Bosch, G. van de Ven, B. Husemann, M. Lyubenova, J. L. Walsh, K. Gebhardt, and K. Gültekin. MRK 1216 and NGC 1277 - an orbit-based dynamical analysis of compact, high-velocity dispersion galaxies. *Monthly Notices of the Royal Astronomical Society*, 452(2):1792–1816, Sept. 2015.

[226] A. Yıldırım, R. C. E. van den Bosch, G. van de Ven, I. Martín-Navarro, J. L. Walsh, B. Husemann, K. Gültekin, and K. Gebhardt. The structural and dynamical properties of compact elliptical galaxies. *Monthly Notices of the Royal Astronomical Society*, 468(4):4216–4245, July 2017.

[227] Y. Yoon, M. Im, and J.-W. Kim. Massive Galaxies Are Larger in Dense Environments: Environmental Dependence of Mass-Size Relation of Early-type Galaxies. *The Astrophysical Journal*, 834(1):73, Jan. 2017.

[228] Y. Yoon, J. Ko, and J.-W. Kim. Impact of galaxy mergers on stellar population profiles of early-type galaxies. *The Astrophysical Journal*, 946(1):41, mar 2023.

[229] Y. Yoon, C. Park, H. Chung, and R. R. Lane. Evidence for Impact of Galaxy Mergers on Stellar Kinematics of Early-type Galaxies. *The Astrophysical Journal*, 925(2):168, Feb. 2022.

[230] K. Yun, A. Pillepich, E. Zinger, D. Nelson, M. Donnari, G. Joshi, V. Rodriguez-Gomez, S. Genel, R. Weinberger, M. Vogelsberger, and L. Hernquist. Jellyfish galaxies with the IllustrisTNG simulations - I. Gas-stripping phenomena in the full cosmological context. *Monthly Notices of the Royal Astronomical Society*, 483(1):1042–1066, Feb. 2019.

[231] H. J. Zahid, M. J. Geller, I. Damjanov, and J. Sohn. The Coevolution of Massive Quiescent Galaxies and Their Dark Matter Halos over the Last 6 Billion Years. *The Astrophysical Journal*, 878(2):158, June 2019.

[232] F. Zwicky. The coma cluster of galaxies. *Publications of the Astronomical Society of the Pacific*, 63(371):61, apr 1951.

Appendix A

Subhalo Switching

When two massive subhalos get closer to each other, the identification of the primary subhalo (most massive subhalo in the halo group) may switch between the two subhalos in different snapshots. Figure A.1 shows the distance to two neighboring subhalos from the center of the halo group (particle with the minimum gravitational potential). As it illustrates, the distance can vary by 1000 kpc in one snapshot.

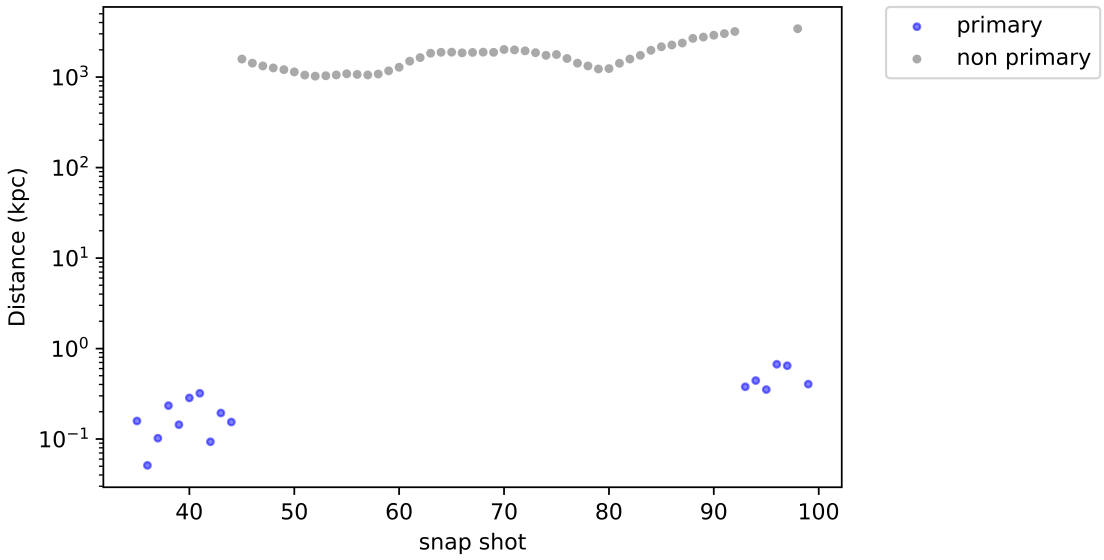

Figure A.1: The distance between the subhalo and parent halo's centers at different snapshots (snaps). Center for each object is the most bounded particle. Blue are the snapshots where it's the primary subhalo of the halo group.

Appendix B

Dependence on Halo Formation Time

Therefore, we chose two redshifts (z = 1.5 and 2) for the redshift (z_i) where the first phase died out. We then explore the properties separately for the three different samples (they overlap). The reason for choosing only redshift 1.5 is that it is the next snapshot with all the details of the particles available after z = 2.

Motivated by Arriba et al. [153] and following the two-phase galaxy evolution paradigm, we chose criteria to define relic galaxies physically based on the halo formation time (z_f) and the change in stellar mass. We constrain dark matter and stellar mass change by considering how much mass has changed since the halo formed (i.e. the first phase became negligible). Since the first phase is believed to die out at the redshift $z \sim 2$, we relax the value for z_f and investigate the impact on relicness. Ideally, it is best to choose a range of redshifts centered around z = 2, but the closest redshifts that TNG300 provides snapshots with full particle data are z = 1.5 and z = 3. Therefore, we choose z = 1.5 and z = 2.

Table B.1: Criteria used to define Relics. Throughout its growth history, M_{200} of the halo reaches its peak after the redshift z^{dm}_{peak} . z_f is the halo formation time. $\frac{M^*_{z=z_f}}{M^*_{z=0}}$ is the ratio of stellar masses at $z = z_f$ to $z = 0$. The last column indicates the number of relics for each criteria

Criteria	z^{dm}_{peak}	z_f	$\frac{M^*_{z=z_f}}{M^*_{z=0}}$	Relics
15E	0.1	1.5	0.9	1309
15E-dm4	0.1	1.5	0.9	1636
15d	0.2	1.5	0.8	1985
15R	0.3	1.5	0.7	2766
15R-dm4	0.3	1.5	0.7	3522
2E	0.1	2	0.9	376
2E-dm4	0.1	2	0.9	615
2d	0.2	2	0.8	562
2R	0.3	2	0.7	826

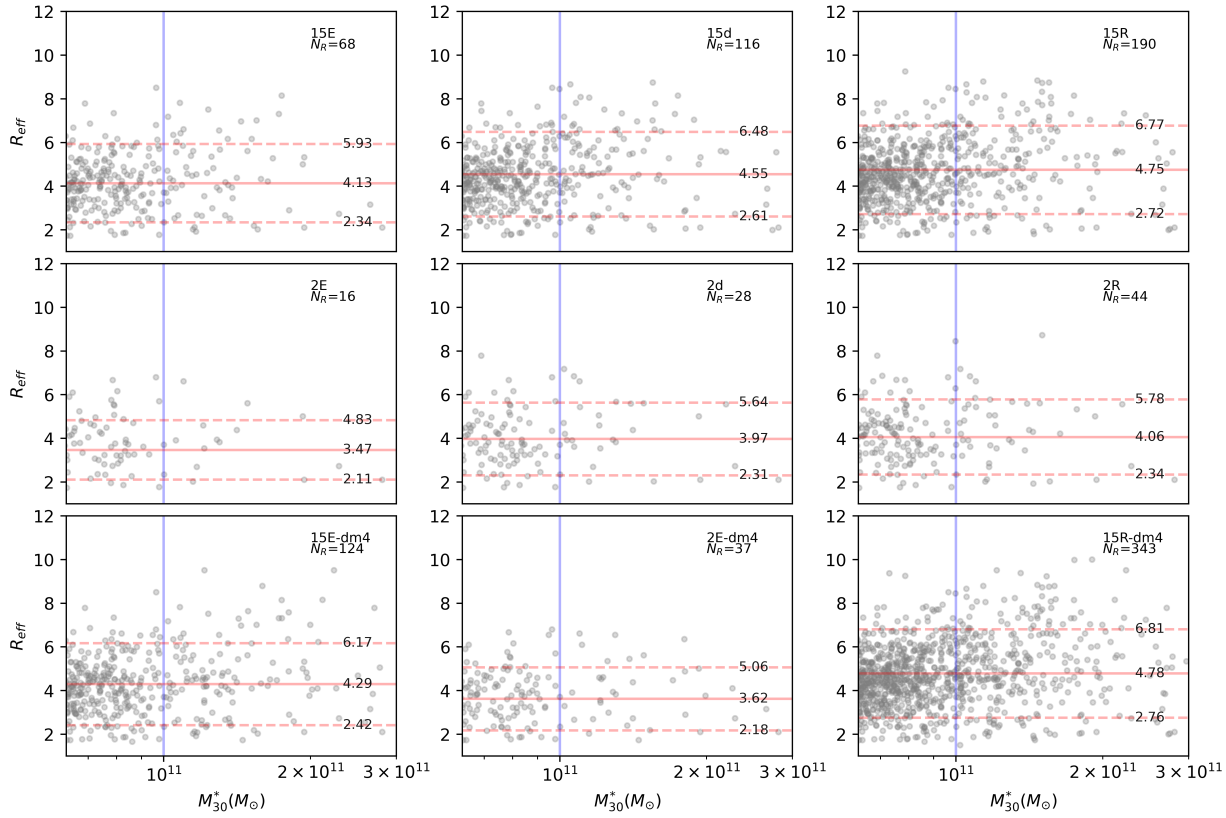

Figure B.1: Comparison of Mass-half-light radius planes for each relic definitions described in Table B.1. Red lines show the median (solid) and ±1 standard deviation (dashed) assuming half-light radii follow a log-normal distribution.

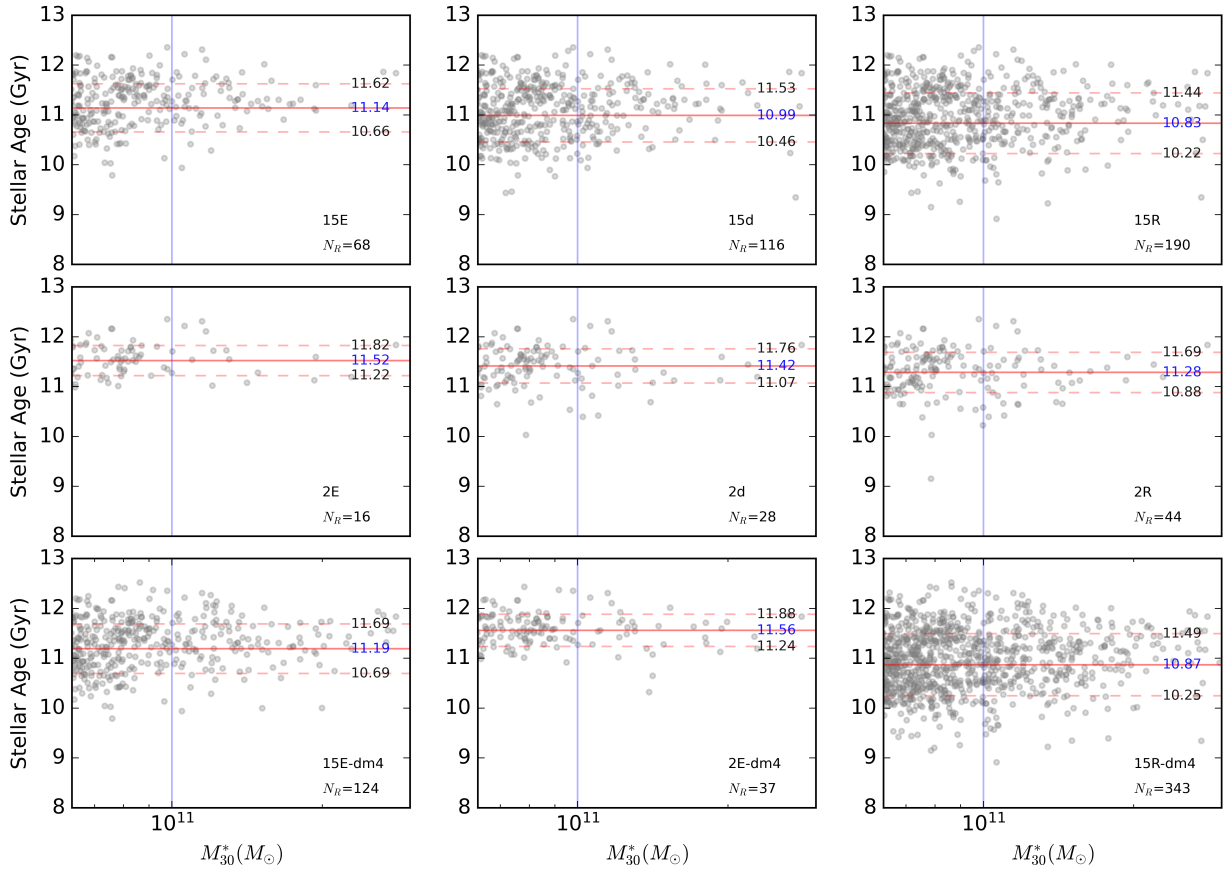

Figure B.2: Comparison of Mass-stellar age planes for each relic definitions used in the first step in section 3.3.

Appendix C

Effects from Galaxy Flybys

We plot the mass assembly history since z = 2 and galaxies in the local environment for highly concentrated (c_{200}) halos in Figure C.1.

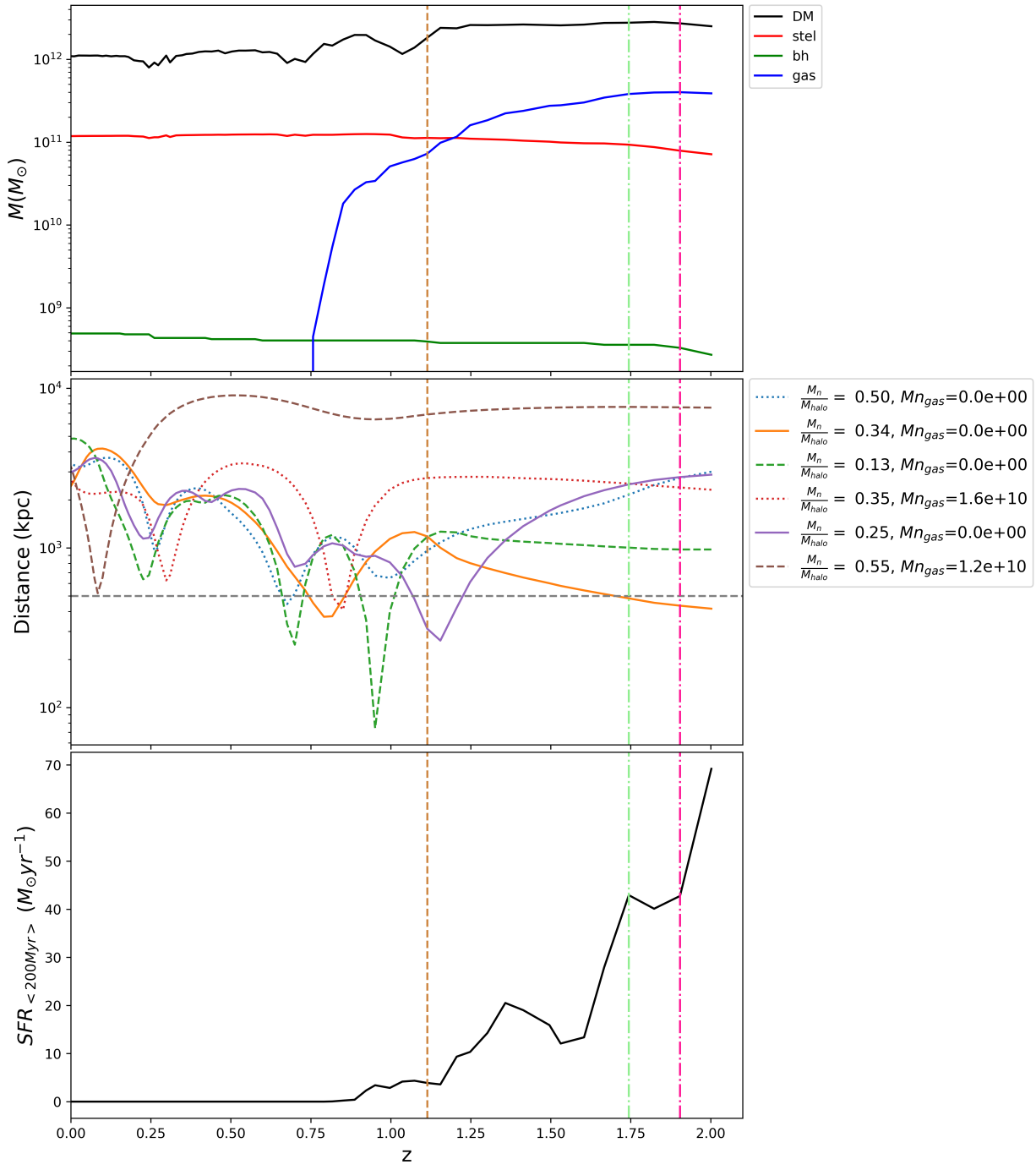

Figure C.1: Mass growth history (top), neighbouring subhalos/halos distance from the subhalo center (center) and star formation rates averaged over the last 200 Myr (bottom) for the largest c_{200} positive outlier. (top) Mass includes all the particles identified by the halo finder for the outlier halo. (middle) The total mass fraction respect to the outlier halo at the closest point ($\frac{M_n}{M_{halo}}$) to each other is quoted in the legend. The neighbours are considered as described in Section 5.3.5. Pink and green dotted dashed lines represent the redshift that a major and minor merger respectively occured.

Appendix D

Gas Temperature Calculation

First the average molecular weight (μ) is calculated by

$$\mu = \frac{4m_p}{1 + 3X_{\rm H} + 4X_{\rm H}X_e} \tag{D.1}$$

where m_p is the mass of the proton, $X_{\rm H}$ is the hydrogen mass fraction ($X_{\rm H} = 0.76$), and X_e is the electron abundance.

Then, the temperature (T) is given by

$$T = (\gamma - 1)\, u\, \mu \tag{D.2}$$

where γ is the adiabatic index ($\gamma = 5/3$) and u is the internal energy; i.e., thermal energy

per unit mass of a selected gas cell[1].

[1]Available on https://www.tng-project.org/data/downloads/TNG300-1/